



**University of
Zurich^{UZH}**

Event-based surface hydrological connectivity and sediment transport on young moraines

ESS 511 Master's Thesis

Author

Florian Lustenberger
13-761-861

Supervised by

Fabian Maier
Dr. Ilja van Meerveld

Faculty representative

Prof. Dr. Jan Seibert

29.04.2019

Department of Geography, University of Zurich



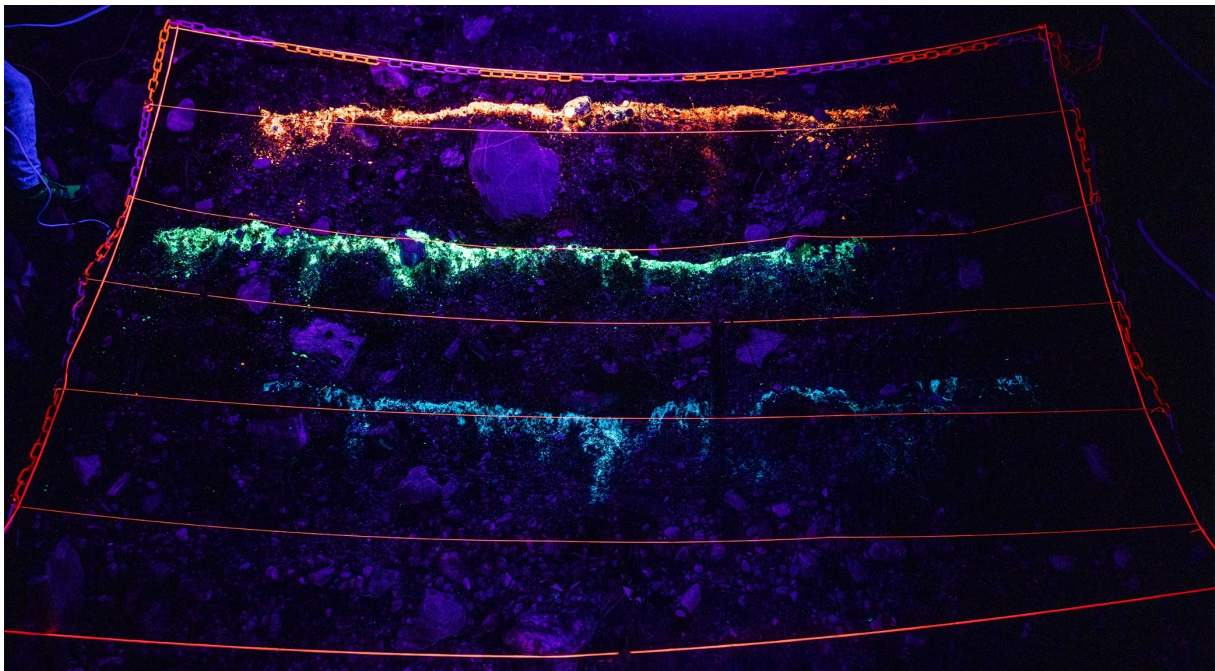
University of
Zurich^{UZH}

EVENT-BASED SURFACE HYDROLOGICAL CONNECTIVITY AND SEDIMENT TRANSPORT ON YOUNG MORAINES

Introducing a new method based on fluorescent sand

MASTER THESIS

To obtain the academic degree of
Master of Science in Earth System Science



AUTHOR

Florian R. Lustenberger
13-761-861

SUPERVISED BY

Fabian Maier
Dr. Ilja van Meerveld

FACULTY REPRESENTATIVE

Prof. Dr. Jan Seibert

Submitted to the Department of Geography, University of Zurich
April 2019

Abstract

Surface hydrological connectivity describes whether two points on the soil surface are connected by water flow. It affects the transport of water, sediment, nutrients and organic matter and thereby drives the process of soil erosion. It is, therefore, important to improve our understanding of how surface hydrological connectivity is established. However, it is difficult to observe connectivity during rainfall events and therefore our understanding of surface connectivity is still limited. In this thesis, a new method to study surface hydrological connectivity and sediment transport on hillslopes was tested. Surface runoff was measured during three artificial rainfall experiments on six plots on three different moraines in the Swiss Alps. Sediment transport pathways were determined using a fluorescent sand tracer and analyzing pre- and post-event photographs. The surface soil characteristics were determined for the six plots as well. The results strongly suggest that rainfall intensity, vegetation cover and plant species richness are the main factors that determine the transport of sediment. Higher rainfall intensities enhanced sediment movement by locally occurring surface runoff and rain splash, while higher vegetation cover and a higher number of plant species reduced transport distances. Slope angle and surface roughness affect transport distances as well. Surface hydrological connectivity could be visualized using the sand tracer on areas where surface runoff was widespread – such as sparsely vegetated hillslopes on a young glacial moraine. On those areas surface hydrological connectivity was likely to be very similar to the sediment connectivity. On older and densely vegetated hillslopes on glacial moraines, erosion by rain splash dominated sediment transport and little surface runoff was observed.

Key words:

surface hydrological connectivity, sediment transport, soil, erosion, hillslopes, rainfall experiments, fluorescent sand, particle tracer, Steingletscher, Swiss Alps, HILLSCAPE

Table of contents

ABSTRACT	I
TABLE OF CONTENTS	II
LIST OF FIGURES	IV
LIST OF TABLES	VIII
1 INTRODUCTION	1
1.1 SOIL EROSION	1
1.2 SURFACE CONNECTIVITY.....	3
1.3 ARTIFICIAL TRACER EXPERIMENTS AND FLUORESCENT TRACERS.....	4
1.4 RESEARCH OBJECTIVES AND QUESTIONS	5
2 HILLSCAPE	7
3 STUDY SITE	8
3.1 STUDY AREA	8
3.2 STUDY SITES	10
4 METHODS	13
4.1 EXPERIMENTAL PLOTS	13
4.2 RAINFALL SIMULATION EXPERIMENTS	14
4.2.1 <i>Rainfall application</i>	14
4.2.2 <i>Surface runoff</i>	15
4.2.3 <i>Sediment concentrations</i>	16
4.2.4 <i>Sediment transport</i>	17
4.2.5 <i>Surface runoff pathways</i>	19
4.3 SITE CHARACTERISTICS.....	19
4.3.1 <i>Vegetation</i>	19
4.3.2 <i>Slope angle</i>	19
4.3.3 <i>Microtopography</i>	19
4.3.4 <i>Saturated hydraulic conductivity</i>	21
5 DATA ANALYSIS	22
5.1 SURFACE TOPOGRAPHY.....	22
5.1.1 <i>Microtopography</i>	22
5.1.2 <i>Flow directions</i>	23
5.2 FLUORESCENT SAND TRANSPORT	23
5.3 SAND AND BLUE DYE	27

5.4	CORRELATION ANALYSIS AND PCA	28
6	RESULTS.....	29
6.1	SITE CHARACTERISTICS	29
6.1.1	<i>Vegetation</i>	29
6.1.2	<i>Slope angle</i>	29
6.1.3	<i>Surface roughness</i>	30
6.1.4	<i>Saturated hydraulic conductivity</i>	30
6.2	SURFACE RUNOFF AND SEDIMENT LOAD	31
6.3	SEDIMENT TRANSPORT	31
6.4	SURFACE CONNECTIVITY.....	34
6.5	CORRELATION ANALYSIS.....	40
7	DISCUSSION	46
7.1	EVALUATION OF THE NEW FLUORESCENT SAND METHOD	46
7.1.1	<i>Field setup</i>	46
7.1.2	<i>The fluorescent sand</i>	48
7.1.3	<i>Photo analyses</i>	49
7.1.4	<i>Measures of sediment transport</i>	50
7.2	DOMINANT EROSION PROCESSES	51
7.3	EFFECTS OF SITE CHARACTERISTICS ON SEDIMENT TRANSPORT.....	52
7.4	EFFECT OF RAINFALL INTENSITY ON SEDIMENT TRANSPORT	55
7.5	SURFACE HYDROLOGICAL CONNECTIVITY	57
8	CONCLUSIONS.....	59
9	RECOMMENDATION FOR FURTHER RESEARCH & IMPROVEMENTS	61
	ACKNOWLEDGEMENTS.....	63
	LITERATURE.....	64
	DECLARATION OF ORIGINALITY	75
	APPENDIX 1: CALCULATIONS	I
	APPENDIX 2: CORRELATION TABLES.....	IV
	APPENDIX 3: SAND PHOTOGRAPHS	VII
	APPENDIX 4: SAND EXTRACTION METHODS	XIII

List of Figures

FIGURE 1.1 SKETCH SUMMARIZING THE EFFECTS OF THE RAINFALL INTENSITY, THE SURFACE RUNOFF AND THE SITE CHARACTERISTICS (VEGETATION COVER, PLANT SPECIES RICHNESS, SLOPE, SURFACE ROUGHNESS, SATURATED HYDRAULIC CONDUCTIVITY) ON EROSION AND/OR SEDIMENT TRANSPORT. GREEN ARROWS REPRESENT POSITIVE AND RED ARROWS NEGATIVE FEEDBACKS.....	3
FIGURE 3.1 STUDY AREA IN THE FOREFIELD OF THE STEINGLETSCHER (SOUTH WEST OF SUSTENPASS) IN THE WESTERNMOST PART OF CANTON BERN (SWITZERLAND). THE LOCATION OF THE THREE MORAINES (3K, 1860, 1990) ARE INDICATED. THE MAP WAS MODIFIED FROM SWISSTOPO (FEDERAL OFFICE OF TOPOGRAPHY SWISSTOPO, 2019A).....	9
FIGURE 3.2 THE SIX EXPERIMENTAL PLOTS STUDIED IN THIS THESIS: 3K, 1860 LEFT, 1860 RIGHT, 1990 LEFT, 1990 MIDDLE AND 1990S RIGHT. THE VEGETATION COVER IS CLEARLY HIGHER AT THE THREE OLDER PLOTS THAN ON THE THREE 1990 PLOTS.	11
FIGURE 3.3 THE TEXTURE OF THE TOPSOIL OF THE THREE MORAINES (3K, 1860, 1990) IN THE GRAIN SIZE DIAGRAM MODIFIED AFTER IUSS WORKING GROUP WRB (2015). THE GRAIN SIZE FRACTIONS WERE OBTAINED FROM MUSSO ET AL. (IN REVIEW). ALL THREE MORAINES WERE RATHER SANDY.	12
FIGURE 4.1 SETUP OF THE EXPERIMENTAL PLOTS (HERE 1860 LEFT), INCLUDING THREE SENNINGER I-WOB® SPRINKLERS, TIPPING BUCKET RAIN GAUGES, PLASTIC BOUNDARIES AROUND THE PLOT, A GUTTER AT THE BOTTOM OF THE PLOT, HOSES (GREEN) TO ROUTE THE SURFACE AND SUBSURFACE FLOW TO THE CYCLOPS-7 TURBIDITY SENSOR AND THE UPWELLING BERNOULLI TUBES. THE FLUORESCENT SEGMENTED CHAIN AND THE HORIZONTAL LINES, AS WELL AS THE CAMERA TOWER TO DETERMINE THE FLUORESCENT SAND TRANSPORT ARE SHOWN AS WELL.	13
FIGURE 4.2 SETUP FOR THE SUBSURFACE AND SURFACE FLOW MEASUREMENTS FOR THE EXPERIMENTAL PLOTS, INCLUDING A GUTTER AT THE BOTTOM OF THE PLOT, HOSES (GREEN) TO ROUTE THE SURFACE AND SUBSURFACE FLOW TO THE CYCLOPS-7 TURBIDITY SENSOR AND THE UPWELLING BERNOULLI TUBES. THE PHOTOS OF THE GUTTER AND THE UPWELLING BERNOULLI TUBES WERE TAKEN BY FABIAN MAIER.	17
FIGURE 4.3 (A) MICROTOPOGRAPHY PROFILER (MTP) IN THE FIELD (3K PLOT, TRANSECT V). (B) SKETCH OF AN EXPERIMENTAL PLOT WITH THE THEORETICAL DIMENSIONS OF 4 × 6 M AND THE TEN TRANSECTS (HORIZONTAL LINES I TO X) FOR WHICH THE MICROTOPOGRAPHY WAS DETERMINED.....	20
FIGURE 5.1 LINEAR DIGITAL EXTENSION OF THE REFERENCE GRID OUTSIDE THE PHOTO IN ORDER TO PERFORM THE GEOMETRIC CORRECTION FOR THE PHOTO OF THE 1990S LEFT PLOT AFTER THE MID INTENSITY RAINFALL SIMULATION.	25
FIGURE 5.2 VISUALIZATION OF THE THREE DIMENSIONS (HUE, SATURATION, VALUE) OF THE HSV COLOR SPACE. HUE IS REPRESENTED ON A CIRCLE IN DEGREES. SATURATION AND VALUE ARE RELATIVE MEASURES AND RANGE BETWEEN 0 % AND 100 %. THIS FIGURE WAS MODIFIED FROM RAHMAT ET AL. (2016).....	25
FIGURE 5.3 (A) IMAGE OF THE EXTRACTED GREEN SAND (MID INTENSITY) ON THE 1990S LEFT PLOT. THE DISTANCES ARE THE SAME AS ON THE PHOTO BEFORE THE EXTRACTION; THE COORDINATE (0, 0) IS LOCATED AT THE TOP LEFT CORNER. ONE PIXEL CORRESPONDS TO 1 MM ² . PER PIXEL ROW THE NUMBER OF CLASSIFIED PIXELS WAS COUNTED AND PLOTTED AS DENSITY CURVE (B). THE SAND LINE AND THE PARTICLES BELOW THE LINE CAN CLEARLY BE IDENTIFIED. THE RED LINE MARKS THE PEAK (MIDDLE) OF THE SAND LINE AND REPRESENTS THE AVERAGED 'ZERO-DISTANCE' OF THE SAND MOVEMENT.	27
FIGURE 6.1 BOXPLOTS OF (A) THE SLOPE ANGLE IN DEGREE, (B) THE TORTUOSITY INDEX (TI), AND (C) THE RANDOM ROUGHNESS (RR) IN MM AS WELL AS (D) A SCATTER PLOT OF THE SATURATED HYDRAULIC CONDUCTIVITY K_{SAT} IN MM/H FOR ALL SIX EXPERIMENTAL PLOTS. THE STARS INDICATE THE SIGNIFICANCE LEVEL OF THE KRUSKAL-WALLIS TEST FOR SLOPE ANGLE AND RANDOM	

ROUGHNESS AND OF THE ANOVA FOR TORTUOSITY INDEX AND K_{SAT} (** $p < 0.001$, ** $p < 0.01$, * $p < 0.05$). DIFFERENT LETTERS INDICATE SIGNIFICANT DIFFERENT MEAN VALUES BASED ON THE POST-HOC TEST (SIGNIFICANCE LEVEL: $\alpha = 0.05$).....	30
FIGURE 6.2 RELATIVE CUMULATIVE FREQUENCY CURVES FOR THE FLUORESCENT SAND THAT MOVED FOR ALL THREE RAINFALL INTENSITIES (LOW = ORANGE, MID = GREEN, HIGH = BLUE) ON (A) THE 3K PLOT, (B) THE 1860S LEFT PLOT, (C) THE 1860S RIGHT PLOT, (D) THE 1990S LEFT PLOT, (E) THE 1990S MIDDLE PLOT AND (F) THE 1990S RIGHT PLOT. ON THE 3K PLOT ONLY ONE SAND LINE (FOR THE LOW INTENSITY SIMULATION) WAS APPLIED. THE HORIZONTAL LINES FOR THE EXTRACTED CUMULATIVE SAND DISTANCES ARE MARKED AND LABELED (50 %, 75 %, 90 %).	32
FIGURE 6.3 THE (A) 50 %, (B) 75 %, (C) 90 %, AND (D) 100 % (MAXIMUM SAND MOVEMENT) OF THE CUMULATIVE FREQUENCY OF THE TRANSPORT DISTANCES FOR ALL SAND PARTICLES THAT MOVED AS A FUNCTION OF THE SIMULATED RAINFALL INTENSITY (LOW, MID, HIGH). ON THE 3K PLOT ONLY ONE SAND LINE (FOR THE LOW INTENSITY SIMULATION) WAS APPLIED. ON THE 1990S MORAINES LEFT AND RIGHT PLOTS SAND MOVED BELOW THE LOWER PLOT BOUNDARY FOR THE HIGH INTENSITY EVENT AND THEIR MAXIMUM MOVEMENT VALUES WERE TOO SMALL (INDICATED WITH THE ARROW).....	33
FIGURE 6.4 PHOTOS OF THE FLUORESCENT SAND LINES AFTER ALL THREE RAINFALL SIMULATIONS OF THE 3K, 1860 LEFT, 1860 RIGHT, 1990 LEFT, 1990 MIDDLE AND 1990 RIGHT PLOTS. OUTLINES (IN THE CORRESPONDING COLOR) WERE DRAWN AROUND THE MAXIMUM SAND EXTENT AND ARE ALSO PRESENTED ON THE RIGHT WITHOUT THE PHOTO. THE RED ELLIPSE INDICATES A POSSIBLE FLOW PATH (SEE TEXT).....	36
FIGURE 6.5 (A) AREAS OF OBSERVED SURFACE RUNOFF ON THE 1990S RIGHT PLOT. IN BLUE (1, 2, 3), AREAS WHERE THE BRILLIANT BLUE DYE TRACER WAS ADDED. THE BLACK DASHED LINE INDICATES AN AREA WHERE SURFACE RUNOFF WAS OBSERVED BUT NO TRACER DYE WAS ADDED. (B) THE DISTRIBUTION OF THE SAND AFTER ALL THREE RAINFALL EXPERIMENTS AND THE OUTLINE (IN THE CORRESPONDING COLOR) ON THE SAME PLOT IS SHOWN (SEE ALSO FIGURE 6.4). (C) COMBINATION OF THE SHAPES FROM THE OBSERVED SURFACE RUNOFF (A) AND THE FLUORESCENT SAND (B). THE ARROWS INDICATE WHERE THE FLOW DIRECTIONS OF WATER AND SEDIMENT OVERLAPPED.	37
FIGURE 6.6 AREAL DRONE IMAGES AND DIGITAL TERRAIN MODEL (DTM) BASED FLOW ACCUMULATION OF ALL SIX EXPERIMENTAL PLOTS. THE FLOW ACCUMULATION CALCULATED BASED ON THE DTM AND THE $D-\infty$ METHOD IS SHOWN IN BLUE (DARKER BLUE REPRESENTS MORE FLOW ACCUMULATION). THE THICK RED LINES REPRESENT THE PLOT BORDERS, THE THIN RED LINES THE AREA OF THE FLUORESCENT SAND SETUP. THE COLORED SHAPES WITH BLACK OUTLINES INDICATE THE SAND COVERED AREAS AFTER ALL THREE RAINFALL INTENSITIES (SEPARATED BY THE SAND COLOR; SIMILAR TO FIGURE 6.4). THE BLUE ARROWS ON THE 1990S RIGHT PLOT INDICATE THE OBSERVED FLOW PATHS OF SURFACE FLOW (AS SHOWN IN FIGURE 6.5c).	38
FIGURE 6.7 3-DIMENSIONAL VISUALIZATION OF THE MICROTOPOGRAPHY LINES (BLUE) FOR THE LOWER PART OF THE 1990S RIGHT PLOT (TRANSECTS V TO X). THE DASHED RED LINES SCHEMATICALLY REPRESENT THE PLOT BOUNDARIES AND THE HORIZONTAL ROPES. THE BLACK SHAPE OUTLINES ON THE PLOT REPRESENT THE SKETCHED PATTERN OF THE DYE TRACER (CONTINUOUS) AND OBSERVED SURFACE FLOW (DASHED), AS PRESENTED IN FIGURE 6.5. THE GREEN ARROW INDICATES THE FLOW AROUND THE LOCAL TOPOGRAPHIC "HIGH"	39
FIGURE 6.8 THE TWO FIRST PRINCIPAL COMPONENTS (PC1, PC2, BASED ON THE PCA) FOR THE FIVE SITE CHARACTERISTICS (VEGETATION COVER, NUMBER OF PLANT SPECIES, SLOPE ANGLE, TORTUOSITY INDEX, RANDOM ROUGHNESS, SATURATED HYDRAULIC CONDUCTIVITY K_{SAT}) FOR ALL SIX EXPERIMENTAL PLOTS (SHOWN WITH SYMBOLS). THE EXPLAINED VARIANCE OF THE PRINCIPAL COMPONENTS IS INDICATED IN THE AXIS LABELS.	41

- FIGURE 6.9 SCATTERPLOTS OF THE RELATIONS BETWEEN THE FOUR SAND DISTANCE MEASURES (BASED ON THE RELATIVE CUMULATIVE TRAVEL DISTANCES: 50 %, 75 %, 90 % AND MAXIMUM DISTANCE) AND THE MEAN VALUE OF THE SITE CHARACTERISTICS (SLOPE ($^{\circ}$), TORTUOSITY INDEX TI (-), RANDOM ROUGHNESS RR (CM), VEGETATION COVER (%), NUMBER OF PLANT SPECIES (SPEC. RICHNESS), SATURATED HYDRAULIC CONDUCTIVITY K_{SAT} (MM/H)) AND THE FIRST TWO PRINCIPAL COMPONENTS (PC1, PC2) OF THE PCA OF THE SITE CHARACTERISTICS FOR THE **LOW RAINFALL** INTENSITY EXPERIMENTS. THE GREEN COLORED SHADING INDICATES SIGNIFICANT SPEARMAN RANK CORRELATIONS (SIGNIFICANCE LEVEL: $\alpha = 0.1$). THE COLORED SYMBOLS REPRESENT THE EXPERIMENTAL PLOTS (SEE FIGURE 6.12). 42
- FIGURE 6.10 SCATTERPLOTS OF THE RELATIONS BETWEEN THE FOUR SAND DISTANCE MEASURES (BASED ON THE RELATIVE CUMULATIVE TRAVEL DISTANCES: 50 %, 75 %, 90 % AND MAXIMUM DISTANCE) AND THE MEAN VALUE OF THE SITE CHARACTERISTICS (SLOPE ($^{\circ}$), TORTUOSITY INDEX TI (-), RANDOM ROUGHNESS RR (CM), VEGETATION COVER (%), NUMBER OF PLANT SPECIES (SPEC. RICHNESS), SATURATED HYDRAULIC CONDUCTIVITY K_{SAT} (MM/H)) AND THE FIRST TWO PRINCIPAL COMPONENTS (PC1, PC2) OF THE PCA OF THE SITE CHARACTERISTICS FOR THE **MID RAINFALL** INTENSITY EXPERIMENTS. THE GREEN COLORED SHADING INDICATES SIGNIFICANT SPEARMAN RANK CORRELATIONS (SIGNIFICANCE LEVEL: $\alpha = 0.1$). THE COLORED SYMBOLS REPRESENT THE EXPERIMENTAL PLOTS (SEE FIGURE 6.12). 43
- FIGURE 6.11 SCATTERPLOTS OF THE RELATIONS BETWEEN THE FOUR SAND DISTANCE MEASURES (BASED ON THE RELATIVE CUMULATIVE TRAVEL DISTANCES: 50 %, 75 %, 90 % AND MAXIMUM DISTANCE) AND THE MEAN VALUE OF THE SITE CHARACTERISTICS (SLOPE ($^{\circ}$), TORTUOSITY INDEX TI (-), RANDOM ROUGHNESS RR (CM), VEGETATION COVER (%), NUMBER OF PLANT SPECIES (SPEC. RICHNESS), SATURATED HYDRAULIC CONDUCTIVITY K_{SAT} (MM/H)) AND THE FIRST TWO PRINCIPAL COMPONENTS (PC1, PC2) OF THE PCA OF THE SITE CHARACTERISTICS FOR THE **HIGH RAINFALL** INTENSITY EXPERIMENTS. THE GREEN COLORED SHADING INDICATES SIGNIFICANT SPEARMAN RANK CORRELATIONS (SIGNIFICANCE LEVEL: $\alpha = 0.1$). THE COLORED SYMBOLS REPRESENT THE EXPERIMENTAL PLOTS (SEE FIGURE 6.12). FOR THE 1990S LEFT AND RIGHT PLOTS SAND MOVED BELOW THE PLOT BOUNDARIES (INDICATED WITH A BREAK IN THE X-AXIS)..... 44
- FIGURE 6.12 SCATTERPLOTS OF THE RELATIONS BETWEEN THE FOUR SAND DISTANCE MEASURES (BASED ON THE RELATIVE CUMULATIVE TRAVEL DISTANCES: 50 %, 75 %, 90 % AND MAXIMUM DISTANCE) AND THE VALUES OF THE SURFACE RUNOFF RATIO (%) AND THE SEDIMENT LOAD (G) FOR THE LOW, MID AND HIGH INTENSITY RAINFALL SIMULATION. THE GREEN COLORED SHADING INDICATES SIGNIFICANT SPEARMAN RANK CORRELATIONS (SIGNIFICANCE LEVEL: $\alpha = 0.1$). THE SHAPES AND COLORS OF THE SYMBOLS REPRESENT THE EXPERIMENTAL PLOTS AND ARE THE SAME AS USED IN THE OTHER GRAPHS. FOR THE LOW INTENSITY EVENT SURFACE FLOW AND, HENCE, ALSO SEDIMENT TRANSPORT TO THE BOTTOM OF THE PLOT ONLY OCCURRED ON THE 1990S MIDDLE AND RIGHT PLOTS. THE SURFACE RUNOFF RATIO AND THE SEDIMENT LOAD FOR THE 1990S RIGHT PLOT ARE SLIGHTLY UNDERESTIMATED BECAUSE OF A LACK OF MEASUREMENTS AFTER THE EXPERIMENT STOPPED (INDICATED BY THE BLACK ARROW). FOR THE HIGH INTENSITY SIMULATION SAND MOVED BELOW THE PLOT BOUNDARIES ON THE 1990S LEFT AND RIGHT PLOTS (INDICATED WITH A BREAK IN THE X-AXIS). 45
- FIGURE 7.1 (A) SKETCH OF THE CAMERA TOWER AND AN EXPERIMENTAL PLOT. THE ANGLE λ BETWEEN THE CAMERA LENS AND THE AVERAGE PLOT SURFACE IS 90° FROM THE NADIR VIEW (B) AND SMALLER FROM THE CAMERA TOWER VIEW (C). THE NADIR PHOTO (B) OF THE 1990S RIGHT PLOT WAS TAKEN WITH A DJI PHANTOM 4 PRO. THE PHOTO FROM THE TOWER CAMERA (C) WAS NOT TAKEN AT A NADIR VIEW. THE WHITE ELLIPSES INDICATE AREAS WHERE SAND IS NOT CLEARLY VISIBLE ON THE PICTURE FROM THE TOWER CAMERA. 47

FIGURE 7.2 (A) EXAMPLE OF ROCKS BLOCKING THE SAND FLOW (ON THE SURFACE) ON THE TOP RIGHT CORNER OF THE 1990S MIDDLE PLOT BELOW THE ORANGE AND GREEN SAND LINE. (B) ORANGE SAND, THAT EASILY FLOWED OVER THE ROCK SURFACES OF THE 1990S RIGHT PLOT IN THE TOP RIGHT CORNER.	52
FIGURE 7.3 TWO EXAMPLES OF SURFACE HYDROLOGICAL CONNECTIVITY, VISUALIZED BY THE ADDITION OF BRILLIANT BLUE TRACER DYE TO THE SURFACE RUNOFF, IN THE LOWER PART OF THE 1990S RIGHT PLOT. THE WHITE CIRCLES MARK WATER FILLED DEPRESSIONS (PONDING), WHICH DRAIN WHEN FILLED AND CONNECT WITH OTHER PARTS OF THE AREA VIA OVERLAND FLOW (WHITE ARROWS).	58
FIGURE 9.1 ALTERNATIVE SETUP FOR THE CAMERA AND THE UV-LAMPS TO CAPTURE THE FLUORESCENT SAND, CREATED DURING THE FIELD WORK PREPARATION IN JUNE 2018 AT UNIVERSITY OF ZURICH. THE POSITION OF THE CAMERA ALLOWS THE LENS TO POINT PERPENDICULAR TO PLOT SURFACE ($\lambda = 90^\circ$).	62
FIGURE A.1 SKETCH OF AN EXPERIMENTAL PLOT (RED) IN THE FIELD WITH THE MEASURED DISTANCES A, B, C AND D AS WELL AS THE ANGLES A AND B. THE PLOT IS DIVIDED INTO TWO TRIANGLES ($A_b = \text{BLUE}$ AND $A_d = \text{GREEN}$) FOR THE CALCULATION OF THE ACTUAL PLOT AREA.	III
FIGURE A.2 SKETCH OF A LOWER EXPERIMENTAL PLOT HALF (A), INCLUDING THE MICROTOPOGRAPHY TRANSECTS V TO X. SINCE THE SLOPE ANGLES WERE MEASURED EVERY 0.5 M, THEIR VALUES WERE USED FOR THE CORRESPONDING 25 CM BEFORE AND AFTER A MEASUREMENT WHICH LEADS TO FIVE DISTANCES (E, F, G, H, I) TO WHICH ONE SLOPE ANGLE MEASUREMENT CORRESPONDS. THE TRANSECTS V AND VI WERE IN THE MIDDLE OF DISTANCE E, VII AND VIII IN THE MIDDLE OF DISTANCE G AND IX AND X IN THE MIDDLE OF DISTANCE I. A VERTICAL SIDE VIEW OF THE LOWER PART OF THE PLOT (B) WAS CREATED TO ILLUSTRATE THE CALCULATION OF THE ACTUAL HEIGHT OF MICROTOPOGRAPHY LINES (TRANSECT V AND VI, TRANSECT VII AND VIII) ABOVE THE LOWEST LINE (TRANSECT IX AND X). THEREFORE, THE HEIGHTS Y_e, Y_f, Y_g, Y_h AND Y_i AS WELL AS THE ANGLES Γ, Δ, E, H AND θ ARE PRESENTED.	III
FIGURE A.3 (A) GEOMETRICALLY CORRECTED AND CROPPED PHOTO OF THE GREEN SAND LINE (MID INTENSITY) OF THE 1990 LEFT PLOT. (B) CLASSIFICATION OF THE GREEN SAND LINE BASED ON THE EXTRACTION METHOD USED IN THIS THESIS (HUE IN PYTHON). (C) A SUPERVISED CLASSIFICATION (HERE MAXIMUM LIKELIHOOD) COULD, HOWEVER, ACHIEVE NEARLY AS GOOD RESULTS. THE CLASSIFICATION WAS PERFORMED WITH ENVI (V. 5.4.1), A COMMON SOFTWARE FOR REMOTE SENSING PURPOSES.	XIII

List of Tables

TABLE 1 AGE IN YEARS, THE ACTUAL PLOT SIZE IN THE FIELD (SEE APPENDIX 1), THE DEGREE OF VEGETATION COVER AND THE SLOPE ANGLE IN DEGREE (SEE CHAPTER 4.3.2) OF ALL SIX EXPERIMENTAL PLOTS (3K, 1860 LEFT, 1860 RIGHT, 1990 LEFT, 1990 MIDDLE, 1990 RIGHT) ON THE THREE STUDIED MORAINES (3K, 1860, 1990).....	12
TABLE 2 ACTUAL RAINFALL INTENSITIES FOR THE LOW, MID, AND HIGH INTENSITY EXPERIMENTS FOR ALL SIX EXPERIMENTAL PLOTS (3K, 1860 LEFT, 1860 RIGHT, 1990 LEFT, 1990 MIDDLE, 1990 RIGHT).	15
TABLE 3 SITE CHARACTERISTICS OF ALL SIX EXPERIMENTAL PLOTS: THE ESTIMATED VALUES OF THE VEGETATION COVER (IN %), THE NUMBER OF PLANT SPECIES, THE AVERAGES OF THE SLOPE ANGLE AND THEIR STANDARD DEVIATIONS SD (IN DEGREES), THE TORTUOSITY INDEX TI, THE RANDOM ROUGHNESS RR (IN CM) AND THE SATURATED HYDRAULIC CONDUCTIVITY K_{SAT} (IN MM/H).	29
TABLE 4 SURFACE RUNOFF RATIOS (IN %) AND SEDIMENT LOADS (IN GRAM) FOR ALL SIX EXPERIMENTAL PLOTS AND ALL THREE SIMULATED RAINFALL INTENSITIES (LOW, MID, HIGH). THE VALUES FOR THE HIGH INTENSITY EVENT ON THE 1990 RIGHT PLOT (MARKED WITH A *) ARE AN UNDERESTIMATE BECAUSE THE SEDIMENT LOAD AND FLOW AFTER THE EXPERIMENT ARE NOT KNOWN DUE TO A BROKEN FIRE HOSE.	32
TABLE 5 DISTANCES OF THE SAND MOVEMENT (BASED ON THE 50 %, 75 % AND 90 % RELATIVE CUMULATIVE TRAVEL DISTANCES FOR THE PARTICLES THAT MOVED, AS WELL AS THE MAXIMUM SAND MOVEMENT, 100 %) IN MM FOR ALL SIX EXPERIMENTAL PLOTS AND ALL THREE SIMULATED RAINFALL INTENSITIES (LOW, MID, HIGH). THE VALUES WERE ROUNDED TO 10 MM INTERVALS. NO DATA IS INDICATED BY N/A.	34
TABLE 6 SUMMARY OF THE EFFECTS OF THE FACTORS STUDIED IN THE THESIS ON SEDIMENT TRANSPORT. NOTE THAT THE LOCALLY OCCURRING SURFACE RUNOFF WAS ONLY OBSERVED AND NOT MEASURED. THUS NO STATISTICAL TESTS COULD BE MADE FOR THAT FACTOR.....	60
TABLE 7 PLOT BORDER LENGTHS A, B, C, D (SEE FIGURE A.1) IN M, AS MEASURED IN THE FIELD, THE ANGLES A (BETWEEN A AND D) AND B (BETWEEN B AND C) IN DEGREE AS WELL AS THE ACTUAL CALCULATED PLOT AREA A_{plot} IN m^2 USING EQUATION (9)....	III
TABLE 8 PEARSON AND SPEARMAN RANK CORRELATIONS FOR THE FOUR SAND DISTANCE MEASURES (BASED ON THE RELATIVE CUMULATIVE TRAVEL DISTANCES: 50 %, 75 %, 90 % AND MAXIMUM DISTANCE) AND THE VALUES OF THE SITE CHARACTERISTICS (SLOPE ANGLE, TORTUOSITY INDEX TI, RANDOM ROUGHNESS RR, VEGETATION COVER, NUMBER OF PLANT SPECIES (SPECIES RICHNESS), SATURATED HYDRAULIC CONDUCTIVITY K_{SAT}) AND THE FIRST TWO PRINCIPAL COMPONENTS (PC1, PC2) OF THE PCA FOR THE THREE RAINFALL INTENSITIES (LOW, MID, HIGH). MARKED IN GREEN ARE THE SIGNIFICANT VALUES (SIGNIFICANCE LEVEL: $\alpha = 0.1$).	IV
TABLE 9 P-VALUES OF PEARSON AND SPEARMAN RANK CORRELATIONS FOR THE FOUR SAND DISTANCE MEASURES (BASED ON THE RELATIVE CUMULATIVE TRAVEL DISTANCES: 50 %, 75 %, 90 % AND MAXIMUM DISTANCE) AND THE VALUES OF THE SITE CHARACTERISTICS (SLOPE ANGLE, TORTUOSITY INDEX TI, RANDOM ROUGHNESS RR, VEGETATION COVER, NUMBER OF PLANT SPECIES (SPECIES RICHNESS), SATURATED HYDRAULIC CONDUCTIVITY K_{SAT}) AND THE FIRST TWO PRINCIPAL COMPONENTS (PC1, PC2) OF THE PCA FOR THE THREE RAINFALL INTENSITIES (LOW, MID, HIGH). MARKED IN GREEN ARE THE SIGNIFICANT VALUES (SIGNIFICANCE LEVEL: $\alpha = 0.1$).....	V
TABLE 10 PEARSON AND SPEARMAN RANK CORRELATIONS FOR THE FOUR SAND DISTANCE MEASURES (BASED ON THE RELATIVE CUMULATIVE TRAVEL DISTANCES: 50 %, 75 %, 90 % AND MAXIMUM DISTANCE) AND THE VALUES OF THE SURFACE RUNOFF	

RATIO AND SEDIMENT LOAD FOR THE THREE RAINFALL INTENSITIES (LOW, MID, HIGH). MARKED IN GREEN ARE THE SIGNIFICANT VALUES (SIGNIFICANCE LEVEL: $\alpha = 0.1$)..... VI

TABLE 11 P-VALUES OF PEARSON AND SPEARMAN RANK CORRELATIONS FOR THE FOUR SAND DISTANCE MEASURES (BASED ON THE RELATIVE CUMULATIVE TRAVEL DISTANCES: 50 %, 75 %, 90 % AND MAXIMUM DISTANCE) AND THE VALUES OF THE SURFACE RUNOFF RATIO AND SEDIMENT LOAD FOR THE THREE RAINFALL INTENSITIES (LOW, MID, HIGH). MARKED IN GREEN ARE THE SIGNIFICANT VALUES (SIGNIFICANCE LEVEL: $\alpha = 0.1$)..... VI

1 Introduction

Soils are the foundation for all life on earth. They are the growing substrate for plants, habitat for microorganisms and provide various ecosystem services, such as biomass production, nutrient stocks and water storage (Dominati *et al.*, 2010; Food and Agriculture Organization of the United Nations (FAO), 2015). Soils are the start of the food chain on land systems and, hence, they are important for the global food production (Capra, 2013; Raclot *et al.*, 2018). However, global change, especially climate and land use change, may lead to loss and degradation of soils, which in turn creates challenges for the global food production (FAO, 2015). The warming climate changes the variability and intensity of rainfall events (Nearing *et al.*, 2004; Anache *et al.*, 2018; Raclot *et al.*, 2018). More intense rainfall results in larger raindrops and a higher kinetic energy (Evans, 1980), which impacts runoff processes and soil erosion (Nearing *et al.*, 2004; Anache *et al.*, 2018). If the intensity is higher than the infiltration capacity, it will also lead to surface runoff (infiltration excess overland flow; Horton, 1933), which can further increase soil erosion. Soil erosion displaces or completely removes fine materials, organic matter and nutrients, leads to the loss of fertile soil, disturbance of ecosystems, and increases the potential for landslides (Lee and Heo, 2011). It might also cause more suspended sediment in water bodies, leading to decreasing water quality (Bilotta and Brazier, 2008). Moreover, it may result in a decrease of biodiversity in both flora and fauna (El Kateb *et al.*, 2013). Although many studies have quantified erosion, there are still research gaps within the area of soil erosion, especially in the understanding of processes and interactions (Poesen, 2018). It is essential to understand the underlying processes that drive or influence erosion in order to successfully protect natural and anthropogenically influenced areas.

1.1 Soil erosion

Soil erosion describes the detachment and transport (i.e. the removal) of sand, silt, clay, organic particles from any surface. During rainfall events, particles on the soil surface are mainly detached and transported via two hydrological processes: (a) rain splash and (b) flowing water on the surface.

- (a) The erosive energy (also referred to as kinetic energy) of a raindrop depends on its size (and hence mass) and impact velocity. During the impact, the energy or momentum is transferred to the ground and, if large enough, loose soil material close to the surface is ejected. This process is commonly referred to as '*splash erosion*' (Evans, 1980; Bryan, 2000; Long *et al.*, 2014; Bracken *et al.*, 2015).

- (b) Surface flow or overland flow describes the water flowing on the soil surface. Comparable to streams, water easily transports loose particles. Water can flow over the surface as sheet wash, inter-rill flow, rill flow and gully flow (Evans, 1980; Bryan, 2000; Bracken *et al.*, 2015).

The available kinetic energy to detach and transport particles depends on the amount of surface runoff, which depends on the infiltration rate and rainfall intensity. The saturated hydraulic conductivity describes the maximum infiltration rate at saturated conditions and thus determines the potential for infiltration excess runoff (Zimmermann *et al.*, 2013) and thereby erosion. Slope angle is generally considered one of the main factors that determines soil erosion on hillslopes. On slopes overland flow and rain splash can transport particles. The potential for higher runoff, and thus also higher erosion rates, increases with slope angle (Evans, 1980; Cerdà and García-Fayos, 1997; El Kateb *et al.*, 2013). The term microtopography refers to the topography of the soil surface at the micro scale (centimeters) and determines the surface roughness, which is a measure of roughness of the considered surface. Surface roughness influences the velocity and routing of surface flow and is, thus, also related to soil erosion (Evans, 1980; Bertuzzi *et al.*, 1990; Battany and Grismer, 2000; Liu and Singh, 2004). Furthermore, water and particles may get trapped in depressions, decreasing the surface runoff and erosion.

The portion of vegetation cover but also the degree of species richness (henceforth called plant species richness) may affect soil erosion rates (see e.g. Zhou *et al.*, 2008; Rodrigo Comino *et al.*, 2016). Higher vegetation cover and also a higher plant species richness tend to lower soil erosion rates (Evans, 1980; Berendse *et al.*, 2015). Vegetation, as well as residues, on hillslopes act as a buffer and lower the total kinetic energy of raindrops on the soil at the moment of impact so that fewer particles can be eroded and transported. In contrast, on bare soils, raindrops contribute to the surface compaction and easily erode soil particles (Evans, 1980; Fullen, 1991; Battany and Grismer, 2000; El Kateb *et al.*, 2013). Vegetation can also lead to higher infiltration rates, mainly because of stronger soil aggregates (Evans, 1980) and routing of the water along preferential flow paths (see e.g. Beven, 2018). Plant species richness, furthermore, influences soil stability. Soils with diverse vegetation have more stable soil aggregates and a higher rooting density. Better soil stability, results in lower erosion rates (Pohl *et al.*, 2009). However, the effect of vegetation on runoff generation, and thus also sediment transport, is still controversial at plot scale (Liu *et al.*, 2019).

Overall, there are many processes and characteristics influencing soil erosion and sediment transport either positively or negatively. A summary of the described processes and their feedbacks is shown in Figure 1.1.

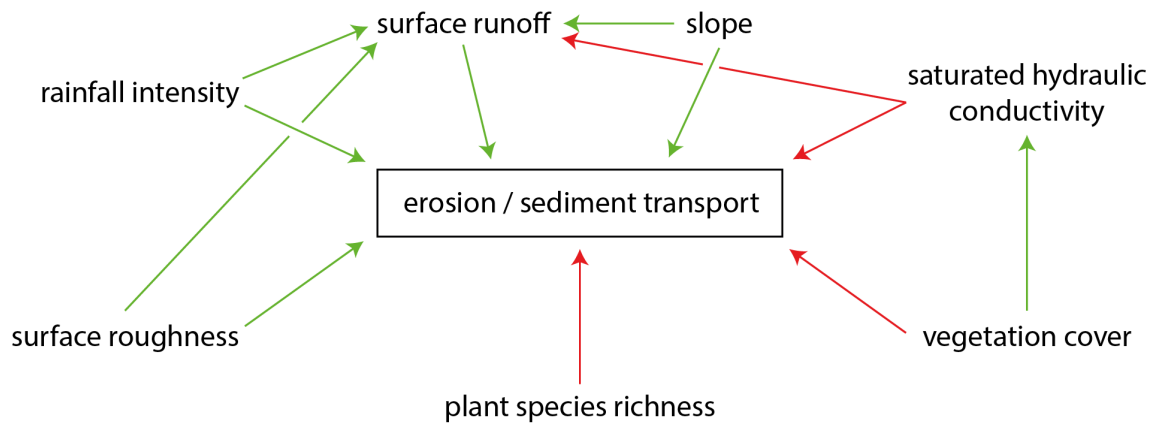


Figure 1.1 Sketch summarizing the effects of the rainfall intensity, the surface runoff and the site characteristics (vegetation cover, plant species richness, slope, surface roughness, saturated hydraulic conductivity) on erosion and/or sediment transport. Green arrows represent positive and red arrows negative feedbacks.

1.2 Surface connectivity

Erosion - or more precisely sediment transport - is linked to the flow paths on the surface. A recently introduced term related to the physical variability of water flow on hillslopes is 'connectivity'. Connectivity refers to how different catchment elements are connected to each other (Ali and Roy, 2010). However, in the literature, the term is used in ambiguous ways (Bracken and Croke, 2007; Michaelides and Chappell, 2009; Blume and van Meerveld, 2015). According to Bracken and Croke (2007) 'surface connectivity' includes the connectivity of landscape, hydrology and sediment. 'Landscape connectivity' refers to the coupling of different landforms. 'Hydrologic connectivity' refers to the coupling or linkage of different catchment regions by water flow (Blume and van Meerveld, 2015), which influences erosion rates and the pathways for sediment transport. It is, thus, directly related to 'sediment connectivity', which is the detachment and connected physical transport of sediments, nutrients, pollutants etc. through the watershed (Bracken and Croke, 2007; Bracken *et al.*, 2015). Surface hydrological connectivity is of great importance for soil erosion, as it entails hydrological processes and the corresponding transport of energy, nutrients, organic matter and other particles across the catchment during precipitation events (Stieglitz *et al.*, 2003).

So far, surface hydrological connectivity is still poorly understood, partly due to lack of proper methods that quantify hydrological but also sediment connectivity (Mayor *et al.*, 2008; Ameli and Creed, 2017). Hydrologic connectivity is typically assessed at three different spatial scales: patch (plot), hillslope, and catchment scale (Bracken and Croke, 2007). At meso or macro scales (hillslope and catchment) it can be estimated by the determination of the drainage network with satellite images using near infrared and short-wave infrared bands (Ares *et al.*, 2016), chemical tracers or based on Digital Terrain Models (DTMs; Golden *et al.*, 2017). The latter can be built

using remote sensing data (e.g. lidar data) and Geographical Information Systems (GIS). Based on DTMs the surface water flow accumulation is calculated based on topographical flow directions (e.g. with the $D-\infty$ method, see Tarboton, 1997). Models, which explicitly simulate water flow on the surface, are also used for the estimation of hydrological connectivity (Chu *et al.*, 2013; Peñuela *et al.*, 2015; Golden *et al.*, 2017). However, on micro scale (plot scale) it is difficult to obtain accurate results based on models or DTMs because of model assumptions and often low spatial resolutions.

1.3 Artificial tracer experiments and fluorescent tracers

Many studies have used artificial rainfall experiments for the assessment of erosion, sediment transport and overland flow (Arnáez *et al.*, 2004; Scherrer *et al.*, 2007; Tauro *et al.*, 2012b; Butzen *et al.*, 2014; van Meerveld *et al.*, 2014; Guzmán *et al.*, 2015; Tauro *et al.*, 2016; Prosdocimi *et al.*, 2017). Artificial rainfall experiments have the great advantage of having full control over one variable (rainfall intensity), whereas its influence on other variables can be investigated. Guzmán *et al.* (2015) studied sediment movement on agricultural fields by the use of magnetite, hematite and goethite tracers. However, tracer concentrations were only measured in sediment load of the runoff samples below the plots and no flow paths on the plot surfaces were recorded. Some studies also focused on the movement of water and sediment on experimental plot surfaces. For example, Prosdocimi *et al.* (2017) studied sediment transport at plot scale by the use of pre and post event DTMs (spatial resolution of 0.01 m). For assessing sediment connectivity they used a DTM based index (*index of connectivity*), defined by Cavalli *et al.* (2013). This index only provides potential connectivity between source and sinks of a catchment or plot (Cavalli *et al.*, 2013). Hardy *et al.* (2017) studied for the first time the movement of individual sediment particles (under laboratory conditions) using a novel real time particle tracking technique but did not refer to surface connectivity. However, studies concerning surface hydrological connectivity and sediment transport (as an indicator for erosion) on hillslopes in alpine regions at plot scale are lacking.

In this study, artificial rainfall experiments were carried out and a new method for the spatial quantification of surface hydrological connectivity and sediment transport at plot scale was tested. Coating sediment particles with fluorescent tracers to study sediment transport was already tested and declared suitable by Yasso (1966). Such particle tracers were initially used to trace sediment movement in coastal regions. Badr and Lotfy (1999) for example studied the drift rate of beach sand along the surf zone in the Nile river delta. Klein *et al.* (2007) examined on- and offshore sediment transport along the coast of Israel. Kato *et al.* (2014) investigated sand movement in a river tidal flat in Japan. Particle tracers have also been used in flowing water on land,

e.g. in streams (Tauro *et al.*, 2012a). Tauro *et al.* (2012b) used a fluorescent particle tracer (buoyant polyethylene balls with diameters of 75 - 1180 μm) on an artificial hillslope to trace overland flow. Tauro *et al.* (2016) used the same particles (75 - 1180 μm) and studied processes on hillslopes that drive streamflow generation. However, the particles of both studies were not representative of the underlying soil material because of their low density and high buoyancy. Other studies have tested more suitable materials, such as clay (Hardy *et al.*, 2016), sand (Hardy *et al.*, 2017) or a mixture of several glass particle sizes (44 - 2000 μm ; Young and Holt, 1968). Hardy *et al.* (2019) were the first to study sediment transport on hillslopes using tracer materials with similar particle sizes and density as the soil material itself. They used it for the detection of soil redistribution by tillage on arable farmland. Despite using particle tracers to study sediment transport, none of the mentioned studies above used it to determine surface connectivity.

A fluorescent particle tracer was chosen in this study because of better particle detection on heterogeneous surfaces. In fluorescent materials, atoms absorb the energy of photons. Thereby, the electrons jump to higher orbitals. The new state is unstable, and the electrons switch back to their original orbitals by emitting energy. The released wavelengths are higher, as energy was lost during this process. The emitted light is called '*fluorescence*' (Usai and Diaspro, 2013).

1.4 Research objectives and questions

The goal of this thesis is to examine the use of a fluorescent sand tracer to determine surface hydrological connectivity and sediment transport. More specifically, the study aimed to address the following research questions:

- (1) Is fluorescent quartz sand useful for tracing water and sediment movement?
- (2.1) Do rainfall intensity, surface runoff and site characteristics (vegetation cover, number of plant species, slope angle, surface roughness, saturated hydraulic conductivity) affect sediment transport on hillslopes at plot scale?
- (2.2) And if so, how do they affect sediment transport?

The study took place in the central Swiss Alps, close to Sustenpass, and was part of the larger research project HILLSlope And Chronosequence Process Evolution (HILLSCAPE; see also chapter 2). The Swiss Alps are commonly considered as the '*water tower*' of Europe. Switzerland provides 6 % of Europe's fresh water supply (Federal Office for the Environment FOEN, 2018) and it

is crucial to understand underlying hydrological processes at its origin to maintain high water quality standards.

Within the study six experimental plots were created. For each plot various site characteristics that may affect sediment transport were determined, namely vegetation cover, number of plant species, slope angle, surface roughness and saturated hydraulic connectivity. During the rainfall application (at three different intensities) surface runoff and sediment concentrations were measured at the lower plot boundary to determine sediment load.

The sand tracer has a representative diameter (sand size) and was applied as a line source on the experimental plots. The distribution of the sand after the irrigation was thought to reveal the flow paths of overland flow and, hence, also the paths for sediment transport. In contrast to buoyant polyethylene particles, quartz sand is deposited along the flow paths (like natural soil particles) and is, thus, still visible after the experiment. Furthermore, no real time observation is needed (as it was for Tauro *et al.*, 2012b, 2012a, 2016, Hardy *et al.*, 2016, 2017) in order to determine surface hydrological connectivity. Simultaneously, the distribution of the sand also provides information about travel distances, which was used as information about sediment transport. The maximum distance of the sand movement is considered to be a measure for sediment transport.

2 HILLSCAPE

The thesis is set within the international and interdisciplinary research project HILLSCAPE, which is a collaboration between the University of Zurich, the University of Freiburg and the German Research Centre for Geosciences (GFZ). The project is funded by the Swiss National Science Foundation (SNSF) and the Deutsche Forschungsgemeinschaft (DFG).

Within the scope of HILLSCAPE natural hillslopes in the Swiss Alps are studied under experimental conditions. Overall, it focusses on the lateral and vertical redistribution of water and the feedbacks between soil development, hydrology and vegetation (van Meerveld *et al.*, 2018). The overall research question of HILLSCAPE is: “How does the hillslope feedback cycle evolve in the first 10,000 years and how is this related to the evolution of hillslope structure, including plant cover?” (van Meerveld *et al.*, 2018).

A sub-question to be answered within the scope of the HILLSCAPE project (within the PhD project of Fabian Maier) is, if erosion rates increase or decrease with soil age. Generally, with increasing soil age, vegetation increases, resulting in more soil stability from the higher rooting density and more stable aggregates (Pohl *et al.*, 2009). The soils thicken and the roots grow deeper, leading to a higher water storage capacity and, thus, also higher evapotranspiration (Tromp-van Meerveld and McDonnell, 2006). These changes are expected to decrease surface runoff, and thus to also decrease soil erosion. However, Lohse and Dietrich (2005) suggested that, due to clay accumulation in more developed soils, the hydraulic conductivity decreases and lateral water flow increases. This might lead to higher surface runoff and higher erosion rates.

Due to the interdisciplinarity of the HILLSCAPE project, data from other research fields, such as geochronology and geobotany, could be included for the analysis in this master thesis.

The results of this master thesis will further be used beyond the thesis for the answering of other questions within the HILLSCAPE project. They will help to understand how sediment on hillslopes is transported and how other factors affect it. The findings will complement later published results, mainly from Fabian Maier (University of Zurich, Department of Geography) and Alessandra Musso (University of Zurich, Department of Geography), and help to answer the sub-question related to soil erosion and moraine age.

Further information about the HILLSCAPE project can be found on: <http://hillscape.ch/>

Visual impressions and a general explanation of the HILLSCAPE project can also be found in the official HILLSCAPE video of Sustenpass: <https://www.youtube.com/watch?v=TEytd77tLk>

3 Study Site

3.1 Study area

The study area is located in the forefield of the Steingletscher (south west of Sustenpass; 46° 43' N, 8° 25' E), an Alpine headwater catchment in the westernmost part of canton Bern (Switzerland). The area was chosen because of the proximity to the glacier and the well preserved moraine remnants beyond the visible little ice age extent of the glacier (King, 1974). Although the HILLSCAPE project studied four moraines (with three experimental plots on each), the experiments described in this study took place on only three moraines (Figure 3.1) because of the dense vegetation, mainly alpine roses (*Rhododendron ferrugineum*) on the oldest moraine, that limited visibility and precluded the analysis of fluorescent sand tracer transport. The selected moraines are located within a small area (maximum 1 km apart from each other), ensuring very similar climatic conditions. However, the moraines are of different ages, leading to different stages in soil and vegetation development. The elevation of the selected moraines varies between 1870 and 1980 m above sea level (m a.s.l.).

The climate in the study area is typical for alpine regions: humid and cold. The mean annual precipitation (1981 – 2010) at the closest MeteoSwiss weather station (Meiringen, 598 m a.s.l.) is 1375 mm (MeteoSwiss, 2016a). The mean annual precipitation for the same period for the closest MeteoSwiss weather station at a similar elevation (Grimsel Hospiz, 1980 m a.s.l.) is 1856 mm (MeteoSwiss, 2016b). The precipitation at Grimsel Hospiz is on average slightly higher during the winter than in the summer (1060 mm from November to April vs 800 mm from May to October). The mean annual temperature at Grimsel Hospiz is 1.9 °C and, thus, snowfall events are common (MeteoSwiss, 2016b).

The bedrock at the Sustenpass mainly consists of metamorphic silicate rocks like pre-Mesozoic metagranitoids, gneisses and amphibolites (Schimmelpfennig *et al.*, 2014). The moraine material consists of the same material, which has a rather low amount of nutrients. Podzols are the most dominant soil type in the region (King, 1974; Heikkinen and Fogelberg, 1980). However, soil classification within the HILLSCAPE project by Alessandra Musso suggests that the dominant soils on the moraines are rather Cambisols in the lower parts (older moraines) and Leptosols in the higher parts (younger moraines) of the research area (Musso *et al.*, in review). Leptosols are thin soils with AC profiles, where the C-horizon represents the parent material, here moraine material. These soils are typical for mountainous regions, especially for pro-glacial areas (Temme and Lange, 2014; IUSS Working Group WRB, 2015). Cambisols and Podzols are further developed stages of Leptosols and contain more soil layers. In Cambisols the parent material is moderately weathered, and a typical brownish B-horizon was formed. Podzols are characterized by their

bleached, grey eluvial horizon (E-horizon) and one or several illuvial horizons (B-horizons). Podzols are completely developed soils and are, thus, only found on older moraines (Zech *et al.*, 2014; IUSS Working Group WRB, 2015).

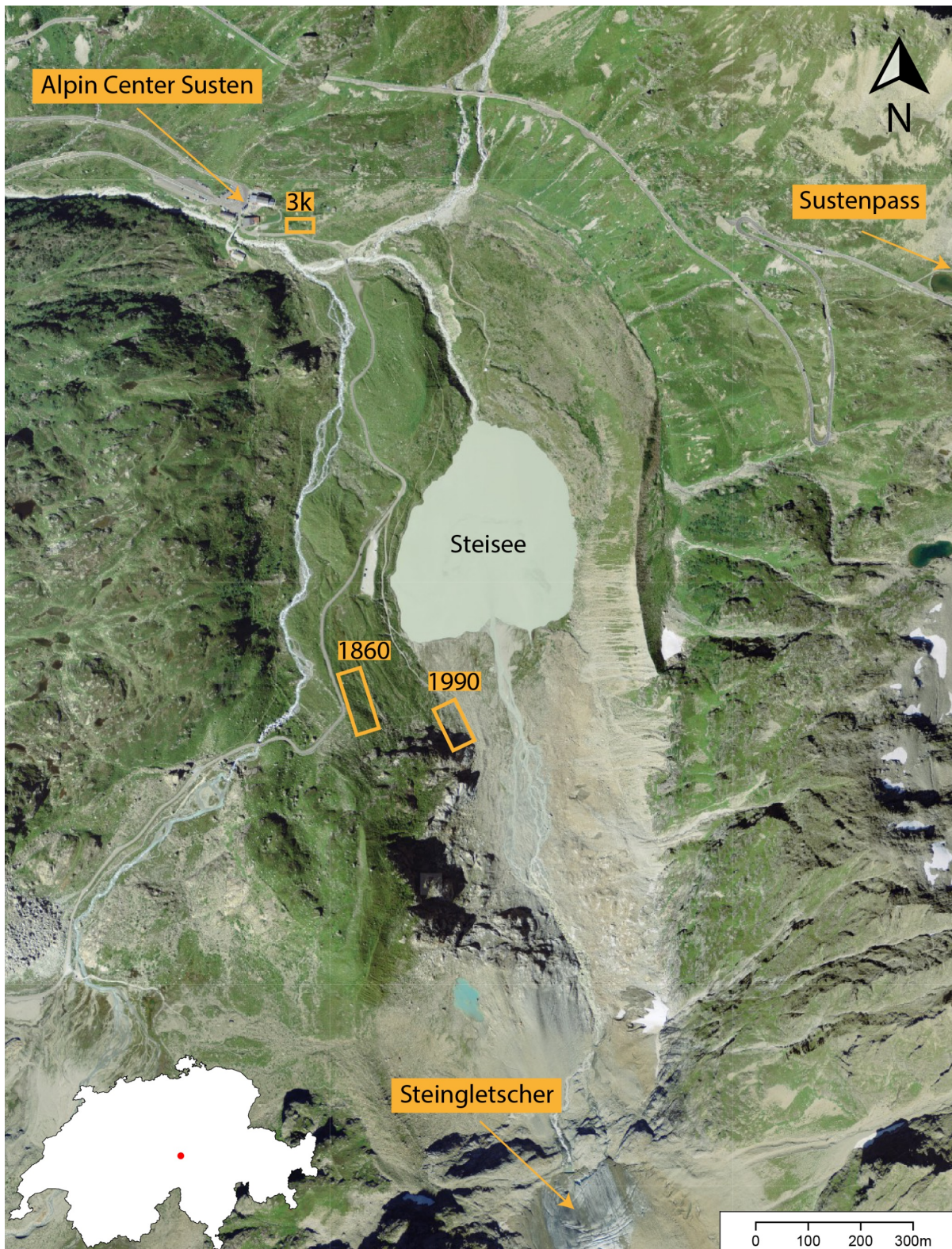


Figure 3.1 Study area in the forefield of the Steingletscher (south west of Sustenpass) in the westernmost part of canton Bern (Switzerland). The location of the three moraines (3k, 1860, 1990) are indicated. The map was modified from Swisstopo (Federal Office of Topography swisstopo, 2019a)

3.2 Study sites

The study took place on six different plots on three different moraines (Figure 3.1, Figure 3.2 and Table 1). The plots were chosen based on a vegetation survey (summer 2017) by Konrad Greinwald (University of Freiburg, institute of biology and geobotany), so that they covered the variability of the vegetation on each moraine. On each moraine initially three plots were chosen for the overall HILLSCAPE experiments. The three plots varied from the lowest to the highest vegetation complexity (cover and number of plant species) and the level of bareness. One plot was chosen where the least vegetation complexity and highest bareness level was observed. One plot represented the other extreme and was chosen where the vegetation complexity was highest and the bareness lowest for the moraine. The last plot location was chosen where the vegetation complexity was in the middle of the two extremes. The partly dense vegetation and the occurrence of shrubs, however, limited visibility and precluded the analysis of fluorescent sand tracer transport from some plots. Thus, only six of the nine plots were used in this study.

1. The oldest moraine (3k) is about 3000 years old, dated by Schimmelpfennig *et al.* (2014) to 2870 ± 120 a. It is located just behind the Alpin Center Susten, Hotel Steingletscher (see Figure 3.1), at 1870 m a.s.l., is south-east exposed and has an average slope angle of 25° . Podzols and Cambisols are found below the fully vegetated moraine. The topsoil mainly consists of sandy loam (Figure 3.3). Forbs and grasses cover the moraine. Only one plot (called 3k) was studied on this moraine (the plot with the lowest shrub cover and second lowest vegetation cover).
2. The second oldest moraine is located next to lake Stein and represents a typical moraine of the little ice age (1860 AD). It has been exposed for about 160 years (Musso *et al.*, in review). The moraine is exposed to north-east and has an average slope angle of 31° . It is situated at 1980 m a.s.l and soils are Leptosols. The topsoil material is a sandy clay loam (Figure 3.3). Similar to the 3k moraine, the 1860s is fully covered by vegetation, dominated by forbs and grasses. Shrubs are common as well. Two plots (1860 left, 1860 right) were studied on this moraine (the two plots with the lowest shrub cover).
3. The youngest moraine has only been exposed for about 30 years. Using aerial photographs from Swisstopo (Federal Office of Topography swisstopo, 2019b) it was dated to 1990 AD. It is located at the foot of the hillslopes draining towards the alluvial plain of the Steingletscher at 1950 m a.s.l. It is exposed towards north-east and has an average slope angle of 26° . In contrast to the two older moraines, it is significantly less vegetated. The surface mainly consists of moraine material (unrounded blocks of all sizes mixed with fine

material). Soil development has hardly started but partly very thin Leptosols are found. The topsoil is full of sand and classified as loamy sand (Figure 3.3). Nevertheless, forbs and grasses occur and dominate over ferns, sedges, shrubs and trees, which are hardly present. All three plots were studied on this moraine (1990 left, 1990 middle, 1990 right).

The plots on the two oldest moraines (3k, 1860) were strongly vegetated while the plots on the youngest moraine (1990) had significantly less vegetation. This means that three plots had a high vegetation cover and three plots a low vegetation cover (Figure 3.2 and Table 1). The plots with low vegetation cover in turn were strongly dominated by moraine material with rocks in different sizes. It is acknowledged that a sample size of six plots is low and precludes statistical analysis, but the setup was very time consuming (see chapter 4.1) and the creation of more experimental plots was thus not possible

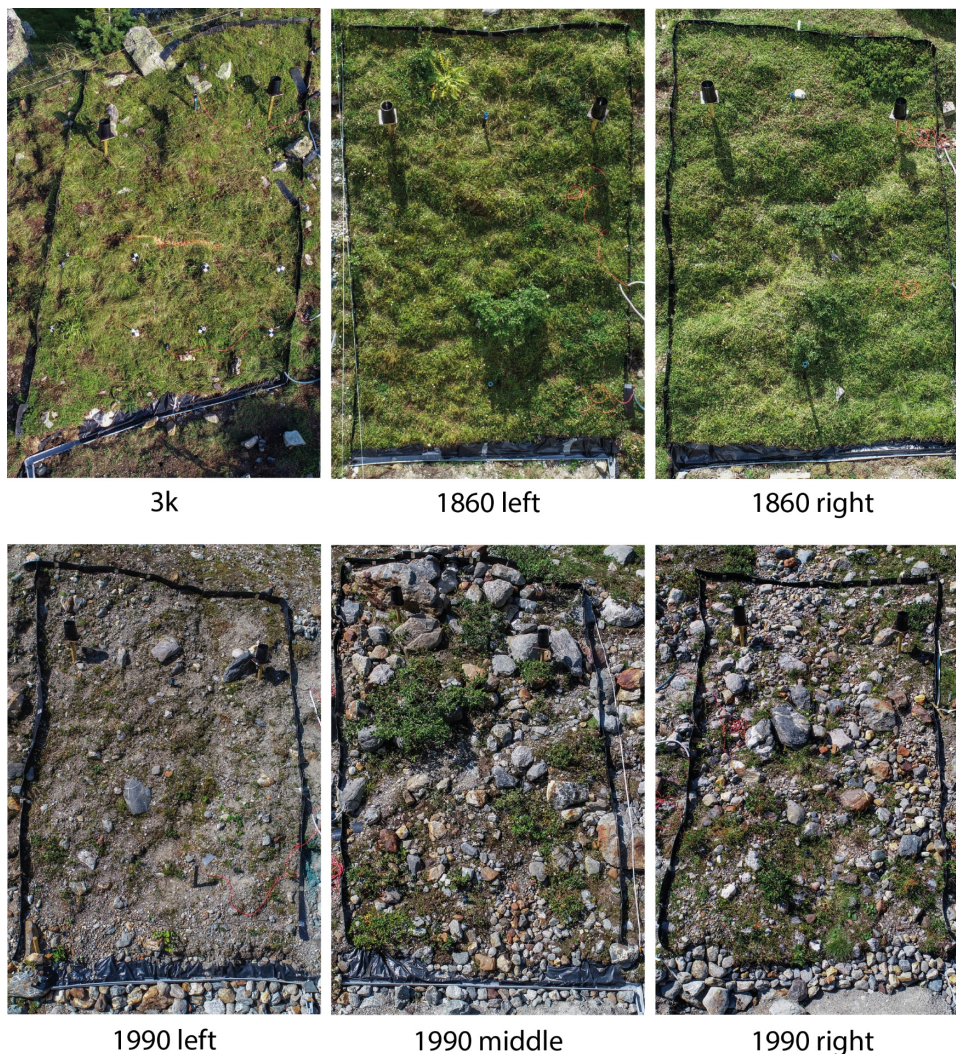


Figure 3.2 The six experimental plots studied in this thesis: 3k, 1860 left, 1860 right, 1990 left, 1990 middle and 1990s right. The vegetation cover is clearly higher at the three older plots than on the three 1990 plots.

Table 1 Age in years, the actual plot size in the field (see Appendix 1), the degree of vegetation cover and the slope angle in degree (see chapter 4.3.2) of all six experimental plots (3k, 1860 left, 1860 right, 1990 left, 1990 middle, 1990 right) on the three studied moraines (3k, 1860, 1990).

plot name	moraine	age [years]	actual plot size [m ²]	vegetation cover	slope angle [°]
3k	3k	3000	23.29	high	25.4
1860 left	1860	160	25.01	high	36.6
1860 right	1860	160	24.70	high	24.5
1990 left	1990	30	23.69	low	33.0
1990 middle	1990	30	23.60	low	23.8
1990 right	1990	30	24.63	low	21.8

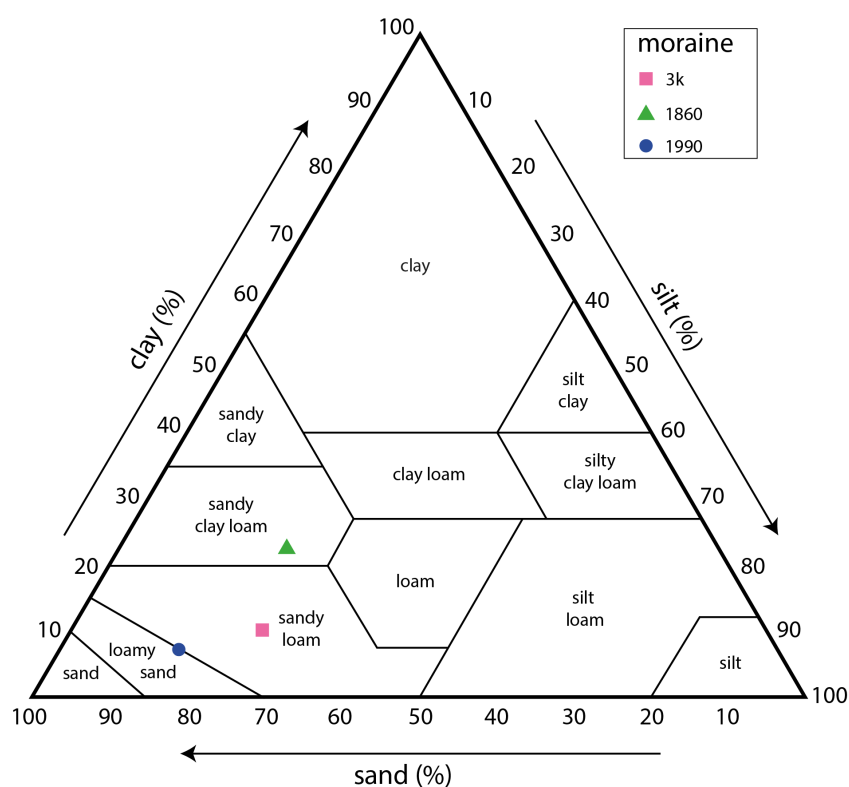


Figure 3.3 The texture of the topsoil of the three moraines (3k, 1860, 1990) in the grain size diagram modified after IUSS Working Group WRB (2015). The grain size fractions were obtained from Musso et al. (in review). All three moraines were rather sandy.

4 Methods

4.1 Experimental plots

The experimental plots were approximately 4 m by 6 m in size (see also Table 1). Plastic sheets with a height of about 20 cm were installed around the plots to prohibit surface water flow in and out of the plot (Figure 4.1). At the lower end of the plots surface and subsurface flow was collected. For the subsurface flow, drainage mats were placed vertically into the soil, down to the C-horizon. This water was guided to an Upwelling Bernoulli Tube (see also Stewart *et al.*, 2015), where the water flow was recorded (data not used in this thesis). A roof covered the gutters of surface and subsurface flow to avoid mixing with rainfall. At each plot, two tipping bucket rain gauges and three sprinklers were installed. Soil moisture and perched groundwater levels were measured as well but were not used in the analysis described in this thesis either.

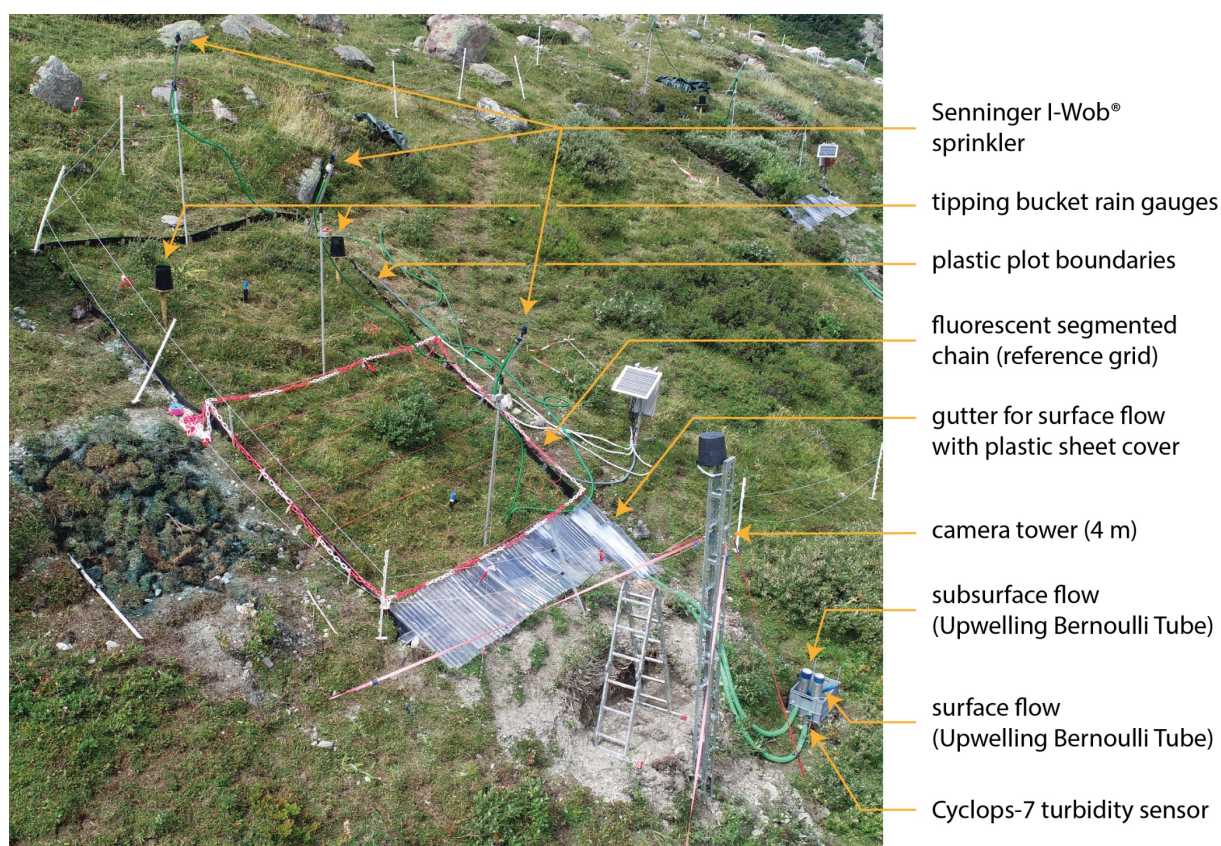


Figure 4.1 Setup of the experimental plots (here 1860 left), including three Senninger I-Wob® sprinklers, tipping bucket rain gauges, plastic boundaries around the plot, a gutter at the bottom of the plot, hoses (green) to route the surface and subsurface flow to the Cyclops-7 turbidity sensor and the Upwelling Bernoulli Tubes. The fluorescent segmented chain and the horizontal lines, as well as the camera tower to determine the fluorescent sand transport are shown as well.

4.2 Rainfall simulation experiments

4.2.1 Rainfall application

On each experimental plot, three poles with Senninger I-Wob® sprinklers were installed along the center line of the plot: one at the upper end, one in the middle, and one at the lower end. The I-Wob sprinklers provide a uniform rainfall intensity within a 4 m sprinkling radius (van Meerveld *et al.*, 2014). The drop size distribution was measured with the oil method after Eigel and Moore (1983). The observed drop sizes (median and range) were similar to those of natural events in temperate regions, meaning that they were representative and are suitable to study erosion processes (Baird, 2008; van Meerveld *et al.*, 2014).

Three rainfall simulations with high intensities were carried out on each plot. The design intensity for each simulation corresponded to the predefined Return Periods (RPs) of approximately 2, 20 and 100 years. For the region of Sustenpass the rainfall intensities were estimated by Ilja van Meerveld (University of Zurich, Department of Geography) and Markus Weiler (University of Freiburg, Chair of Hydrology) using the Hydrological Atlas of Switzerland (see HADES, 2019). However, due to variation in the slope angle and pressure differences, as well as wind induced redistribution of the falling raindrops, rainfall intensity during an experiment varied (see Table 2):

- Low intensity (RP = 2 years)
 - design intensity: 20 mm/h
 - actual intensities: 13 – 24 mm/h
- Mid intensity (RP = 20 years)
 - design intensity: 40 mm/h
 - actual intensities: 38 – 69 mm/h
- High intensity (RP = 100 years)
 - design intensity: 60 mm/h
 - actual intensities: 59 – 95 mm/h

The goal was to use approximately the same amount of water for all experiments (design infiltration on the plot: ~20 mm; actual range: 15 – 58 mm). In terms of experimental runtime, the low intensity run took 55 – 75 min, the mid intensity 36 - 50 min and the high intensity 34 - 40 min. For the low intensity event only the middle sprinkler was used. For the mid intensity the middle and upper sprinklers were used. For the high intensity all three sprinklers were used at the same time.

Table 2 Actual rainfall intensities for the low, mid, and high intensity experiments for all six experimental plots (3k, 1860 left, 1860 right, 1990 left, 1990 middle, 1990 right).

	3k	1860 left	1860 right	1990 left	1990 middle	1990 right
actual low intensity [mm/h]	13	21	20	24	15	15
actual mid intensity [mm/h]	69	42	44	39	38	70
actual high intensity [mm/h]	89	81	95	86	70	59

The irrigation experiments were conducted in August and early September 2018. All experiments were first conducted on the 3k moraine, then on the 1860s moraine and last on the 1990s moraine. The rainfall simulations for each moraine were carried out over a three-day time period, starting with the low intensity simulation on day 1, the mid intensity event on day 2, and the high intensity event on day 3. All plots on a moraine were irrigated on the same day. The antecedent conditions for all experiments were assumed to be similar after 24 h of no rain (interval between rainfall simulations on the experimental plots). Within this time soil moisture is assumed to have decreased back to the field capacity (Markus Weiler, personal communication, July, 2018). In case of natural rainfall between the experiments, the plots were covered with tarps to minimize the influence of additional water to the soil moisture content. The water used for irrigation was collected prior to the experiments from the near glacial stream and stored in two 5000-liter water reservoirs. Using fire hose, the water was transported from the reservoirs to the plots during the experiments.

4.2.2 Surface runoff

For the surface runoff measurements, plastic foil was inserted just below the sod at the lower end of the plot to capture all surface flow (generally < 5 cm from the soil surface; see also Figure 4.2). The foil guided the water to a gutter, which was connected to an Upwelling Bernoulli Tube (designed after Stewart *et al.*, 2015), where the water level was recorded using a Keller DCX-22-CTD water level logger. The surface runoff measurements thus include surface runoff and very shallow (biomat) flow. The water level could be converted to flow rates due to the known geometry at the outflow of the Upwelling Bernoulli Tube. The total surface runoff volume was based on the volume of water that flowed through the Bernoulli Tube during the experiment (V_{ST}) and the remaining water in the Bernoulli Tube (V_{BT}) as well as the supply pipe (V_{pipe}). This was related to the average of the rainfall measured at the two rain gauges inside the plots (P = actual rainfall volume). As the plots did not perfectly meet a rectangle with the dimensions of 4 m × 6 m, also the actual plot area (A) was calculated. This was done using the true measured lengths of the

plot borders and the angles in between (see Appendix 1). The percentage of surface runoff, henceforth also called surface runoff ratio (r_{sf}), was calculated as follows:

$$r_{sf} = \frac{V_{sr} + V_{BT} + V_{pipe}}{P * A} \quad (1)$$

The data for the surface runoff measurements was provided by Fabian Maier.

4.2.3 Sediment concentrations

The turbidity of the surface runoff was measured using Cyclops-7 turbidity sensors (Turner designs). They were installed in the hose between the gutter at the end of the experimental plots and the Upwelling Bernoulli Tubes (see Figure 4.1 and Figure 4.2). They recorded the turbidity in Nephelometric Turbidity Units (NTUs) during the experiments. A calibration curve (i.e., the correlation between the NTU measurements and the actual sediment concentration in g/l) was established for each moraine. Six known amounts of soil were added into a predefined amount of water, the solution was continuously stirred and the turbidity (in NTUs) was measured using a Cyclops-7 turbidity sensor. Using the NTU values (in 1 min steps) and the calibration curve, the sediment concentration was determined, which was then combined with the measured surface runoff (l/min) to obtain the actual sediment load per plot and experiment.

The sediment load was also measured in water samples (using filters), collected in the surface runoff below the plot. However, most sediment was trapped in the hose or the Upwelling Bernoulli Tube and the obtained sediment loads were clear underestimates. They were, hence, not used for the analysis.

The turbidity and surface runoff measurements, as well as the calibration were done by Fabian Maier. The soil samples of the moraines were collected by Alessandra Musso.

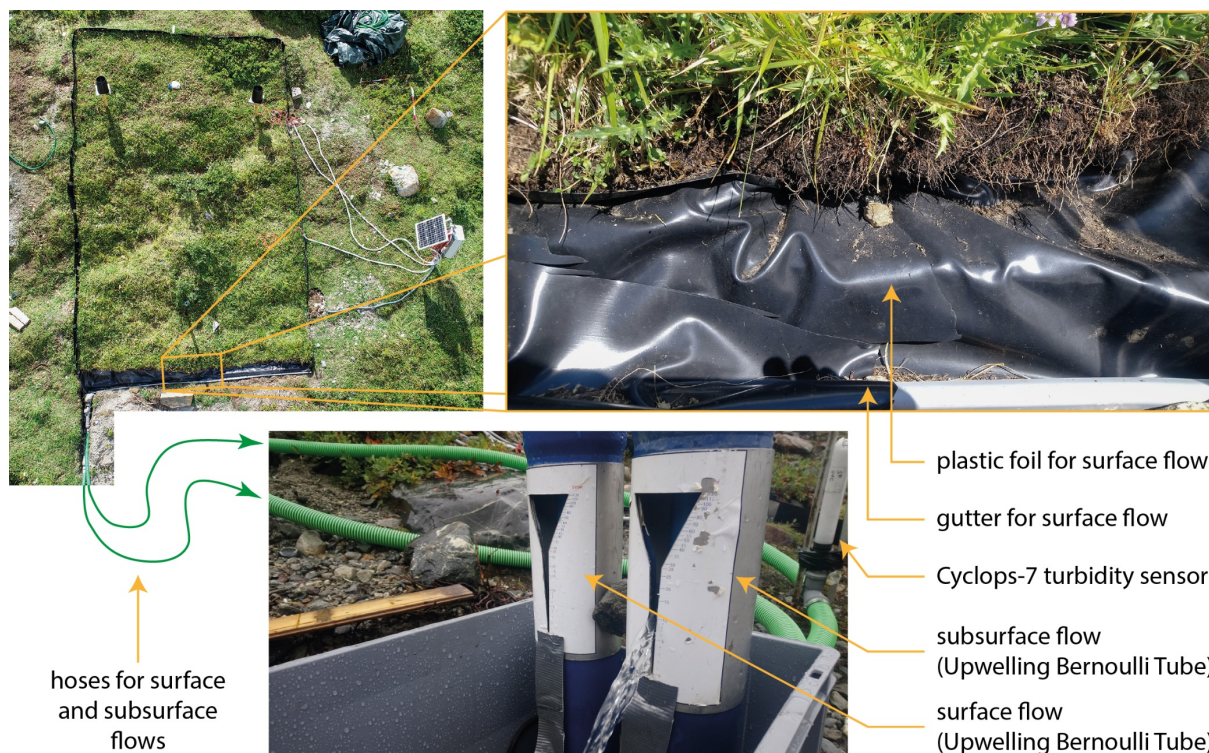


Figure 4.2 Setup for the subsurface and surface flow measurements for the experimental plots, including a gutter at the bottom of the plot, hoses (green) to route the surface and subsurface flow to the Cyclops-7 turbidity sensor and the Upwelling Bernoulli Tubes. The photos of the gutter and the Upwelling Bernoulli Tubes were taken by Fabian Maier.

4.2.4 Sediment transport

In order to study sediment transport (and thus erosion) on the experimental plots, a fluorescent glow in the dark decorative sand (hereafter only called fluorescent sand) was used as particle tracer. Orange sand was used for the low intensity, green for the mid intensity and blue for the high intensity events. The sand consists of quartz sand, with a particle size of 300 – 500 μm , coated in the glow in the dark powder 'TAT 33', which consists of alumina and rare earth metals (Noxton, 2019). The particle sizes are typical for the topsoils on the moraines of the Steingletscher (see also Figure 3.3). 10 – 20 % of the soil material near the surface had the same size class as the used sand (see Musso *et al.*, in review, for grain size distributions). The fluorescent sand is produced by the Noxton™ company in the Ukraine. A more detailed description of the ingredients of TAT 33 is not available. According to Noxton™ (2019) it is water resistant, inert, non-toxic and non-radioactive.

The sand was applied as a line source on the soil surface on the lower half of the experimental plots prior to each irrigation experiment. The application on the lower half was chosen because of the larger probability of surface runoff occurrence compared to the upper half. The lines on the 3k and 1860s plots were 1.55 m long (1 kg sand). The lines on the 1990s moraine were 3.1 m long (2 kg sand). All lines were about 3 - 5 cm wide and ~2 cm high. On the plots with higher vegetation

cover sand was expected to move less and thus only half of the sand amount was used, resulting in half of the line's length. In contrast, the surface variability on the 1990s plots was larger (because of rocks). To include this variability, longer sand lines were useful.

On the 3k plot only one sand line (orange for the low intensity rainfall simulation) was used. Due to very little sand movement after the first rainfall simulation, it was expected to behave similar for the mid and high intensity rainfall simulations and no further lines (green and blue) were applied in order to save resources.

Around the plot an orange-white 0.5 m segmented plastic chain was installed (Figure 4.1). Additionally, thin fluorescent ropes were stretched horizontally over the plot every 0.5 m. This installment served as distance reference on the plots for later image analysis (chapter 5.2). Below the plots a 4 m camera tower was installed, on top of which a Sony Alpha 7R II camera with a wide angle lens (Sony Vario-Tessar T FE 16-35 mm F4 ZA OSS) was mounted. The camera was fixed on a tilting angle to account for the average slope angle on the plots. The plot boundaries and the sand lines were illuminated at night with six eurolite 18W UV lamps, which emit light in the ultraviolet (UV) range at around 365 nm. Four lamps were mounted on metal rods, which were held over the plot by two people to illuminate the plot from above. The two remaining lamps were manually held and placed where more light was needed. The TAT 33 powder, coating the sand particles, provides an afterglow effect for several hours after being exposed to a light source (Noxton, 2019). To obtain this effect, the sand was exposed to two 23 W LED light panels prior to taking the photographs. This resulted in a higher overall visibility of the sand and no UV illumination would be needed to allow sand detection. However, the sand shines brighter with additional UV illumination and allows for an easier detection. Furthermore, the fluorescent chain and the ropes need constant UV illumination to be visible in the dark.

Photos of the sand lines were taken the nights before and after irrigation experiments, with full pixel resolution (42 megapixels). The camera was operated remotely using the android smart phone Samsung Galaxy S8+ and the "PlayMemories Mobile" app from Sony. However, the focal point had to be set on the camera itself. The aperture was fully open (F/4), while the ISO and the shutter speed were set according to the current light and wind conditions. With strong wind the camera tower was moving slightly which led to blurry photos, when high shutter speeds were chosen. Thus, it was reduced to 1 s and higher ISO values (up to 8000) were used instead. However, under windless conditions the shutter speed was set to two, five or ten seconds to reduce the ISO (1000 – 5000, depending on the light conditions) and obtain better quality pictures.

4.2.5 Surface runoff pathways

To assess the congruency between the patterns of sand transport and flowing water on the surface, a dye tracer (brilliant blue) was added on the right plot of the 1990s moraine. This provided qualitative information on the degree of correlation between surface sediment transport and hydrologic connectivity. It was applied during the mid and high intensity simulations at locations where surface runoff was recognizable by eye. The movement of the dye tracer was captured with the Sony Alpha 7R II camera, mounted on the camera tower. The camera recorded a video with a resolution of 3840 px × 2160 px (UHD) and 25 frames per second.

4.3 Site characteristics

4.3.1 Vegetation

The mapping of vegetation on the experimental plots was done using the extended Braun-Blanquet method (Dierschke, 1994). The number of plant species and their abundance (vegetation cover) were recorded by Konrad Greinwald in summer 2018. All vegetation data used here was provided by Konrad Greinwald.

4.3.2 Slope angle

The slope angles (or slope gradients) were measured directly in the field using an inclinometer (1° precision). The angles were measured on one side of the plot (6 m plot length) in 0.5 m steps, resulting in 13 measurements per plot. The measurements were averaged per plot.

4.3.3 Microtopography

There are several methods to determine the microtopography. The current state of the art method uses terrestrial laser scanners (TLS; see e.g. Barneveld *et al.*, 2013) because they provide the highest possible accuracy and precision (Thomsen *et al.*, 2015). However, TLS are not able to properly map through dense vegetation (Coveney and Stewart Fotheringham, 2011). Thus, other optical methods to measure microtopography (e.g. the creation of stereo photos or the use of an Xtion Pro, see Thomsen *et al.*, 2015) were not further considered, as they would face the same challenges. Due to patchy coverage of alpine roses (*Rhododendron ferrugineum*) and other shrubs on the moraines, roller chains (see e.g. Thomsen *et al.*, 2015) were also considered unsuitable.

Therefore, a self-constructed Microtopography Profiler (MTP; sometimes also called pinboard or micro profiler) was used (Figure 4.3a). The profiler was made by Fabian Maier, and was similar to the construction of Leatherman (1987). It consists of a wooden rectangular frame and 101 metal rods placed vertically through the frame. The distance between the rods is 1.5 cm (horizontal resolution), providing a horizontal length of 1.5 m. Behind the frame waterproof paper was mounted. On the paper, horizontal lines were drawn at a 1 cm distance in order to read off the height of the rods.

The MTP was set at ten locations on each plot (hereinafter called transects, lines i to x; see also Figure 4.3b). For all measurements, the MTP was placed fully vertical (0°) and the metal rods were set on the ground while avoiding branches or stems of shrubs and trees. The Sony Alpha 7R II camera was used to take photos of the final position of the rods. The camera was placed on a tripod in front of the MTP. The camera was always positioned in front of the center of the profiler. This was crucial as the metal rods did not directly touch the paper with the marks. By maintaining the same viewing angle for all images, a higher accuracy was reached (looking at the profiler from different angles would have led to different height estimates). Using the lines on the paper behind, the heights of the rods were read off manually from the photos with a 0.5 cm vertical resolution.

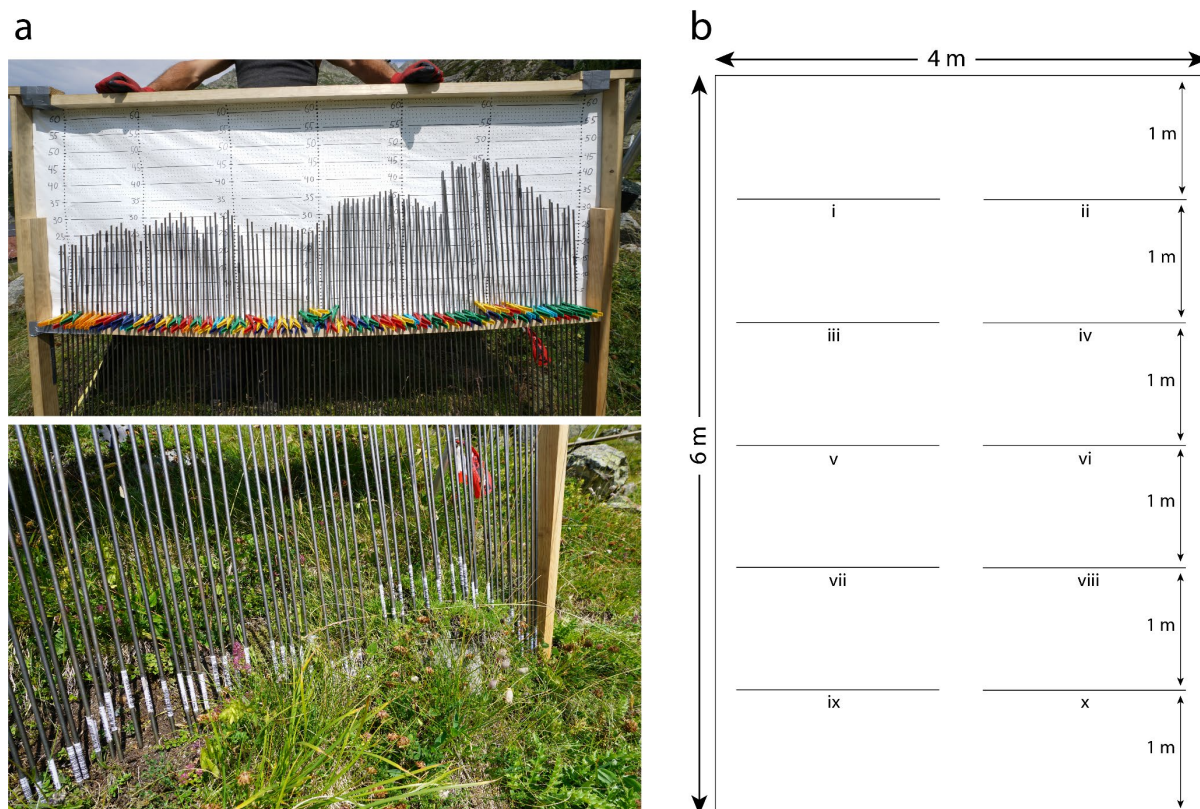


Figure 4.3 (a) Microtopography profiler (MTP) in the field (3k plot, transect v). (b) Sketch of an experimental plot with the theoretical dimensions of 4×6 m and the ten transects (horizontal lines i to x) for which the microtopography was determined.

4.3.4 Saturated hydraulic conductivity

The saturated hydraulic conductivity (K_{sat}) at the surface is the steady state surface infiltration rate (assumed to represent saturated conditions). It was measured using double ring infiltrometers (Eijkelkamp). The lower end of the infiltrometers was cut at an 20 – 30° angle (which represents the average slope for all moraines of the Steingletscher) for easy use on steep hillslopes. The use of double ring infiltrometers for sloped landscapes was already tested and declared suitable by Bodhinayake *et al.* (2004).

At each experimental plot, three measurements were taken. The measurements were conducted close to the borders but outside the experimental plots to not influence the plots. The three measurements (upper part, middle part, lower part) were averaged (arithmetic mean) for the purpose of this thesis. The hydraulic conductivity data for this thesis was provided by Fabian Maier.

5 Data analysis

5.1 Surface topography

5.1.1 Microtopography

For each transect, the minimum height was subtracted from all values so that the minimum elevation was always zero and the different transects could be compared. To assess surface roughness, two measures were used: Random Roughness (RR) and the Tortuosity Index (TI). For the analyses, both measures were averaged per plot (average of the ten transects). Random roughness is one of the most used indices to describe surface roughness in the literature (Paz-Ferreiro *et al.*, 2008). Here, the random roughness definition of Currence and Lovely (1970) was used (see also Vermang *et al.*, 2013):

$$RR = \sqrt{\frac{1}{n} \sum_{i=1}^n (h_i - \bar{h})^2} \quad (2)$$

where h a single height reading, \bar{h} the mean of the height readings per transect and n is the total number of height readings per transect (here 101). In other words, it is the standard deviation of the height readings h .

For the tortuosity index, the profile lengths of each transect had to be calculated. To do so, the coordinates of the height readings were digitally connected to form a line. This line approximates the length of a corresponding line directly measured on the ground, e.g. by a roller chain. The rougher a surface, the longer the length of this line. The tortuosity index generally allows an easier comparison of line lengths in different studies since it is independent of the profiler. It is defined as:

$$TI = \frac{L - L_0}{L_0} \quad (3)$$

where L is the length of the line of the considered transect and L_0 the horizontal length of the profiler (Bertuzzi *et al.*, 1990), here 1.5 m.

For the comparison of the microtopography with the sand and dye movement on the 1990s right plot, a 3-dimensional plot was created using only the transects within the area of the sand transport (transects v to x on the lower part of the plot, see also Figure 4.3b). The transects next to each other (v and vi, vii and viii, ix and x) were combined, leading to three microtopography lines over nearly the whole plot width with a 30 cm gap in between and 35 cm missing on either

side of the lines towards the plot boundaries. Using the measured slope angles (0.5 m intervals – see chapter 4.3.2) the actual elevations of the microtopography transects (relative to the lowest microtopography line) could be determined and plotted (see Appendix 1).

5.1.2 Flow directions

Additionally, a DTM of all three moraines was created, using areal drone images (camera: Sony Cyber-shot DSC-WX220) from summer 2017 to calculate potential flow directions for surface runoff (DTM based flow accumulation). The drone flights and the post processing of the images were done by WWL Umweltplanung und Geoinformatik GbR. DTMs allow the determination of potential surface hydrological connectivity based on water routing and accumulation on the surface (see e.g. Golden *et al.*, 2017). The flow directions and the water accumulation were generated by Fabian Maier using the $D-\infty$ method of Tarboton (1997), which allows for flow into all directions (independent of the grid cells/pixels). Generally, DTM based flows are used at meso and macro scales. However, the drone images had a very good spatial resolution and, thus, the DTM based flows were qualitatively used at plot scale. The DTM based flow directions were compared to the patterns of the sand transport.

For the 1990s right plot the patterns of the sand transport, the dye tracer and the DTM based flow directions were qualitatively compared with the data from the microtopography profiles (chapter 5.1.1). On the other plots the patterns of the sand transport were compared with the DTM flow directions.

5.2 Fluorescent sand transport

The photos of the fluorescent sand were processed using Python 3 (v3.7 – used with Spyder v3.3.1), Adobe Photoshop CC 2019 and the statistical computing software R (v3.5.1 – used with RStudio v1.1.463). First, a geometric correction was applied in order to account for slightly different camera angles in the different pictures and to convert the pixels (px) into a distance measure (here millimeters). Therefore, the Interactive Data Language (IDL) code for the geometric correction of brilliant blue dye tracer pictures (developed by Weiler, 2001; but see also Weiler and Flühler, 2004; Schneider *et al.*, 2014), was converted by Hannes Leistert (University of Freiburg, Chair of Hydrology) to Python 2 and further to Python 3 by Marc Vis (University of Zurich, Department of Geography).

Within the interactive Python 3 script the reference points of the segmented plastic chain around the experimental plots were marked and their corresponding coordinates added. The top

left corner of the chain grid was set as $x = 0$ mm and $y = 0$ mm. The second point, 0.5 m further down, where the color of the chain changes for the first time, the coordinate were $x = 0$ mm and $y = 500$ mm. This procedure was performed counter clockwise for each available reference point on both sides of the plot. Reference points were not selected on the slope parallel lines (top and bottom) because the chain was not completely straight. The horizontal distances used, in order to get the right x-values on the right side of the plot, were measured in the field. Using the selected points and their coordinates, the photos were geometrically corrected, resulting in new pictures, where one pixel corresponds to one millimeter (1 px = 1 mm).

The algorithm for the geometric correction is restricted to interpolation and not applicable for extrapolation outside the reference points. Therefore, only the area within the selected reference points was geometrically corrected. If sand moved below the last reference point on the photo, a correction would not be possible. Such cases existed, because in the field the focus was on taking images that captured all sand particles. They thus did not necessarily contain all reference points. For these pictures (1990s left and right plots for the mid and high intensity event), the reference grid was linearly extrapolated outside of the photo (before the geometric correction) using Adobe Illustrator CC 2019 and the segmented chain was prolonged using straight lines (Figure 5.1). This was also done for the slope parallel ropes. The intersections of the extended lines were used as the extrapolated reference points. After extrapolation, these photos were geometrically corrected, using the Python 3 script.

The geometrically corrected pictures were exported and cropped in Adobe Photoshop (cropping in Python is also possible but is less precise) so that they corresponded to the dimensions of the grid inside the fluorescent chain on the experimental plots. This means the pixel row and column containing the coordinate (0, 0) became the first row and column of the cropped photo.

The corrected and cropped photos were further processed in a new Python 3 code, developed for this thesis. However, some parts were similar to the code used for the extraction of brilliant blue dye (Weiler, 2001; Weiler and Flühler, 2004; Schneider *et al.*, 2014). In a first step the photos were converted from the rgb (r = red, g = green, b = blue) to the hsv (h = hue, s = saturation, v = value) color space. The hsv color space (Figure 5.2) was defined by Smith (1978) and is a transformation of the rgb space. Hue (h) represents the color on a circle in degrees (from 0° to 360°). Saturation (s) is a relative measure of the color purity or vibrance and ranges from 0 – 100 %. In other words, it is the deviation of the color from white. The value (v) is a measure of the brightness, which also ranges from 0 – 100 % and is, thus, the deviation from black (Smith, 1978; Li, 2008). The use of the hsv color space has the advantage that only one measure (namely hue) describes the color, given that the saturation and value were constant.

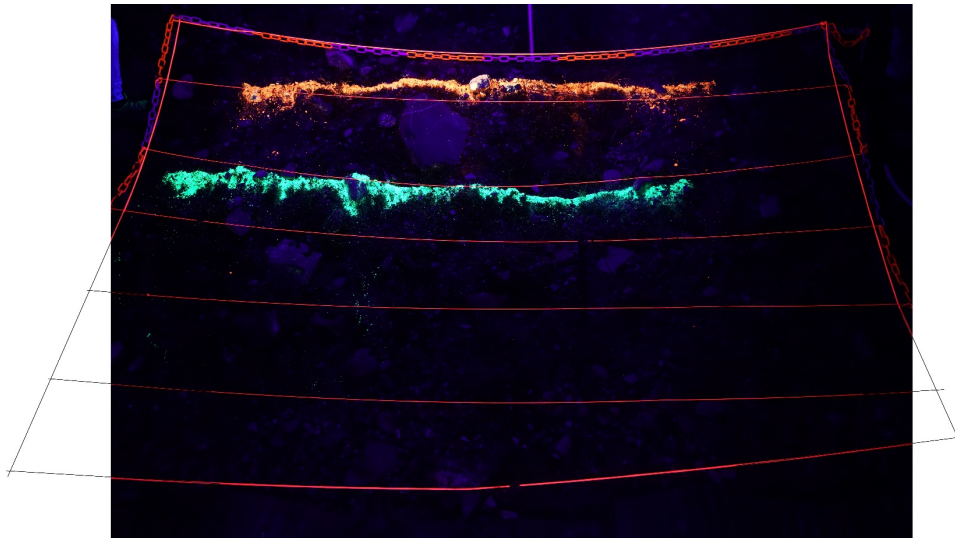


Figure 5.1 Linear digital extension of the reference grid outside the photo in order to perform the geometric correction for the photo of the 1990s left plot after the mid intensity rainfall simulation.

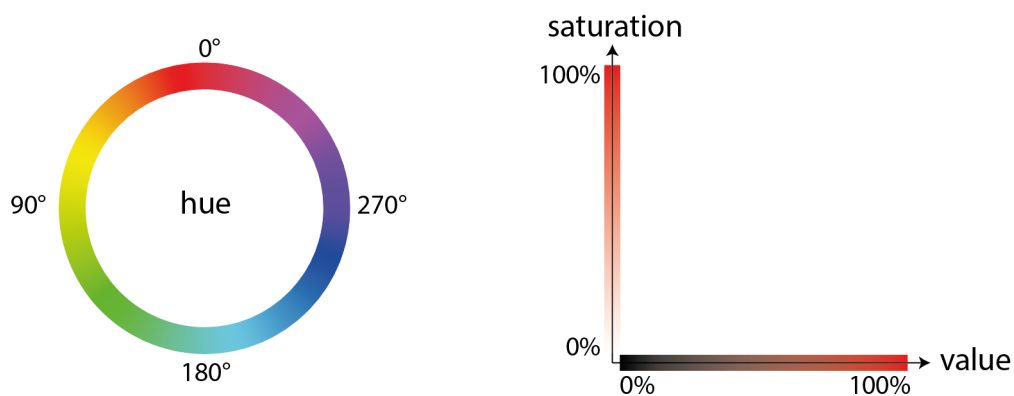


Figure 5.2 Visualization of the three dimensions (hue, saturation, value) of the hsv color space. Hue is represented on a circle in degrees. Saturation and value are relative measures and range between 0 % and 100 %. This figure was modified from Rahmat et al. (2016).

An analysis based on the hue histogram in Python for the sand extraction proved to be not possible because distinct color specific peaks could not be determined. Thus, ten representative spots on the photos were chosen per sand color using the “Color Sampler Tool” in Adobe Photoshop to determine the typical hue values. The hue of the orange sand varied between 0° and 80° and between 320° and 360° . The green sand had a hue between 150° and 180° , while the blue sand had a hue between 180° and 240° (the borders were always excluded from the range in order to prevent overlaps). The boundaries were the same on all photos. Not all sand particles recognized by human eyes were detected within this range. As the quartz sand particles and TAT 33 were not perfectly bond together, some sand particles lost their ability to glow when the TAT 33 coat was

washed off. The remaining quartz sand had a more whitish color. To ensure correct maximum sand transport distances (see below), the lowermost pixel containing sand was manually checked for its hue. In case of a hue outside the typical boundaries for the corresponding color, the pixel was recolored with a hue within the range using Adobe Photoshop.

In order to extract the sand of one color from the photos, the hue of each individual pixel was checked in Python. If a pixel had its hue within the given range for a color and the value v was larger than 10 %, it was classified as '*sand*' and otherwise as '*no sand*' (Figure 5.3a). The threshold of the value was chosen in order to reduce noise for the dark parts of the photos (glowing sand was brighter and had, thus, higher values). This procedure worked well for the extraction of the green sand but proved to be more difficult for the orange sand as also the grid around the plot and the fluorescent rope on the plot emitted light within the observed range of the orange sand. Using Adobe Photoshop these lines were manually "removed" using black color. This method is subjective, but no appropriate other method could be found. During the extraction of the blue sand, the surrounding parts of the green sand (some sand particles but mainly the glowing light around the green sand line) were detected as blue sand because the emitted light of the green and blue sand were very close together. Based on visual classification, the break point between green and blue was set to 180° (below: green, above: blue). To minimize misclassifications the images were cropped so that most of the green sand (green line) was not on the picture. The remaining number of green sand particles (those that moved during the mid intensity rainfall simulation below the blue sand line) which were misclassified to blue are based on visual comparison assumed to be negligible.

In the classified images of all three sand colors, the number of classified pixels were counted per row (row sums). The sums can be shown as density curve along the plot border (Figure 5.3b). The row sums were exported to the statistical computing software R, where the pixel row with the maximum number of classified pixels (row with maximal row sum) was determined. This corresponds to the peak (approximately the middle) of the sand line (see red line in Figure 5.3). All the rows above were removed so that the peak of the sand line was set as starting point for the sand movement. The number of the pixel row (counted from the top), thus, corresponds to the distance (in mm) of the sand movement from the peak of the sand line.

By comparing the pictures before and after an irrigation experiment, the sand particles that moved during the experiment were extracted. The number of the classified pixels per row prior to the experiment were subtracted from that after the experiment. Negative numbers, e.g. at the sand line due to sand infiltration and movement, were set to zero. The resulting datasets provided information on the amount of sand (number of pixels or mm^2) that moved during the rainfall simulations, starting at the peak of the sand line.

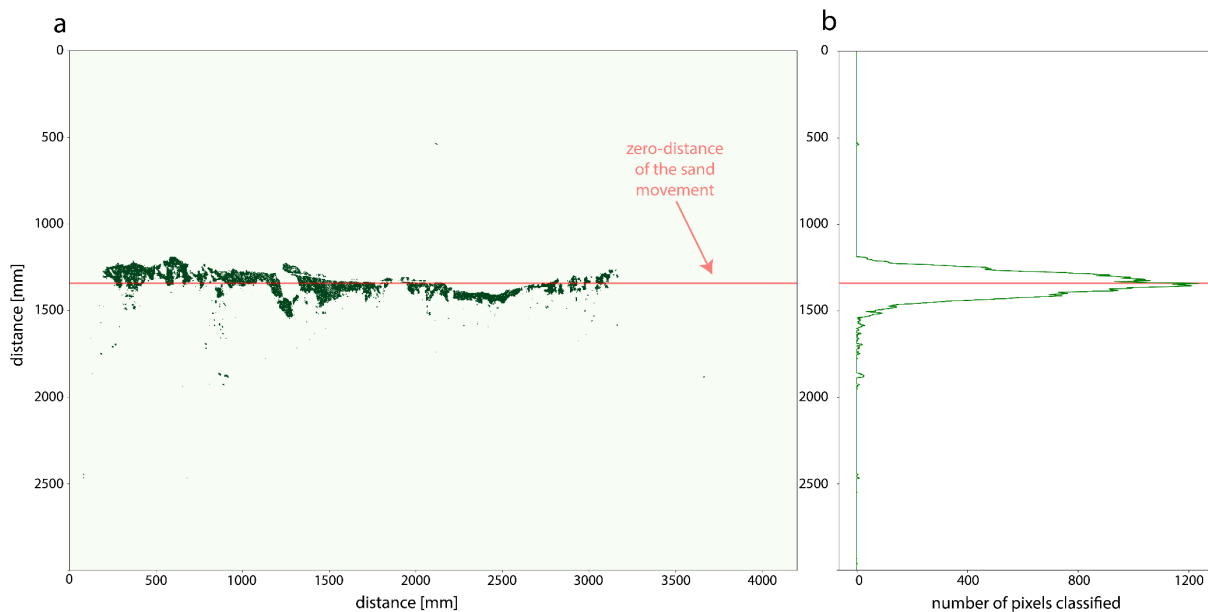


Figure 5.3 (a) Image of the extracted green sand (mid intensity) on the 1990s left plot. The distances are the same as on the photo before the extraction; the coordinate $(0, 0)$ is located at the top left corner. One pixel corresponds to 1 mm^2 . Per pixel row the number of classified pixels was counted and plotted as density curve (b). The sand line and the particles below the line can clearly be identified. The red line marks the peak (middle) of the sand line and represents the averaged 'zero-distance' of the sand movement.

Because the maximum travel distance of the sand is somewhat uncertain, four distance measures to describe the sand movement were extracted: the 50 %, 75 %, 90 % and 100 % (maximum) distance of the sand that moved over the surface. For this, the cumulative frequency distribution of the travel distances of all particles that moved was determined. The 50 % marks the median travel distance of the particles that moved and 100 % the maximum travel distance of a sand particle that moved but stayed on the plot. The maximum distance (100 %) could also be extracted based on the number of the last pixel row containing sand, since one pixel equals 1 mm and the peak of the sand line was pixel row zero.

5.3 Sand and blue dye

Surface connectivity was inferred from the fluorescent sand tracer transport. The distribution of the fluorescent sand particles (orange, green, blue) after all three irrigation experiments (low, mid, high), revealed preferential surface flow patterns. Thus, lines around the distribution of all sand particles were drawn by hand in Adobe Photoshop CC 2019 for a qualitative representation of the surface connectivity. In addition, a composite image over the time of the blue dye tracer movement was created using Adobe Premiere Pro CC 2019 and Adobe Photoshop CC 2019 for the right plot of the 1990s moraine. The flow path outlines of the dye tracer and the shape outlines of

the fluorescent sand were combined in one composite image in order to qualitatively compare the patterns.

5.4 Correlation analysis and PCA

The distance measures for sediment transport (50 %, 75 %, 90 % and maximum distance) were expected to depend on the site characteristics (vegetation cover, number of plant species, slope angle, surface roughness and saturated hydraulic conductivity). Therefore, the correlation (Pearson linear correlation (r) and Spearman's rank correlation (r_s)) between the sand travel distances and the site characteristics, as well as the surface runoff ratio and sediment load was determined. Because many of the site characteristics were correlated (and thus not independent), a Principal Component Analysis (PCA) was performed and the two first principal components were used in the correlation analysis as well.

6 Results

6.1 Site characteristics

6.1.1 Vegetation

The vegetation cover ranged from 21.2 % (1990 left) to 55.1 % (1860 left) and was clearly higher for the plots on the 3k and 1860s moraine than for the 1990s moraine plots (Table 3). The number of plant species was also higher for the plots on the 3k and the 1860s moraine and ranged from 24 (1990 left) to 46 (3k). However, the number of species on the 1990 middle plot (34) was very similar to the 1860s left and right plots (35 each).

6.1.2 Slope angle

The average slope angle on the experimental plots ranged from 21.8° (1990 right) to 36.6° (1860 left), indicating different conditions for the plots (Table 3 and Figure 6.1a). The Kruskal-Wallis test revealed that the experimental plots were statistically not identical (p-value of $9.8 * 10^{-6}$, Figure 6.1a). The 1860 left and 1990 left plots had similar mean slope angles, and so did the other four plots. The Dunn's test further indicated that the 3k and the 1990 left plots were not significantly different either.

The standard deviations of the slope angles were similar among the plots (ranging from 5.0° on the 1990s middle plot to 8.4° on the 1990s right plot) except for the 3k, where it was significantly higher (14.2°; see also Table 3). This indicates a strongly changing terrain. Indeed, the plot had more steps and depressions than the other plots (see also Figure 3.2).

Table 3 Site characteristics of all six experimental plots: the estimated values of the vegetation cover (in %), the number of plant species, the averages of the slope angle and their standard deviations sd (in degrees), the tortuosity index TI, the random roughness RR (in cm) and the saturated hydraulic conductivity K_{sat} (in mm/h).

plot	vegetation cover [%]	number of plant species	slope angle [°]	slope sd [°]	tortuosity index TI	random roughness RR [cm]	K_{sat} [mm/h]
3k	52.5	46	25.4	14.2	0.334	5.4	600
1860 left	55.3	35	36.6	5.6	0.285	4.1	1720
1860 right	52.9	35	24.5	5.2	0.292	3.8	2660
1990 left	21.2	24	33.0	6.1	0.358	3.9	5760
1990 middle	38.5	34	23.8	5.0	0.550	5.2	3720
1990 right	34.5	29	21.8	8.4	0.524	6.6	3480

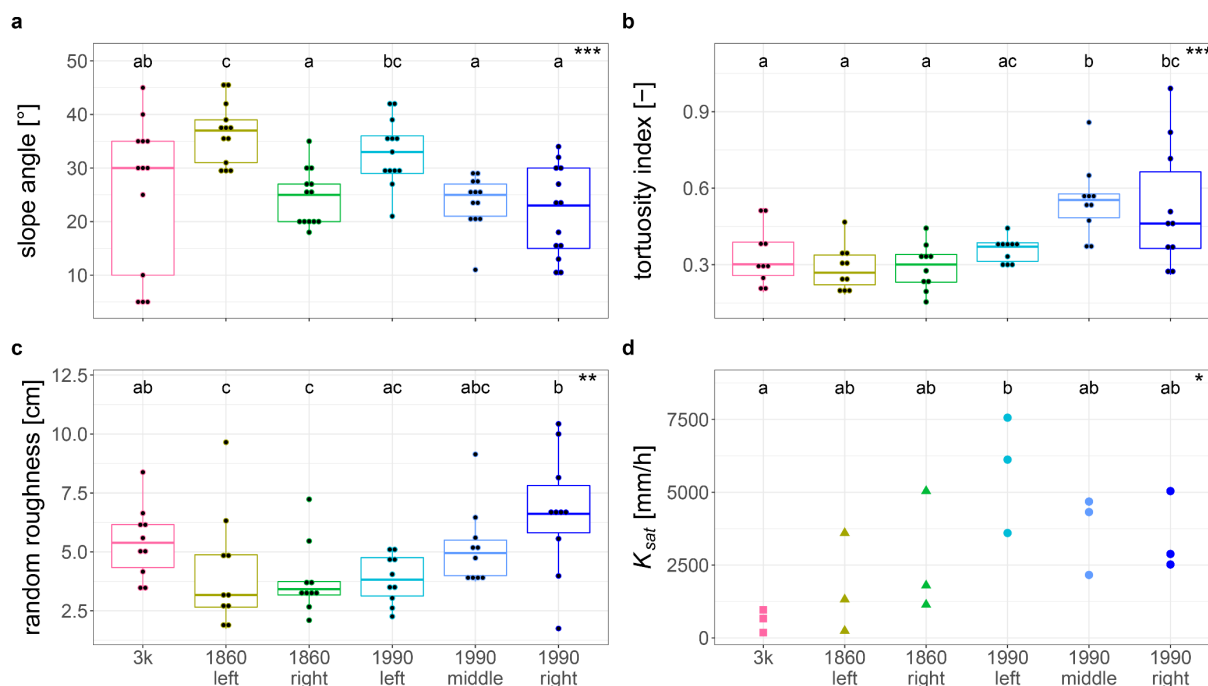


Figure 6.1 Boxplots of (a) the slope angle in degree, (b) the tortuosity index (TI), and (c) the random roughness (RR) in mm as well as (d) a scatter plot of the saturated hydraulic conductivity K_{sat} in mm/h for all six experimental plots. The stars indicate the significance level of the Kruskal-Wallis test for slope angle and random roughness and of the ANOVA for tortuosity index and K_{sat} (** $p < 0.001$, ** $p < 0.01$, * $p < 0.05$). Different letters indicate significant different mean values based on the post-hoc test (significance level: $\alpha = 0.05$).

6.1.3 Surface roughness

Both surface roughness measures indicated differences in microtopography among the experimental plots (Figure 6.1b, Figure 6.1c and Table 3). Overall the one-way analysis of variance (ANOVA) revealed a strongly significant difference between the plots with a p-value of 1.9×10^{-5} . The tortuosity index for the two plots on the 1990s moraine (middle and right) was different than that for the other plots. The 1990 left plot had a tortuosity index that was somewhat in between the others. The random roughness was higher for the 1990s middle and left plots, as well as for the 3k plot but the differences were less clear. The data points were more variable per plot, leading to a large overlap between the plots. Nevertheless, the p-value of 3.9×10^{-3} for the Kruskal-Wallis test indicates a significant difference between the plots in terms of surface roughness.

6.1.4 Saturated hydraulic conductivity

The mean of the saturated hydraulic conductivity was higher for the three plots on the 1990s moraine than for the others (Table 3 and Figure 6.1d). It was clearly the lowest (600 mm/h) for the 3k plot and highest for the 1990s left plot (5760 mm/h). The ANOVA revealed a significant

difference among the plots with a p-value of 0.0278. However, according to the Tukey HSD test only the 3k and 1990s left plots were significantly different from each other.

6.2 Surface runoff and sediment load

For the low intensity simulation, surface runoff was only observed on the middle and right plots of the 1990s moraine (Table 4). For the mid intensity simulation, surface runoff occurred also on the 1860s right plot. For the high intensity simulation, surface runoff occurred on all plots. Surface runoff and thus also the surface runoff ratio (r_{sf}) were higher for the younger moraines ($3k < 1860 < 1990$). For the high intensity simulation, the surface runoff ratio ranged between 4 % (3k) and 8.4 % (1990 right).

The sediment load of the surface runoff did not indicate the same clear trend from young to old as the surface runoff ratio. The sediment loads ranged from 41 g (3k) to 933 g (1990 right) for the high intensity simulation.

The surface runoff ratio and the sediment load for the 1990s right plot are slightly underestimated because of a lack of measurements after the experiment stopped.

6.3 Sediment transport

The cumulative distribution of the distances of the sand transport varied between all experimental plots and rainfall intensities (Figure 6.2). The sand on the 1860s left plot barely moved and only a few sand particles were detected below the original sand line (leading to the steep curves in Figure 6.2b; see also photos in Appendix 3). On the other five plots, more sand particles moved and covered a larger area (less steep curves in Figure 6.2a and c-f). On the 1990s right plot the sand was more uniform spread with distance below the original sand line (compared to the other plots). The sand on the 1990s left and right plots appears to have moved further for the mid intensity than for the high intensity rainfall simulation.

The sand moved (maximal distances) between 0 mm (1860 left) and 1320 mm (1990 right) for the low intensity, between 400 mm (1860 left) and 1280 mm (1990 right) for the mid intensity and between 440 mm (1860 left) and 890 mm (1990 right) for the high intensity rainfall simulation (Table 5).

Table 4 Surface runoff ratios (in %) and sediment loads (in gram) for all six experimental plots and all three simulated rainfall intensities (low, mid, high). The values for the high intensity event on the 1990 right plot (marked with a *) are an underestimate because the sediment load and flow after the experiment are not known due to a broken fire hose.

plot	low intensity surface runoff ratio [%]	mid intensity surface runoff ratio [%]	high intensity surface runoff ratio [%]	low intensity sediment load [g]	mid intensity sediment load [g]	high intensity sediment load [g]
3k	0	0	4	0	0	41
1860 left	0	0	4.4	0	0	69
1860 right	0	5.2	4.1	0	155	224
1990 left	0	0	4.9	0	0	87
1990 middle	7.9	6.3	6.8	24	133	320
1990 right	9.3	12.1	8.4*	21	533	933*

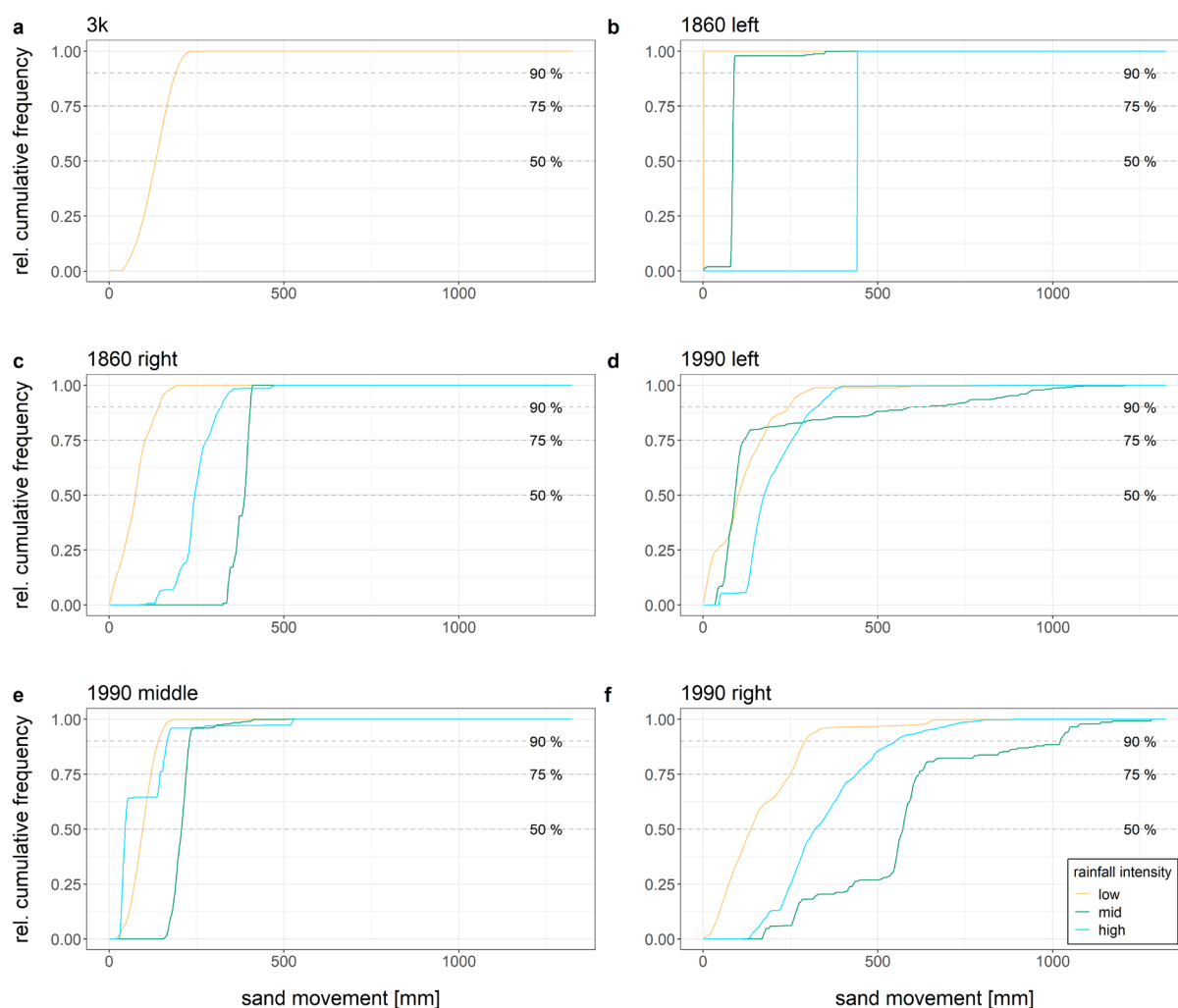


Figure 6.2 Relative cumulative frequency curves for the fluorescent sand that moved for all three rainfall intensities (low = orange, mid = green, high = blue) on (a) the 3k plot, (b) the 1860s left plot, (c) the 1860s right plot, (d) the 1990s left plot, (e) the 1990s middle plot and (f) the 1990s right plot. On the 3k plot only one sand line (for the low intensity simulation) was applied. The horizontal lines for the extracted cumulative sand distances are marked and labeled (50 %, 75 %, 90 %).

The 50 % and 75 % relative cumulative frequencies of transport distances on the 1860s right, the 1990s middle and right plots increased from the low to the mid intensity simulations, but appear to have decreased again for the high intensity simulation (Table 5, Figure 6.3). Only for the 1860s left plot did the travel distances increase with increasing rainfall intensity. The distances for the 1990s left plot decreased from the low to mid intensity but increased for the high intensity event. The 90 % of the relative cumulative frequency of the transport distance increased from the low to the mid intensity simulation for all plots, however for the high intensity it decreased again for all plots, except for the 1860s left. The maximum sand transport distances increased for all plots from the low to the mid intensity simulation except for the 1990s right plot, where it decreased slightly. For the high intensity simulation, the maximum distance of the 1860s left and right and 1990s middle plots increased further compared to the mid intensity. On the 1990s left and right plots the maximum distances were shorter for the high intensity than for the mid intensity simulation. For the 1990s left and right plots it strongly decreased.

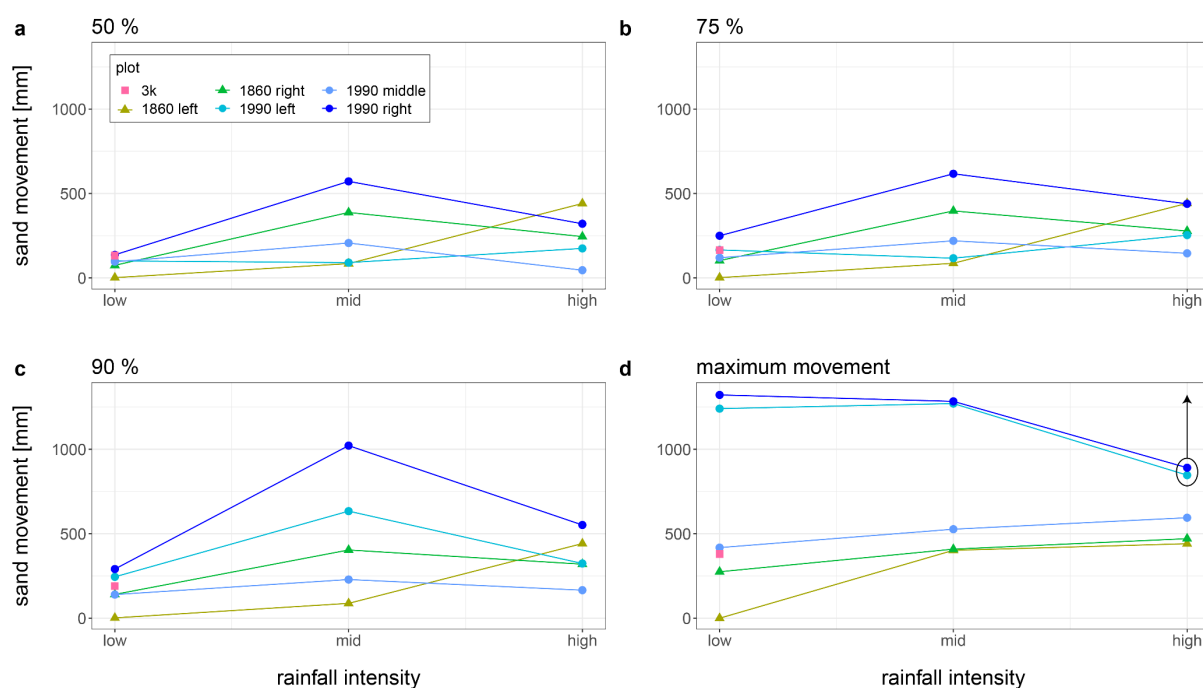


Figure 6.3 The (a) 50 %, (b) 75 %, (c) 90 %, and (d) 100 % (maximum sand movement) of the cumulative frequency of the transport distances for all sand particles that moved as a function of the simulated rainfall intensity (low, mid, high). On the 3k plot only one sand line (for the low intensity simulation) was applied. On the 1990s moraines left and right plots sand moved below the lower plot boundary for the high intensity event and their maximum movement values were too small (indicated with the arrow).

Table 5 Distances of the sand movement (based on the 50 %, 75 % and 90 % relative cumulative travel distances for the particles that moved, as well as the maximum sand movement, 100 %) in mm for all six experimental plots and all three simulated rainfall intensities (low, mid, high). The values were rounded to 10 mm intervals. No data is indicated by n/a.

plot	distance of the sand movement			maximum sand movement [mm]
	50 % [mm]	70 % [mm]	90 % [mm]	
Low intensity				
3k	130	170	190	380
1860 left	0	0	0	0
1860 right	80	100	140	280
1990 left	100	170	250	1240
1990 middle	100	120	140	420
1990 right	140	250	290	1320
Mid intensity				
3k	n/a	n/a	n/a	n/a
1860 left	90	90	90	400
1860 right	390	400	400	410
1990 left	90	120	630	1270
1990 middle	210	220	230	530
1990 right	570	620	1020	1280
High intensity				
3k	n/a	n/a	n/a	n/a
1860 left	440	440	440	440
1860 right	250	280	320	470
1990 left	180	250	320	850
1990 middle	50	150	170	600
1990 right	320	440	550	890

However, fluorescent sand particles were found in the gutters below the 1990s left and right plots. Hence, the corresponding values for maximum sand transport distances are larger (indicated with the arrow in Figure 6.3d). Nevertheless, the values were assumed to be in the correct ordering (higher than the other three), and thus they were still used for the correlation analysis (chapter 6.5).

6.4 Surface connectivity

Less sand moved and the maximum distances were shorter for the plots with denser vegetation (3k, 1860 left, 1860 right; see also Figure 6.3d). The observed qualitative maximum sand extent was clearly smaller as well (Figure 6.4). On the 1990s left and right plots sand moved below the lower plot boundary and the full extent of the connectivity could not be assessed. On the three plots of the 1990s moraine and the 1860s right plot, areas of the different sand colors overlapped, indicating similar flow paths. On the 1860s left plot the areas with sand did not overlap but the distribution of the blue sand seemed to be an extension of the green area. There were two locations in the middle of the green sand line, where the sand moved downslope. Just below, in the blue sand also moved downslope (peaks in the middle of the lines, indicated with the red ellipse in Figure 6.4).

The dye tracer was applied on the surface at three locations on the 1990s right plot (blue shape outline in Figure 6.5a and c). At the first location it moved through a rill towards the left plot boundary. The dye tracer injected at the second location flowed around rocks, split its path multiple times and overall turned slightly to the left (seen from the camera tower; the actual flow direction is to the right – in the following directions are always presented from the camera tower view). In the lower part of the plot, where the terrain was flatter, the dye distributed over a larger area and ponding was observed. The third location, where dye was applied, was in the flatter area and surface water was mainly observed in ponds. Water moved only very slowly compared to the other locations. Surface flow was also observed in another location where no tracer dye was added (represented by a black dashed line in Figure 6.5a and c). The overland flow pattern agreed well with the sediment that was deposited just below the area and was also observed during a natural rainfall event.

The comparison of the dye tracer observations with the distribution of the sand on the 1990s right plot (Figure 6.5b) revealed similar flow paths for both (indicated in Figure 6.5c with red arrows). At the first location where dye was applied orange sand also moved along the rill. At the second location the sand (orange, green and blue) covered most of the dye pattern and ended up in the same paths. At the third location the sand only entered the dye area and, thus, no further overlap was visible. At the area where surface runoff was observed but no tracer dye was added (black dashed line in Figure 6.5a and c) green and blue sand moved downslope, leading to a good overlap.

The DTM based flow accumulation (Figure 6.6) indicated local downward flow within small channels for all plots except for the 3k, where no DTM based flow was accumulated on the plot surface (only below). According to the DTM there was little flow accumulation where the sand lines were placed on the 1860s left and right plots. However, there was some overlap, e.g. on the right plot on the right side of the sand lines. On the 1990s moraine the traces of the sand overlapped with the DTM based flow accumulation. On the left plot, the sand movement overlapped well with DTM based flow accumulation (see e.g. on the left side). On the middle plot, on the left side of the sand lines, sand barely moved. However, on the right side where the DTM based flow accumulation indicated a stream (dark blue) there was more sand movement. On the right plot, the DTM based flow accumulation matched with the sand movement and also the three locations where dye was added (1, 2, 3 in Figure 6.5) and where surface flow was observed (black dashed line Figure 6.5).

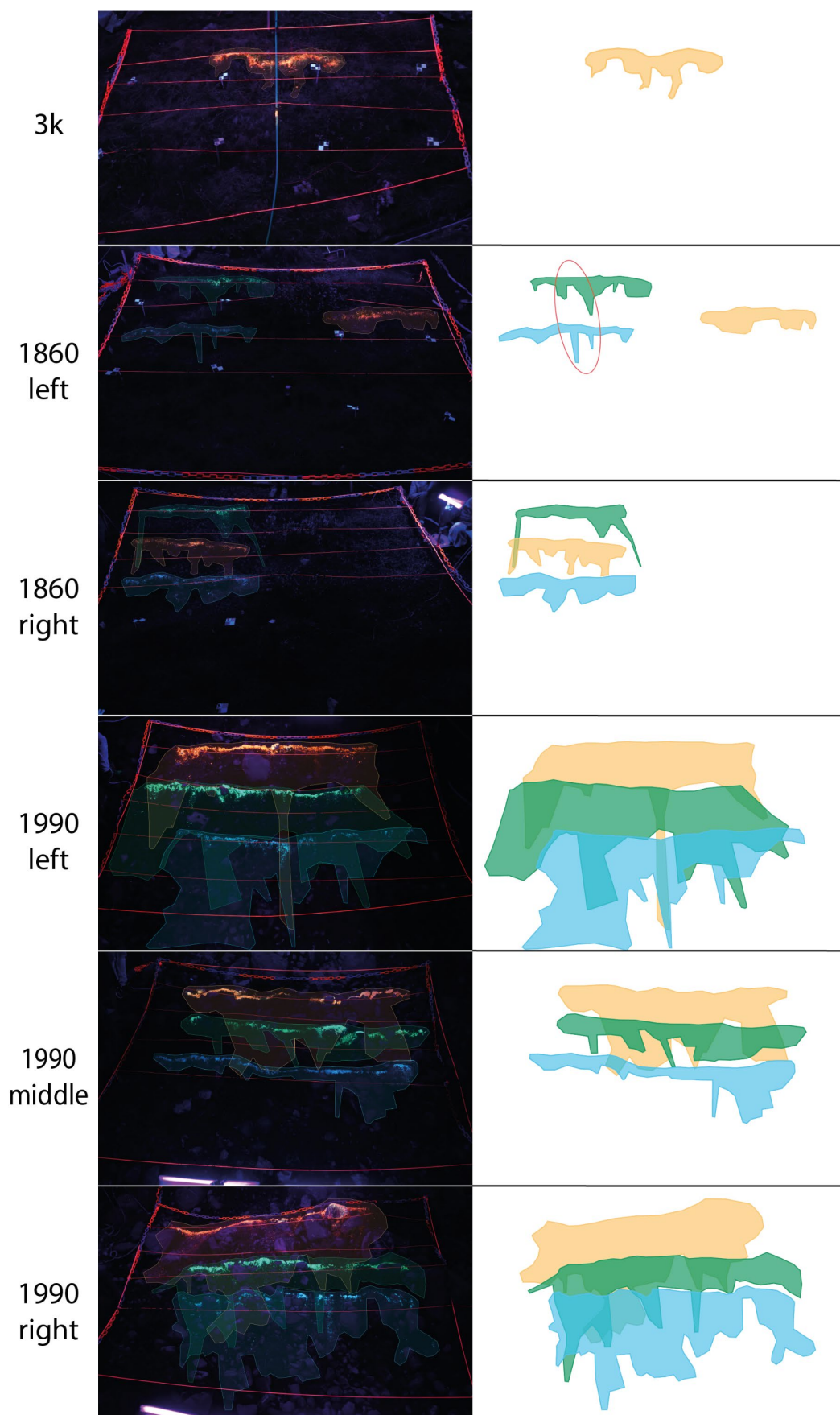


Figure 6.4 Photos of the fluorescent sand lines after all three rainfall simulations of the 3k, 1860 left, 1860 right, 1990 left, 1990 middle and 1990 right plots. Outlines (in the corresponding color) were drawn around the maximum sand extent and are also presented on the right without the photo. The red ellipse indicates a possible flow path (see text).

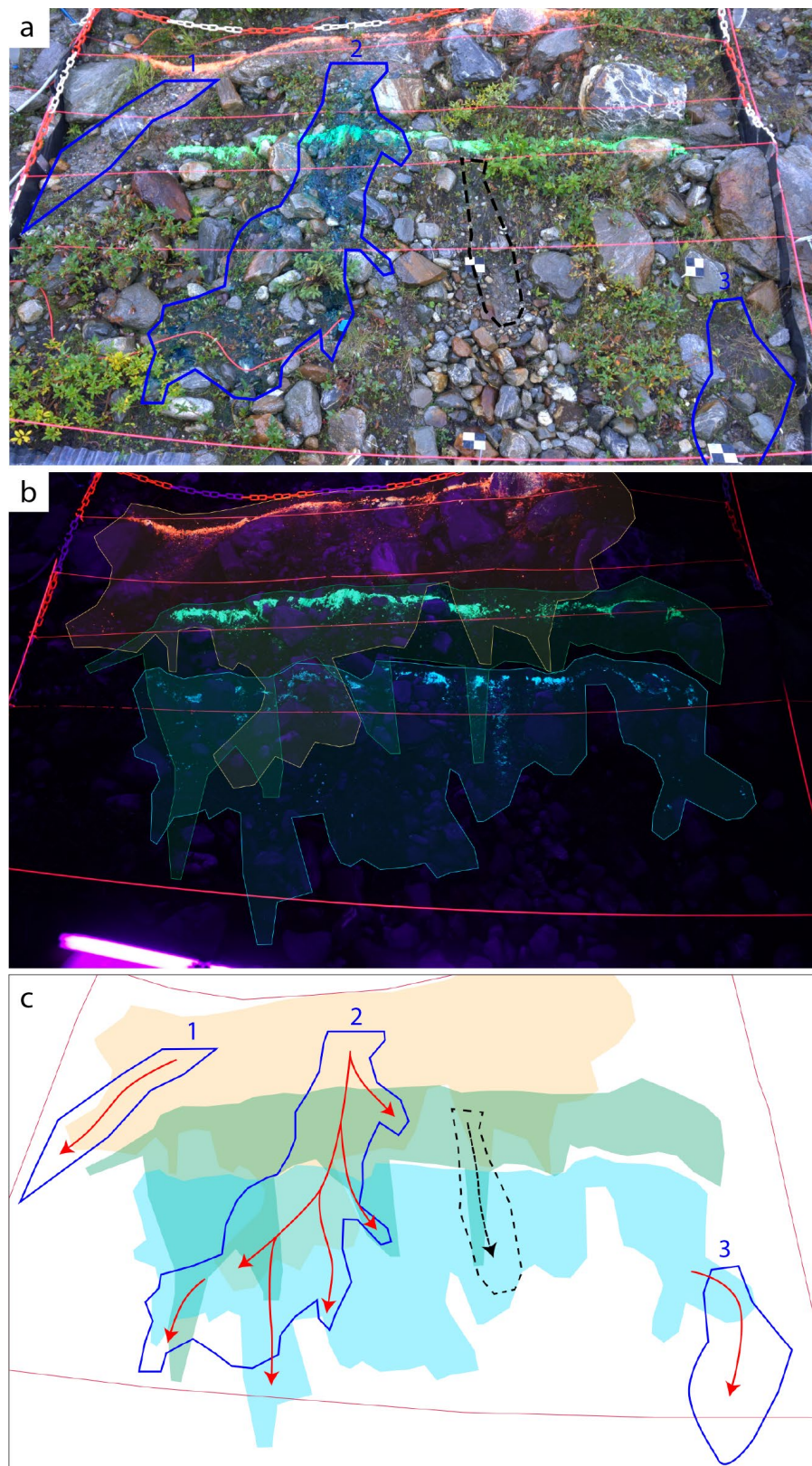


Figure 6.5 (a) Areas of observed surface runoff on the 1990s right plot. In blue (1, 2, 3), areas where the brilliant blue dye tracer was added. The black dashed line indicates an area where surface runoff was observed but no tracer dye was added. (b) The distribution of the sand after all three rainfall experiments and the outline (in the corresponding color) on the same plot is shown (see also Figure 6.4). (c) Combination of the shapes from the observed surface runoff (a) and the fluorescent sand (b). The arrows indicate where the flow directions of water and sediment overlapped.

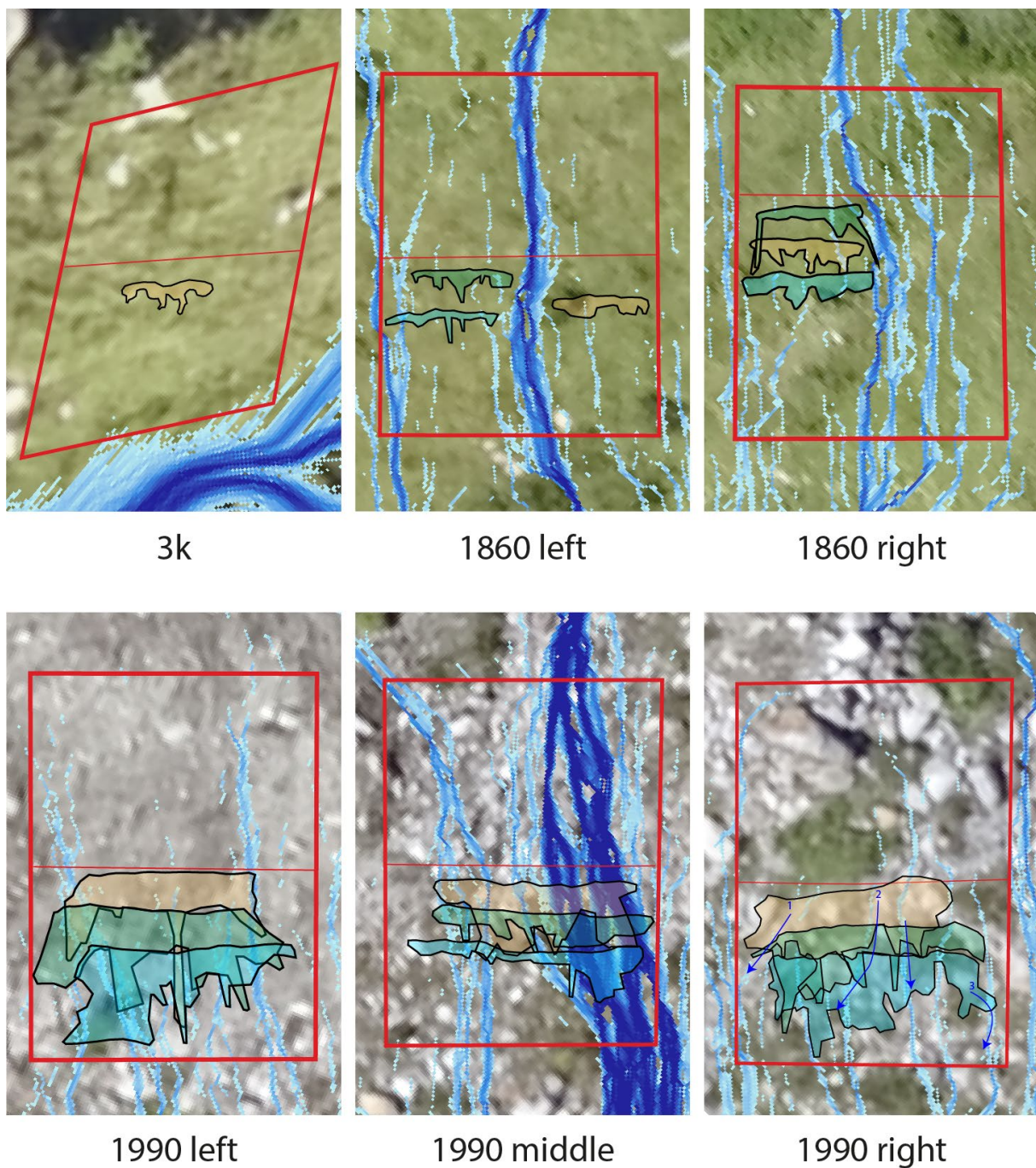


Figure 6.6 Areal drone images and Digital Terrain Model (DTM) based flow accumulation of all six experimental plots. The flow accumulation calculated based on the DTM and the $D-\infty$ method is shown in blue (darker blue represents more flow accumulation). The thick red lines represent the plot borders, the thin red lines the area of the fluorescent sand setup. The colored shapes with black outlines indicate the sand covered areas after all three rainfall intensities (separated by the sand color; similar to Figure 6.4). The blue arrows on the 1990s right plot indicate the observed flow paths of surface flow (as shown in Figure 6.5c).

The 3-dimensional representation of the microtopography on the 1990s right plot (Figure 6.7) indicates a good match with the flow patterns of the dye tracer (black straight lines) and surface flow (black dashed line). This indicates that overland flow and sediment transport occurred in rills. On the left side of the plot an approximately 20 cm high “peak” (next to the green arrow) represents a rock located in a topographic depression (also visible in Figure 6.5a). The surface water, the dye tracer and also the sand particles passed this rock on the left side (green arrow). On the lower left side of the plot, the microtopography indicates a topographic slope towards the left. This was coherent with the flow paths (shown in Figure 6.5). The observed surface flow with no dye addition also occurred in a small depression or rill (see also Figure 6.5a).

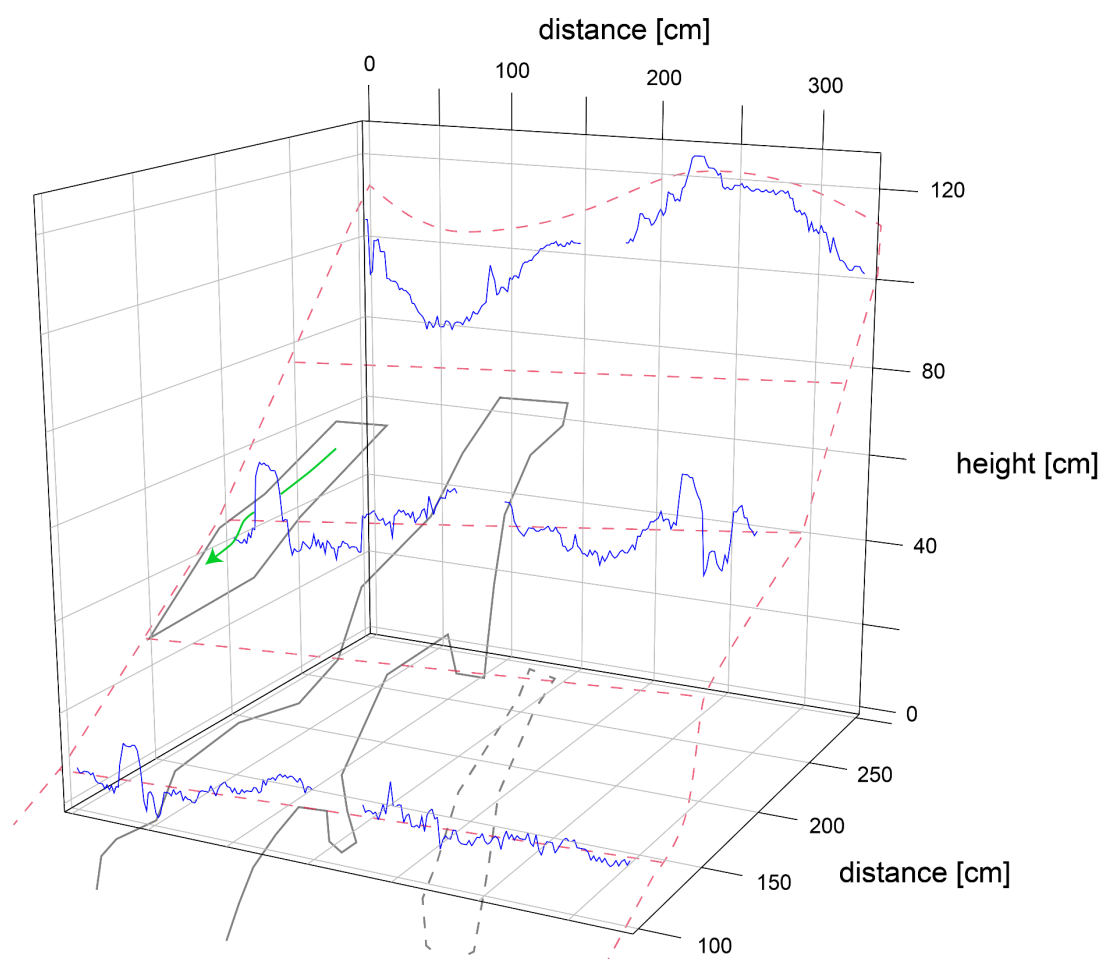


Figure 6.7 3-dimensional visualization of the microtopography lines (blue) for the lower part of the 1990s right plot (transsects v to x). The dashed red lines schematically represent the plot boundaries and the horizontal ropes. The black shape outlines on the plot represent the sketched pattern of the dye tracer (continuous) and observed surface flow (dashed), as presented in Figure 6.5. The green arrow indicates the flow around the local topographic “high”.

6.5 Correlation analysis

The principal component analysis of the site characteristics (Figure 6.8) explained 88.3 % of the variance within the first two principal components. Principal component 1 (PC1) explained 50.1 % of the variance and was mainly described by the average saturated hydraulic conductivity and the two vegetation measures (vegetation cover and number of plant species). Principal component 2 (PC2) explained 38.2 % of the variance and was described by the surface roughness measures (random roughness and tortuosity index) and the slope angle. The 3k and 1860s moraines were more densely vegetated (higher vegetation cover and had more different plant species) than the 1990s plots but had lower surface K_{sat} values (PC1). On the other hand (PC2) the 1990s right and middle plots, as well as the 3k plot, had a rougher surface and smaller slope angles than the other plots (see also Table 3). However, the separation of the points was not as clear as for PC1.

Comparing the four distance measures of the sand movement with all five site characteristics and the first two principal components revealed some significant correlations. Although both Pearson and Spearman rank correlations were tested, only the Spearman rank correlations are described here. In brackets the significant sediment transport distances (50 %, 75 %, 90 %, max), the correlation coefficient (r_s) and their p-values are shown. The full tables with all correlation values and their p-values can be found in Appendix 2.

Overall not many significant correlations were found, most of them for the maximum distance (Figure 6.9, Figure 6.10, Figure 6.11). For the low intensity simulation sediment transport distance was significantly correlated with the tortuosity index (max: $r_s = 0.83$, $p = 0.058$), the vegetation cover (75 %: $r_s = -0.89$, $p = 0.033$; max: $r_s = -0.94$, $p = 0.017$) and the number of plant species (max: $r_s = -0.75$, $p = 0.084$). For the mid intensity simulations, transport distance was correlated with slope angle (50 %: $r_s = -0.90$, $p = 0.083$; 75 %: $r_s = -0.90$, $p = 0.083$), vegetation cover (max: $r_s = -0.90$, $p = 0.083$), number of plant species (max: $r_s = -0.87$, $p = 0.054$) and PC1 (max: $r_s = -0.90$, $p = 0.083$). For the high intensity, transport distance was correlated with vegetation cover (max: $r_s = -0.90$, $p = 0.083$), number of plant species (max: $r_s = -0.87$, $p = 0.054$) and PC1 (max: $r_s = -0.90$, $p = 0.083$). All significant correlations were negative, except for the tortuosity index, indicating that they reduced the transport of sand. The only positive correlation indicates an increase in surface roughness leads to further sand transport.

The four distance measures of the sand movement were not clearly related to the surface runoff ratio and the sediment load. Only for the mid intensity, both the surface runoff ratio (50 %: $r_s = 0.87$, $p = 0.054$; 75 %: $r_s = 0.87$, $p = 0.054$) and sediment load (50 %: $r_s = 0.98$, $p = 0.005$; 75 %: $r_s = 0.98$, $p = 0.005$) were significantly correlated with the transport distance (Figure 6.12).

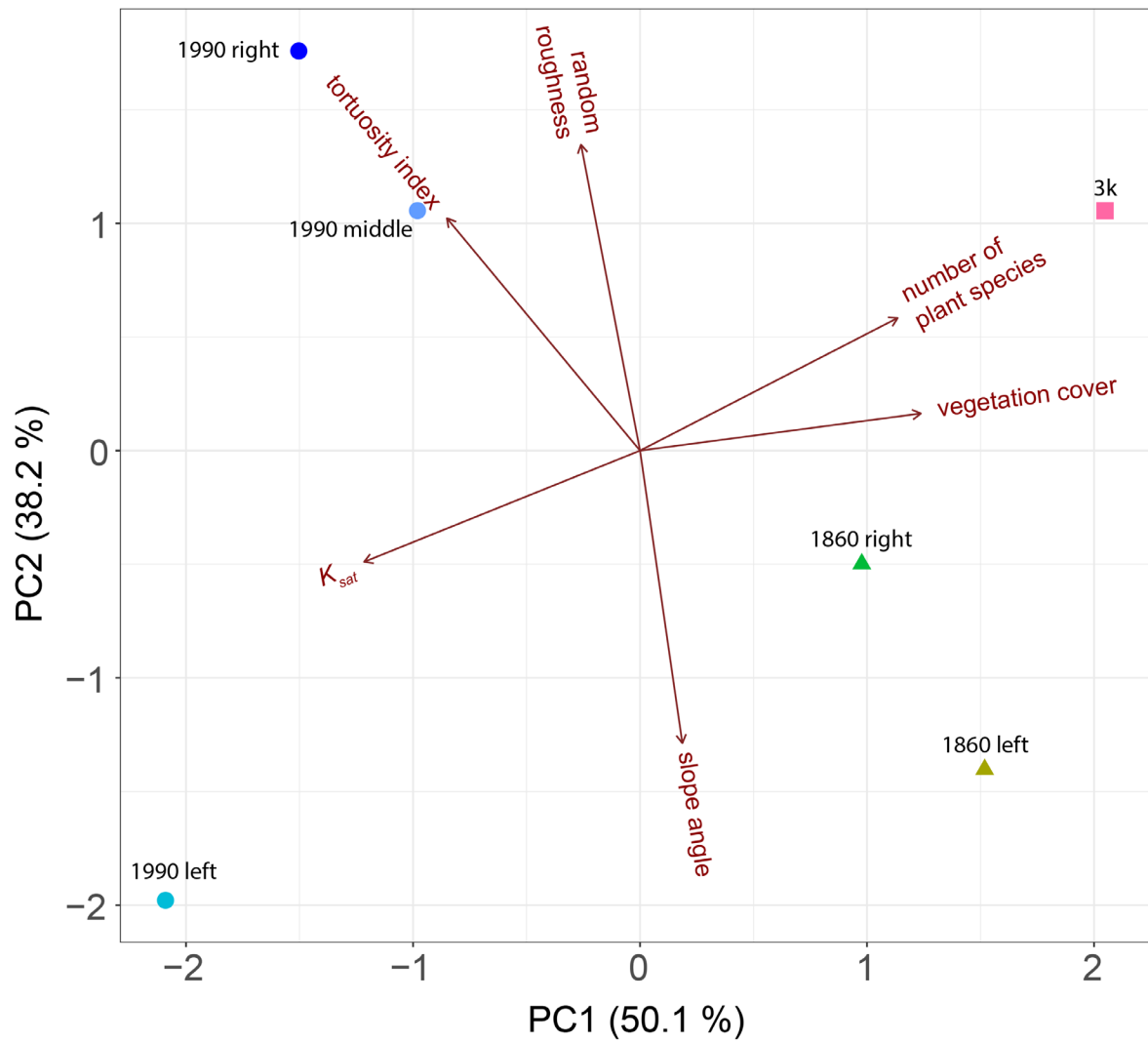


Figure 6.8 The two first principal components (PC1, PC2, based on the PCA) for the five site characteristics (vegetation cover, number of plant species, slope angle, tortuosity index, random roughness, saturated hydraulic conductivity K_{sat}) for all six experimental plots (shown with symbols). The explained variance of the principal components is indicated in the axes labels.

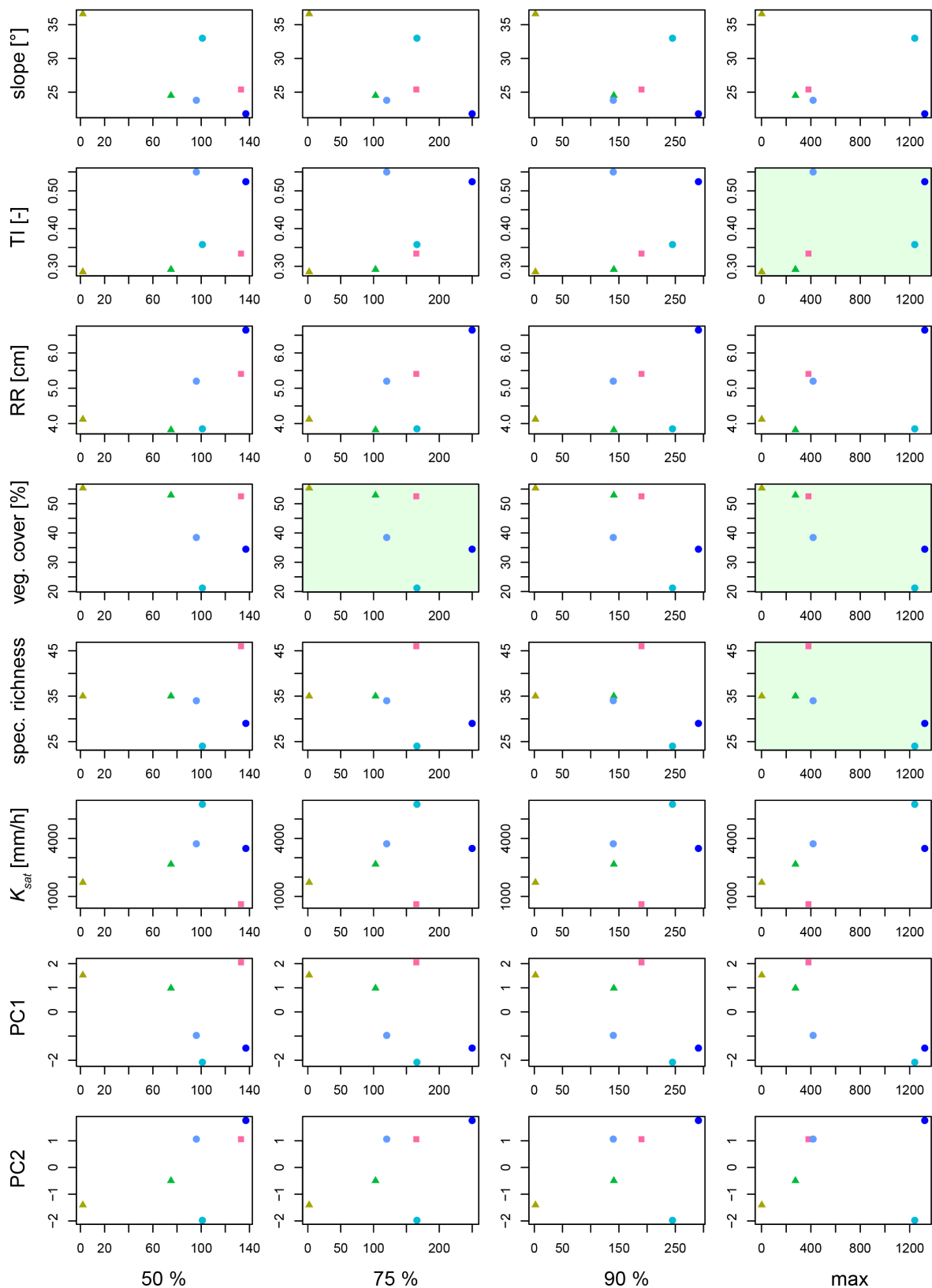


Figure 6.9 Scatterplots of the relations between the four sand distance measures (based on the relative cumulative travel distances: 50 %, 75 %, 90 % and maximum distance) and the mean value of the site characteristics (slope ($^{\circ}$), tortuosity index TI (-), random roughness RR (cm), vegetation cover (%), number of plant species (spec. richness), saturated hydraulic conductivity K_{sat} (mm/h)) and the first two principal components (PC1, PC2) of the PCA of the site characteristics for the **low rainfall** intensity experiments. The green colored shading indicates significant Spearman rank correlations (significance level: $\alpha = 0.1$). The colored symbols represent the experimental plots (see Figure 6.12).

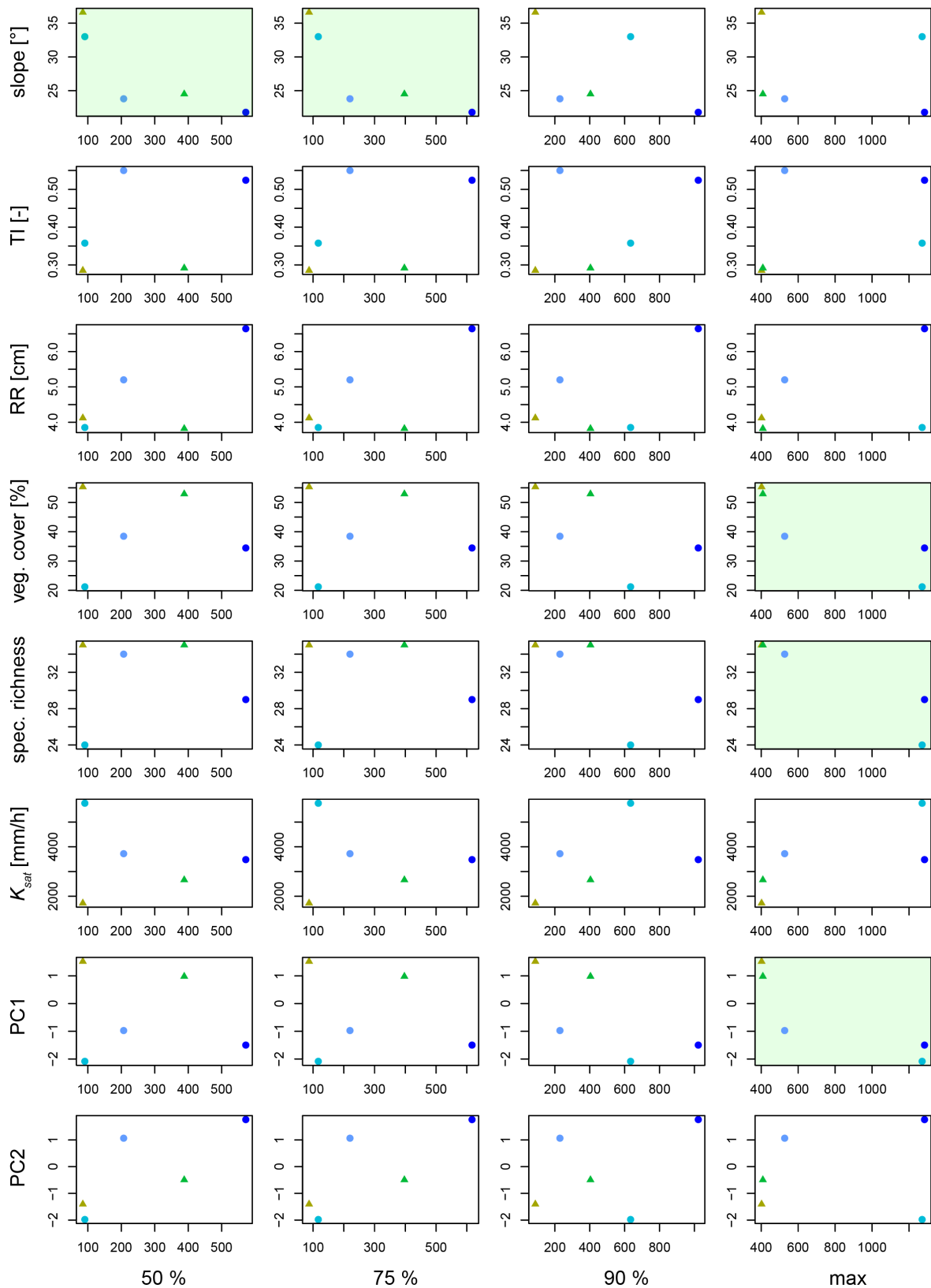


Figure 6.10 Scatterplots of the relations between the four sand distance measures (based on the relative cumulative travel distances: 50 %, 75 %, 90 % and maximum distance) and the mean value of the site characteristics (slope ($^{\circ}$), tortuosity index TI (-), random roughness RR (cm), vegetation cover (%), number of plant species (spec. richness), saturated hydraulic conductivity K_{sat} (mm/h)) and the first two principal components (PC1, PC2) of the PCA of the site characteristics for the **mid rainfall** intensity experiments. The green colored shading indicates significant Spearman rank correlations (significance level: $\alpha = 0.1$). The colored symbols represent the experimental plots (see Figure 6.12).

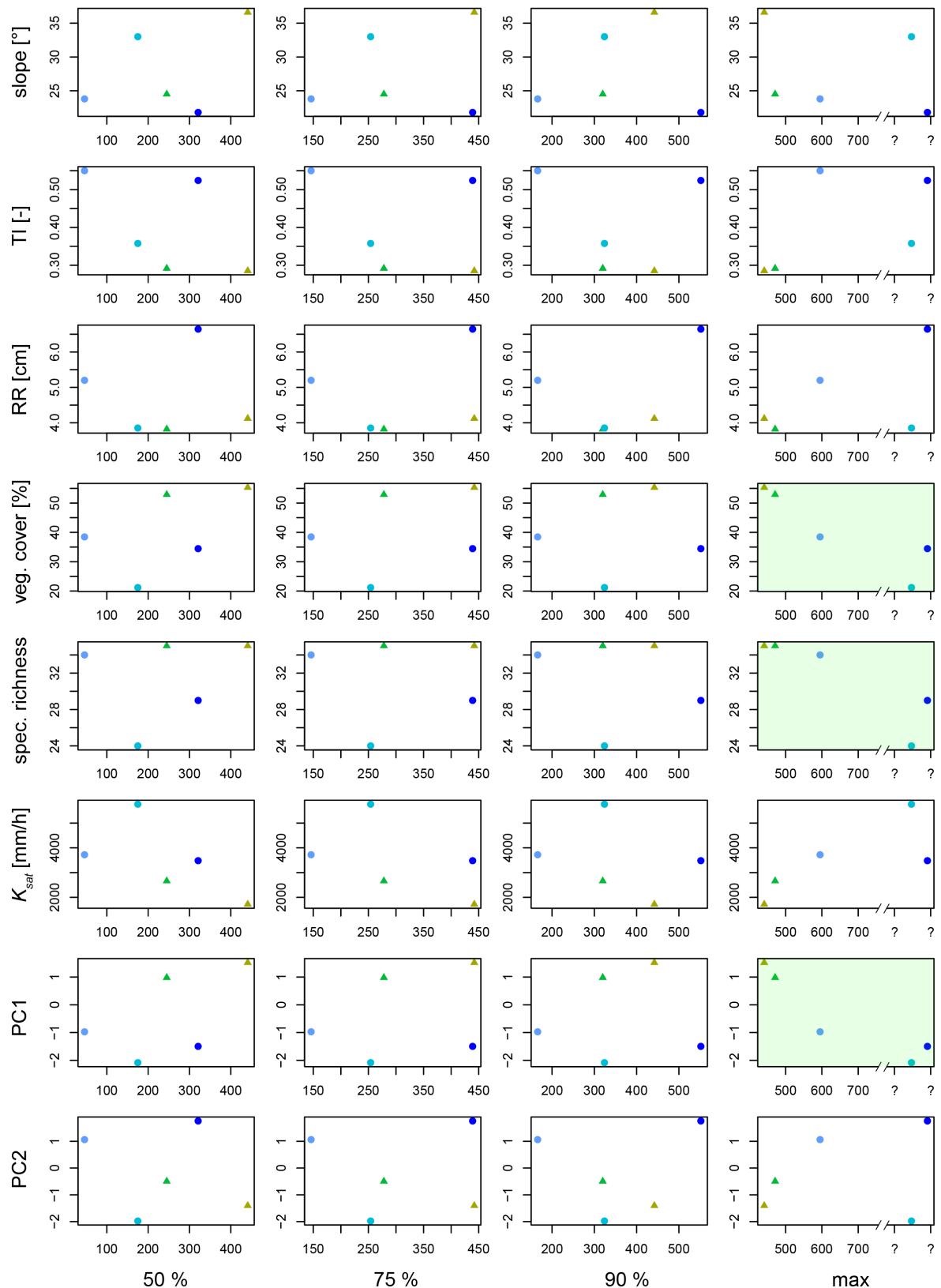


Figure 6.11 Scatterplots of the relations between the four sand distance measures (based on the relative cumulative travel distances: 50 %, 75 %, 90 % and maximum distance) and the mean value of the site characteristics (slope ($^{\circ}$), tortuosity index TI (-), random roughness RR (cm), vegetation cover (%), number of plant species (spec. richness), saturated hydraulic conductivity K_{sat} (mm/h)) and the first two principal components (PC1, PC2) of the PCA of the site characteristics for the **high rainfall** intensity experiments. The green colored shading indicates significant Spearman rank correlations (significance level: $\alpha = 0.1$). The colored symbols represent the experimental plots (see Figure 6.12). For the 1990s left and right plots sand moved below the plot boundaries (indicated with a break in the x-axis).

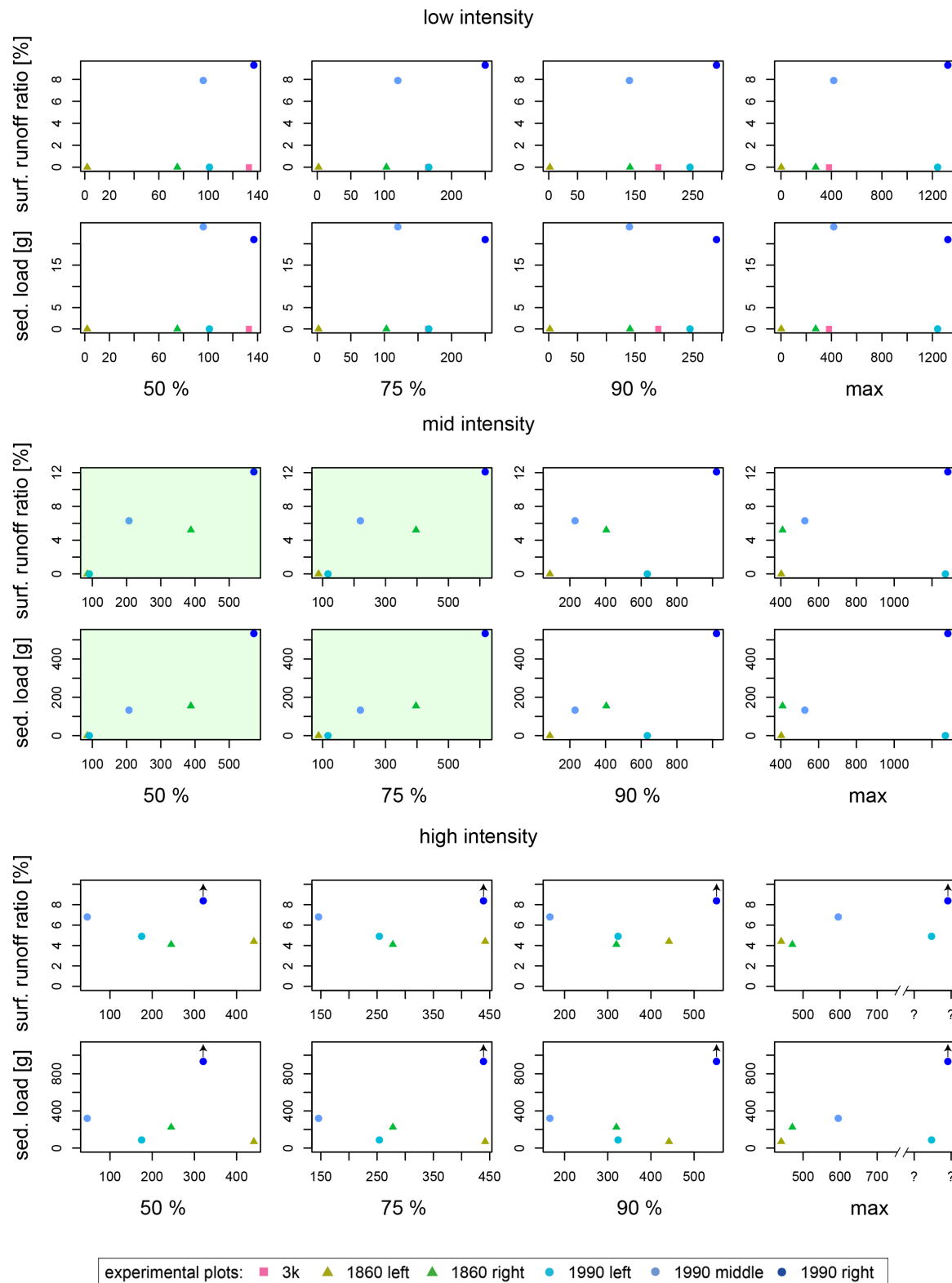


Figure 6.12 Scatterplots of the relations between the four sand distance measures (based on the relative cumulative travel distances: 50 %, 75 %, 90 % and maximum distance) and the values of the surface runoff ratio (%) and the sediment load (g) for the low, mid and high intensity rainfall simulation. The green colored shading indicates significant Spearman rank correlations (significance level: $\alpha = 0.1$). The shapes and colors of the symbols represent the experimental plots and are the same as used in the other graphs. For the low intensity event surface flow and, hence, also sediment transport to the bottom of the plot only occurred on the 1990s middle and right plots. The surface runoff ratio and the sediment load for the 1990s right plot are slightly underestimated because of a lack of measurements after the experiment stopped (indicated by the black arrow). For the high intensity simulation sand moved below the plot boundaries on the 1990s left and right plots (indicated with a break in the x-axis).

7 Discussion

7.1 Evaluation of the new fluorescent sand method

The distribution of the sand is affected by the combination of various factors, including different site characteristics. This highlights the challenges of finding an appropriate method or metric to obtain a better understanding of surface hydrological connectivity. In contrast to Tauro *et al.* (2012b) a qualitative detection of surface connectivity was possible because a sand tracer was used instead of buoyant polyethylene balls. The new method showed promising results for the determination of sediment connectivity and surface hydrological connectivity.

7.1.1 Field setup

The fluorescent segmented chains were fixed with tent pegs. On the left and right sides of the plot the plot boundaries gave additional stability to the chain. Where the chain crossed the plot, tent pegs could not be used to stabilize the chain because they would disturb the plot surface and the flow on the surface. Hence, the chain was hanging down, which led to a slight bending of the tent pegs over the days. This meant a slight change in the reference points relative to the ground between the photos. It happened also slightly on the left and right borders (but less). The change in the reference grid was in the range of a few millimeters.

The chosen reference points (change of the color of the segmented chain) were too large, meaning that it was not a point on the photo but rather a small area. The high pixel resolution of the camera made this worse because the area consisted of more pixels. The manual selection of the reference points in Python 3, thus, led to some inaccuracy as well, but this was also on the millimeter range. Because the reference points were rather small “reference areas”, every time a photo was newly geometrically corrected, a slightly different correction was applied. This “reference areas” could lead to a larger difference when subtracting the extracted sand after a rainfall experiment from the extracted sand before the experiment. A fully correct subtraction would only work if both images could be perfectly placed on top of each other and this is only possible for unique, not moving, and small reference points. Thus, uncertainties within the range of about 1 cm should be assumed for the used distance measures. This is high compared to other studies which reached spatial reliable resolutions of 1 mm (Hardy *et al.*, 2019) or even < 1 mm (Hardy *et al.*, 2017). Nonetheless, in terms of estimating maximum travel distances to get an idea of possible erosion, it is acceptable.

The slope parallel fluorescent ropes (stretched over the plots at 0.5 m intervals) were a huge drawback. They were useful in the field for the direct estimation of the sand movement but had to

be removed in Adobe Photoshop later in order to correctly extract the orange sand, as they emitted in the same wavelength range as the sand. Additionally, they blocked the view to the sand below them. Thus, a different color rope (or no rope) should be used in the future.

The camera used to capture the distribution of the sand was mounted on a tower below the plot, leading to a smaller angle ($\lambda < 90^\circ$) between the average plot surface and the camera lens ($\lambda = 90^\circ$ indicates a camera lens pointing straight down from the nadir, see also Figure 7.1a). The smaller angle could inhibit detection of sand particles behind larger objects. Thus, if large rocks were present on the plots, sand behind these rocks could not be detected due to so called ‘*shadowing effects*’ (e.g. on the 1990s middle plot – see also chapter 7.2). This is clearly visible when comparing a photo from the camera tower with a drone-based image taken with a DJI Phantom 4 Pro and nadir view (Figure 7.1b and c). Hardy *et al.* (2019) took photographs at only 2 m height above ground to study particle tracing on tilled farmland. At only 2 m height soil aggregates (after tillage) could shield areas with tracer particles. However, they did not address this important limitation which questions their results.

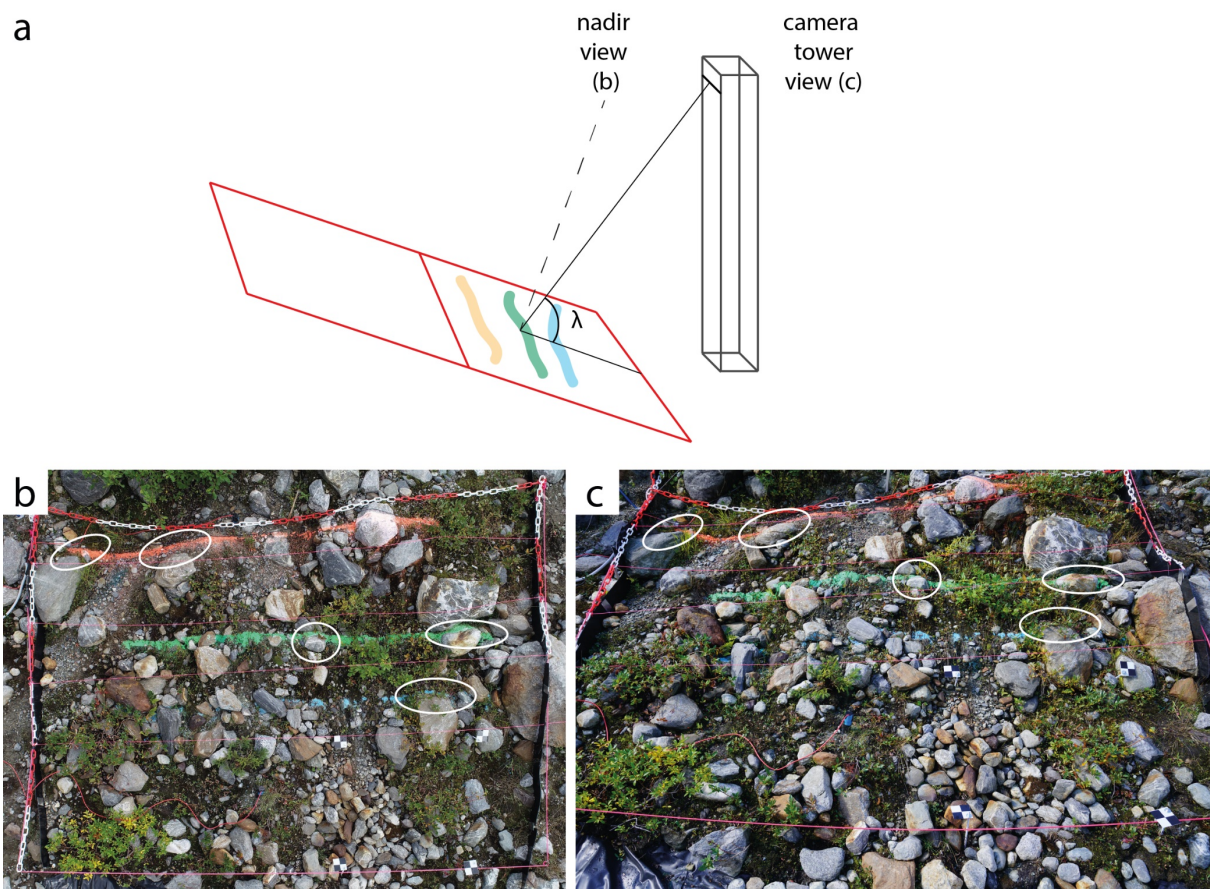


Figure 7.1 (a) Sketch of the camera tower and an experimental plot. The angle λ between the camera lens and the average plot surface is 90° from the nadir view (b) and smaller from the camera tower view (c). The nadir photo (b) of the 1990s right plot was taken with a DJI Phantom 4 Pro. The photo from the tower camera (c) was not taken at a nadir view. The white ellipses indicate areas where sand is not clearly visible on the picture from the tower camera.

On the 1990s moraine the orange sand line (low intensity) was placed in the middle of the plot, the green line (mid intensity) 50 – 60 cm below and the blue line (high intensity) another 50 – 90 cm downslope. The placement of the fluorescent sand lines was not optimal, as the sand lines were too close to the end of the plot and sand moved out of the detectable range. Starting with the orange sand line in the middle of the plot had the advantage of a larger “catchment area” on the plot above the line. In retrospect, it would have been better to place the lines further up on the plot and closer together. Because sediment transport strongly depends on the soil surface, it is therefore highly variable in space (Parsons *et al.*, 2004). The lines should, thus, be closer together in order to be able to better compare the measured sand distances of the different rainfall intensities. In contrast, for the evaluation of surface connectivity, the placement of the sand lines further apart was better since more flow paths could be observed (covering a larger total area). This results in a trade-off between the two interests and, hence, with interest in both, sediment transport distances and surface connectivity, the chosen distance between the sand lines (50 - 90 cm) seems acceptable.

The glow in the dark sand in combination with the fluorescent reference grid and the UV-lamps had the advantage that no wavelength filter had to be used on the camera as for example in the setup of Hardy *et al.* (2019). In addition, no real-time particle tracking (as used by Tauro *et al.*, 2012b, 2012a, 2016, Hardy *et al.*, 2016, 2017) was used since sand was not only detached but also deposited on the plot surface (see also chapters 6.4 and 7.5) which led, compared to the other studies, to a relatively easy setup. However, if the goal was to extract exact particle travel distances (and not only estimates) real-time particle tracking would be necessary, as performed by Hardy *et al.* (2017) on soil surfaces.

7.1.2 The fluorescent sand

After being exposed to water, the fluorescent sand clumped together and formed small aggregates (size: 1 - 15 mm) when the sand was drying. These aggregates were not easily destroyed by raindrops, leading to reduced sand movement during subsequent rainfall experiments. This was observed in the field during the last irrigation experiment (high intensity) on the 3k plot. The clumping of the sand was probably caused by a glue, that should prohibit the removal of the glowing color TAT 33 from the quartz sand particles. It was, thus, not possible to use a sand line for more than one rainfall experiment in order to study the sediment transport distances. This is also the reason why no sediment transport data for the 3k plot (where only one sand line was applied) was obtained for the mid and high intensity rainfall simulations (n/a in Table 5).

The quality of the fluorescent sand also depended on the sand color. The glowing color coating (TAT 33 and a glue) of the blue sand was more easily washed from the quartz sand particles than from the orange and green particles, leading to more undetectable particles in the post processing for the blue sand. Due to the insufficient quality of the blue sand, it should not have been used for the high intensity simulation where even more energy was available to leach the color.

The ability of the sand to glow, without the need of constant UV- light, is a great advantage of the tested method. As this study was performed on glacial moraines, the surface roughness was high and thus many obstacles created UV- light shaded areas. Nevertheless, the sand particles still emitted light and could thus be captured on the photographs. Hardy *et al.* (2019) used, as many other studies (Young and Holt, 1968; Tauro *et al.*, 2012b, 2012a, 2016, Hardy *et al.*, 2016, 2017), particles that need constant UV-light exposure in order to be visible in the dark and were, thus, not able to see particles in the shadows.

7.1.3 Photo analyses

A major limitation of the geometric correction code of Weiler (2001), that was used in this study, is the inability to extrapolate beyond the range of the chosen reference points. This was not necessary for the extraction of brilliant blue dye tracer in the soil because a wooden grid was placed around the transects (see Weiler and Flühler, 2004). However, for the extraction of the sand distribution on the surface, this method would have resulted in more accurate results (compared to the linear extrapolation of the grid outside the photo; see Figure 5.1) as sand particles that moved beyond the last reference point needed to be included in the analysis. The geometric correction outside the reference points could not be included in the code due to lack of time.

Because of the “reference areas” instead of reference points, the top left corner (coordinate 0, 0) of the corrected images was not always exactly at the same location (uncertainty of about 1 cm as described in chapter 7.1.1). Thus, for the subtraction of the sand lines (see chapter 5.2) the peak of the sand lines was chosen (Figure 5.3) as reference for the overlap of the photos before and after the experiments. This peak was assumed to be at about the same location before and after the experiments (because the sand line was about 2 cm high and not all of that sand would move during a rainfall experiment). It was assumed that this would lead to more accurate results than subtracting the complete images (overlapping at the coordinate 0, 0) from each other. However, because of infiltration and sand movement, the peak of the sand may not have been at exactly the same locations, which would have led to additional uncertainties in the travel distances.

The sand colors green and blue were not optimal as their emitted wavelength ranges almost overlap. This caused additional uncertainty during the sand extraction process because of

misclassifications (see chapter 5.2). Additionally, the blue coating partly washed off the sand. The pure quartz sand had a white color which could not be detected because the background also contained white elements. Sand particles partly covered in soil material or submerged in small ponds in depressions could also not be detected in post processing. However, this is a common problem and was also found by Hardy *et al.* (2019).

The conversion of the rgb photos to the hsv color scheme was a good choice. Using only one channel of the rgb photos did not lead to satisfactory results and for each color a combination of channels would have been needed. The separation of the three sand colors in the hsv, using sand's hue was the only objective method that led to reasonable results. Other common objective and reproducible procedures for color-based object extractions used in remote sensing, such as unsupervised classification methods resulted in significantly worse results. However, with supervised classification algorithms (e.g. maximum likelihood) nearly equally good results could be achieved (see Appendix 4). Such methods are subjective and not reproducible and, thus, they were not considered further. For a description of the mentioned methods see for example Lillesand *et al.* (2015) or Mather *et al.* (2016).

7.1.4 Measures of sediment transport

The “reference areas” instead of reference points, the small covered areas by the fluorescent ropes on the plots and the position of the camera led to the inability to calculate the actual size of sand covered areas after a rainfall experiment. Secondly, it led to uncertainties in the measures of the sand movement, particularly for the 50 %, 75 % relative cumulative frequency of transport distances, and partly also the 90 % relative frequency. For the maximum distance the values were assumed to be more accurate, since the angle between the plot surface and the camera lens (λ) was larger for the lower end of the plot and because no large rocks were located within these areas (see also Figure 3.2). The four distance measures were, thus, not always meaningful but because of uncertainties related to each of them, it was preferred to report the results for all of the distance measures.

On the experimental plots where almost exclusively splash erosion occurred so that only some sand particles or aggregates (e.g. attached to a pebble) moved, the 50 %, 75 % and 90 % relative cumulative frequency based distances were not so informative. Instead, rather the maximum distance should be used (see chapter 7.2). The shorter distance measures are particularly useful to compare plots where erosion processes by surface flow dominated.

7.2 Dominant erosion processes

Splash erosion is a relatively inefficient process for sediment detachment and transport (Bracken *et al.*, 2015), and fewer particles are transported compared to sheet wash. According to Long *et al.* (2014) only about 4 % of the momentum of raindrops, at the surface, lead to the detachment and movement of particles. Hence, on the experimental plots, where only few sand particles moved, erosion by rain splash is assumed to be the dominant erosion process. On strongly vegetated plots (3k, 1860 left, 1860 right) fluorescent sand was only found on some spots below the line for all rainfall intensities (Figure 6.2a-c; see also photos of the sand in Appendix 3). The main reason for this is the presence of dense vegetation (over 50 % vegetation cover), which increases the resistance for sediment movement (Berendse *et al.*, 2015). The DTM based flow accumulation for the sand covered areas was also low (Figure 6.6) and no distinct surface flow was observed during the experiments. However, splash erosion was observed on these plots. Due to splash erosion sediment particles could be transported over larger barriers, such as rocks and vegetation. Higher distances are possible with higher rainfall intensities, as the movement of the particles is dependent on the kinetic energy of the rain drops (Pietravalle *et al.*, 2001).

The 1990s middle plot was similar to plots of the 3k and the 1860s moraines in terms of the sand movement, as sand was barely transported downslope. The vegetation cover and the number of plant species was higher than for the 1990s left and right plots and thus more similar to the plots of the 3k and 1860s moraines. However, surface flow was observed on the plot surface during the experiments which rather indicates surface flow to be the dominant erosion process. Compared to the 3k and the 1860s left and right plots, the saturated hydraulic conductivity was rather high for the 1990s plot, leading to more infiltration of sand particles into the soil and less sediment transport on the surface. According to the DTM, flow accumulation was high on the right side of the plot. Large rocks just below the sand lines blocked the surface flow and led to a different routing of the water (infiltration). Additionally, the rocks blocked the view of the camera (shadowing effect; see also chapter 7.1.1), and all the sand between those rocks was not detected (Figure 7.2a). The high infiltration and the rocks that blocked the surface flow may have caused the relatively short sand transport distances for the middle 1990s plot. The real travel distances, however, may be higher since the rocks also blocked the view of the camera.

On the left and right plots of the 1990s moraine the sand was transported more evenly over the surface (Figure 6.2d and f). Surface runoff was observed during the experiments and also suggested by the DTM flow accumulation. Compared to the other plots the vegetation cover and the number of plant species was lower. Hence, surface flow was assumed to be the dominant erosion process.

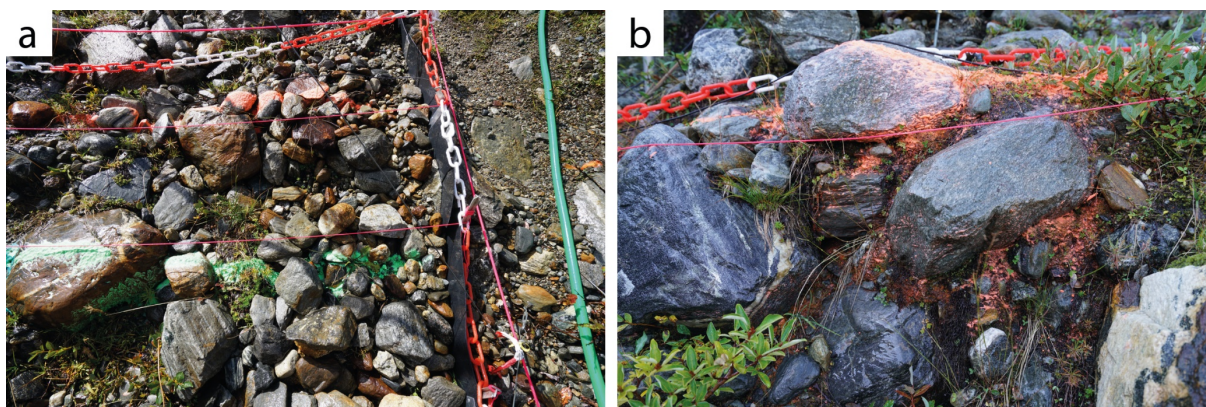


Figure 7.2 (a) Example of rocks blocking the sand flow (on the surface) on the top right corner of the 1990s middle plot below the orange and green sand line. (b) Orange sand, that easily flowed over the rock surfaces of the 1990s right plot in the top right corner.

7.3 Effects of site characteristics on sediment transport

Since sand transport on half of the experimental plots was dominated by splash erosion, the maximum sand movement is the most reliable measure for sediment transport within this study. However, since sand was placed loosely on the surface before the rainfall experiments, and because the sand was not fully representing the grainsize distribution of the underlying soil (but only a fraction), the measured distances do not represent actual erosion rates and would rather indicate maximum values for local surface erosion.

The site characteristics that were significantly correlated with at least one of the four distance measures for the sand movement for all rainfall intensities were vegetation cover, number of plant species, slope angle, surface roughness (tortuosity index) and PC1. Overall vegetation cover (average Spearman rank correlation factor of -0.91 over all rainfall intensities) and the number of plant species (average Spearman rank correlation factor of -0.83 over all rainfall intensities) were the most important factors in determining the amount of sediment transport on hillslope surfaces. Slope angle and surface roughness could also have an effect. These findings are consistent with the findings of Battany and Grismer (2000), where vegetation cover was found to be the most important factor. Slope angle and surface roughness had a secondary influence. Rodrigo Comino *et al.* (2016) also found vegetation to have the largest effect on runoff generation and sediment transport and slope angle as a secondary factor. Additionally, also stone cover and pre-experiment soil moisture conditions were found significant. Stone cover was not directly measured on the experimental plots in this thesis; however, stones of different sizes dominated the surface on the 1990s moraine and also more surface flow and sediment runoff was observed.

Vegetation cover and the number of plant species were significantly negative correlated with the maximum sand transport distance for all three rainfall intensities. This was also observed for

PC1, which mainly described the two vegetation measures. The influence of the vegetation on the movement of the fluorescent sand can also be seen in Figure 6.4, where the area where sand transport and deposition occurred was smaller for the stronger vegetated plots (3k, 1860 left, 1860 right) than for the other three plots. On the 1990s middle plot also less sand moved than for the left and right plots. This can be explained by the higher vegetation cover and larger number of plant species. The negative relation between vegetation cover and sediment movement is consistent with the findings of many other studies (Battany and Grismer, 2000; Rey *et al.*, 2004; Zhang *et al.*, 2004; Marques *et al.*, 2007; Wei *et al.*, 2007; Zhou *et al.*, 2008; Rodrigo Comino *et al.*, 2016) and can be explained by increased soil stability, increased resistance (Berendse *et al.*, 2015), higher interception (El Kateb *et al.*, 2013), lower potential for abrasion and higher rate of local sedimentation (Rey *et al.*, 2004; Sandercock and Hooke, 2011). The negative relation between the number of plant species and the sediment transport is more difficult to explain. Allen *et al.* (2016) found that the number of plant species indirectly increases the number and length of roots, which brings more soil stability and less erosion. Hou *et al.* (2016) reported that there is a strong relationship between the number of plant species and vegetation cover and that the correlation between the number of plant species and sediment transport depends on the vegetation patterns. For example, for heterogeneously distributed vegetation, vegetation cover increases with the number of plant species causing sediment transport to decrease. However, for homogeneously distributed vegetation, vegetation cover decreases with a larger number of plant species and sediment transport increases. On the six experimental plots vegetation patterns were heterogeneous, and thus the findings are consistent with those of Hou *et al.* (2016).

Slope angle was only significantly correlated with the 50 % and 75 % relative cumulative frequency of transport distances for the mid intensity events (but not for the 90 % and maximum distance). Because the relation (degree and orientation, see also Appendix 2) between the transport distance and slope angle differed for different distance measures and rainfall intensities and because no significant correlation with the maximum distance was found, the correlation analysis of the slope angle should be interpreted with caution. Additionally, the significant correlation was negative, indicating that smaller slope angles would lead to larger transport distances for the sand. This is unexpected because most studies show that erosion rates are higher for steeper slopes (Evans, 1980; Cerdà and García-Fayos, 1997; Koulouri and Giourga, 2007; El Kateb *et al.*, 2013; Martínez-Murillo *et al.*, 2013; Rodrigo Comino *et al.*, 2016). Nevertheless, some studies also found increasing erosion rates with increasing slope angle up to a threshold value and decreasing erosion rates after that (Bryan, 1979; Evans, 1980; Qing-quan *et al.*, 2001). This was also found by Liu and Singh (2004), for surface flow velocity and shear stress, which influence sediment transport. The reason for the threshold value is complex and is related to changes in vegetation cover, plant species richness (Nadal-Romero *et al.*, 2014), surface flow velocity, shear

stress, erosion-resisting capacity, infiltration etc. which change with increasing slope angles (Bryan, 1979; Qing-quan *et al.*, 2001).

The tortuosity index was significantly correlated to the maximum sediment transport distance for the low intensity simulation but the trend (Figure 6.9) is not as clear as e.g. for vegetation cover and should be interpreted with caution. The real transport distance for the 1990s middle plot would probably be larger. If this were true, the correlation would be better resulting in a more linear correlation. This also applies for the mid and high intensity simulations. Nevertheless, the positive correlation for the low intensity simulation is consistent with the results of other studies (e.g. Römken *et al.*, 2002; Vermang *et al.*, 2015). Rougher surfaces lead to more sediment transport because of more changes in the drainage network during precipitation events when surface runoff occurs (Römken *et al.*, 2002). However, surface roughness could also be negatively correlated to the sediment transport (Ziadat and Taimeh, 2013) and, thus, the direction of the significant correlation was not meaningful (given the small sample size). More sediment transport on the surface would mean that also the sediment load (in the measured surface runoff) would be higher. However, the sediment loads for the low intensity rainfall simulations (Figure 6.12) were rather low and only for two plots different from zero (Table 4). Thus, even if the sand on the plot surface moved, it did not reach the downslope end of the plot. This is a strong indication for the complex interconnections and linkages between different parts of a hillslope (see also chapter 7.5). Surface runoff can occur locally but also disappear again due to infiltration, as e.g. seen in the ponding with the dye tracer on the 1990s right plot (see Figure 6.5a). These findings are consistent with those of Römken *et al.* (2002) who found no increased sediment export (soil loss) from rougher surfaces overall but locally increased sediment loads in the surface runoff.

K_{sat} was not significantly correlated to the sediment transport distances, which is surprising. The K_{sat} values on the plots were typical for the corresponding soil or moraine material and are within the range of “sand” (42 – 4170 mm/h), “poorly sorted sand and gravel” (208 – 4170 mm/h) and “gravel” (4170 – 41700 mm/h; Hendriks, 2010). As expected, the surfaces dominated by gravel (the three plots on the 1990s moraine) had higher K_{sat} values than the others. The PCA further suggested a negative relation between the two vegetation measures (vegetation cover and number of species) and K_{sat} , which indicates lower infiltration rates for the vegetated areas. However, the measured saturated hydraulic conductivity was always higher than the applied rainfall intensity. The lowest measured K_{sat} was for the 3k plot (600 mm/h) but this was still approximately seven times higher than the actual high rainfall intensity on this plot (89 mm/h; see Table 2). Nonetheless, surface runoff was observed on all plots for the high intensity simulation, suggesting the occurrence of saturation excess runoff (Dunne and Black, 1970) instead of infiltration excess runoff (Horton, 1933). Note, however, that the measured surface runoff is not

equivalent to pure overland flow, as the plastic foil was inserted just below the sod and the surface runoff thus included biomat flow (see chapter 4.2.2). Also, other factors could be responsible for the further sand movement on the less vegetated plots (1990 left and right). The high spatial variability of soil properties leads to very heterogeneous infiltration rates that often change over short distances (van Schaik, 2009). This is even more distinct for glacial moraine material with the strong variability in the grain and gravel sizes, which is thought to influence the local development of soils (Johnson *et al.*, 2015). It allows water flow over the surface and infiltration at other locations (see e.g. flow towards the ponding in the lower parts of Figure 6.5a). Moreover, rock surfaces have K_{sat} values close to zero. Rocks cover a large portion of the surface of the three plots on the 1990s moraine. Since no water infiltrates there, it is forced to flow over the rock surface before infiltrating into the soil. Sand on such rocky surfaces, thus, moves easily with the water (Figure 7.2b). In contrast on vegetated plots, the vegetation itself functions as resistance (Berendse *et al.*, 2015), and even if water would flow on the surface (as suggested by the DTM based flow accumulation), sand particles may be stopped. Additionally, the soils are more stable because of the higher rooting density (Allen *et al.*, 2016), impeding the process of detachment. This is not relevant for the sand from the line, as it was loosely placed on the soil surface, but generally applies for other sediment particles and is therefore of major importance to understand surface erosion.

7.4 Effect of rainfall intensity on sediment transport

The sand movement generally increased from the low to the mid intensity rainfall simulation for all four distance measures (Figure 6.3), indicating an increase in sediment transport with increasing rainfall intensity. This is congruent with the findings of various other studies (see e.g. Römken *et al.*, 2002; Zhang *et al.*, 2011; Defersha and Melesse, 2012; Martínez-Murillo *et al.*, 2013; Ziadat and Taimeh, 2013; Wen *et al.*, 2015; Khan *et al.*, 2016; Xu *et al.*, 2017) and is also intuitive as a higher rainfall intensity provides more kinetic energy on the soil surface (Evans, 1980) and should result in more surface runoff (Khan *et al.*, 2016). The blue sand lines had more gaps (in the line) than the orange and green lines (see Figure 6.4 and Appendix 3), indicating that more sand was washed away by surface runoff, infiltration and splash erosion during the high intensity rainfall simulation. However, the determined sand travel distances decreased from the mid to the high intensity simulations (especially in the 50 %, 75 % and 90 % relative cumulative frequency of transport distances). The maximum sand movement, however, increased with increasing rainfall intensity for all plots, except for the 1990s left and right. This could be partly explained by the bad quality of the sand (chapter 7.1.2), resulting in white quartz sand particles (after the experiment) that could not easily be distinguished from the background. Another factor could be a higher

infiltration of the sand below rocks and into the soil. As already mentioned in chapter 6.3, blue sand particles were found in the gutters below the plot, indicating that the sand had moved off the plot and the determined travel distances are thus too short. Accounting for the mentioned factors one could argue that increasing rainfall intensity leads to higher sediment transport on hillslope surfaces. As the Spearman rank correlation coefficients for the driving factors (vegetation cover and number of plant species) were about the same over all rainfall intensities (see Table 8 in Appendix 2), but the maximum sediment movement increased with higher rainfall intensity, the rainfall intensity itself could be seen as the main factor determining sediment transport. This is congruent with the findings of e.g. Ziadat and Taimeh (2013), Wen *et al.* (2015) or Khan *et al.* (2016) who also found rainfall intensity to be the main driving factor for soil erosion (at least among the studied factors). However, there could also be other factors that are even more important. For example, Xu *et al.* (2017) found upslope inflow (to the studied area) to be more effective for soil erosion than rainfall intensity.

Sand movement was positively correlated to the surface runoff ratio and the sediment load measured at the bottom of the plot. The sediment load of the surface runoff is expected to correlate (positively) with both the observed sediment transport on the plot surface and the surface runoff itself. However, the positive correlation was only significant with the 50 % and 75 % relative cumulative frequency of transport distances and only for the mid intensity simulation (Figure 6.12). Hence, the results should also be interpreted with caution. For the low intensity only the 1990s middle and right plots had a sediment load that was different from zero. The two plots were located directly at the bottom of the hillslope, draining into the fluvial plane of the Steingletscher. Subsurface flow (measured in the first Upwelling Bernoulli Tube – see chapter 4.1) was continuously observed (also after several days of no natural rainfall), suggesting exfiltrating groundwater at this location. During the irrigation experiments, the soils on the two plots were thus saturated and surface runoff was generated earlier (e.g. in the form of partial area surface runoff (Betson, 1964), which is often observed at the lower end of hillslopes (Beven, 2012)) than for the other four plots. In contrast the 1990s left plot was located further up on the moraine and the slope was significantly steeper than for the other two plots. Additionally, K_{sat} was very high (comparable to pure gravel). The irrigated water on the plot, therefore, likely infiltrated deep. Surface runoff (and thus also sediment load) did not occur for the low and mid intensity experiments and was very small for the high intensity experiment. Nevertheless, local surface flow was observed, most likely because of the high spatial variability of the soil properties, and sand moved on the plots, even if no surface runoff was measured. This is a very important finding, as it shows the occurrence of surface flow and re-infiltration and highlights the importance of hydrological connectivity (see chapter 7.5).

7.5 Surface hydrological connectivity

Fluorescent sand transport was observed on all experimental plots and for all rainfall intensities, except on the 1860s left plot for the low intensity simulation. The main sand displacement happened via splash erosion (3k, 1860 left, 1860 right) and locally occurring surface flow, which re-infiltrated again on the plot area (1990 left, middle, right). Dominating processes on the latter plot surfaces were local re-infiltration and redeposition.

For the 1990s right plot, there was a good match between the distribution of the fluorescent sand after the experiments (Figure 6.4), the DTM based flow accumulation (Figure 6.6) and the movement of the dye tracer (Figure 6.5c). These findings suggest that the distribution of the sand is able to represent the paths of surface flow (at least on the 1990s right plot). Surface flow was mainly observed along rills (rill flow) and towards depressions (Figure 6.5a) as reflected by the microtopography (Figure 6.7), indicating that microtopography is an important factor determining surface hydrological connectivity. This is consistent with the classic view of surface hydrological connectivity. As water on a surface becomes available during rainfall events, e.g. due to saturation excess runoff (Dunn), it first flows into topographic depressions and ponding starts. When they are full and more water is added, they start draining into other depressions, and thus they become hydrologically connected (Appels *et al.*, 2011). The creation of such a hydrological runoff system was observed in the lower part of the 1990s right plot (Figure 7.3). Ponding was observed in depressions. Filled depressions overflowed and, thus, connected via overland flow with other locations.

In general, the local microtopography and, thus, local slope gradients defined the direction of flow on the surface as e.g. seen in the flow towards the left in the lower part of the 1990s right plot (Figure 6.5 and Figure 6.7). Surface hydrological connectivity depends on the distribution of topographic features but also vegetation patches that may act as hydrological sinks (Lesschen *et al.*, 2009; Meerkerk *et al.*, 2009; Cantón *et al.*, 2011) or barriers. Debris, litter, microtopography, slope length and slope angle are also considered to affect connectivity (Mayor *et al.*, 2008; Appels *et al.*, 2011; Reaney *et al.*, 2014).

Although splash erosion was not the dominant erosion process on the 1990s moraine (see chapter 7.2), it was still an important process and was also observed during all experiments. This suggests that the surface hydrological connectivity and sediment connectivity are not fully the same. Nevertheless, surface hydrological connectivity is the basis for sediment transport and is, thus, strongly linked to sediment connectivity (Bracken *et al.*, 2015). According to Ares *et al.* (2016) it is even a prerequisite. Since splash erosion only contributes to a minor part to sediment transport

(Long *et al.*, 2014; Bracken *et al.*, 2015), surface hydrological connectivity was relatively similar to the sediment connectivity on the plots where overland flow and sheet wash occurred (three plots on the 1990s moraine). On the other three experimental plots (3k, 1860 left, 1860 right), where erosion of the fluorescent sand was dominated by rain splash, only sediment connectivity was detected. The sediment connectivity on the three more vegetated plots was mainly influenced by the vegetation cover. Locally different plant types could also strongly influence the movement of sand particles (Sandercock and Hooke, 2011).

Better connectivity on hillslopes may lead to increased local surface runoff (Appels *et al.*, 2011) and, hence, also more sediment transport (Zimmermann *et al.*, 2014). This is congruent with the findings from the experimental plots of the 1990s moraine.

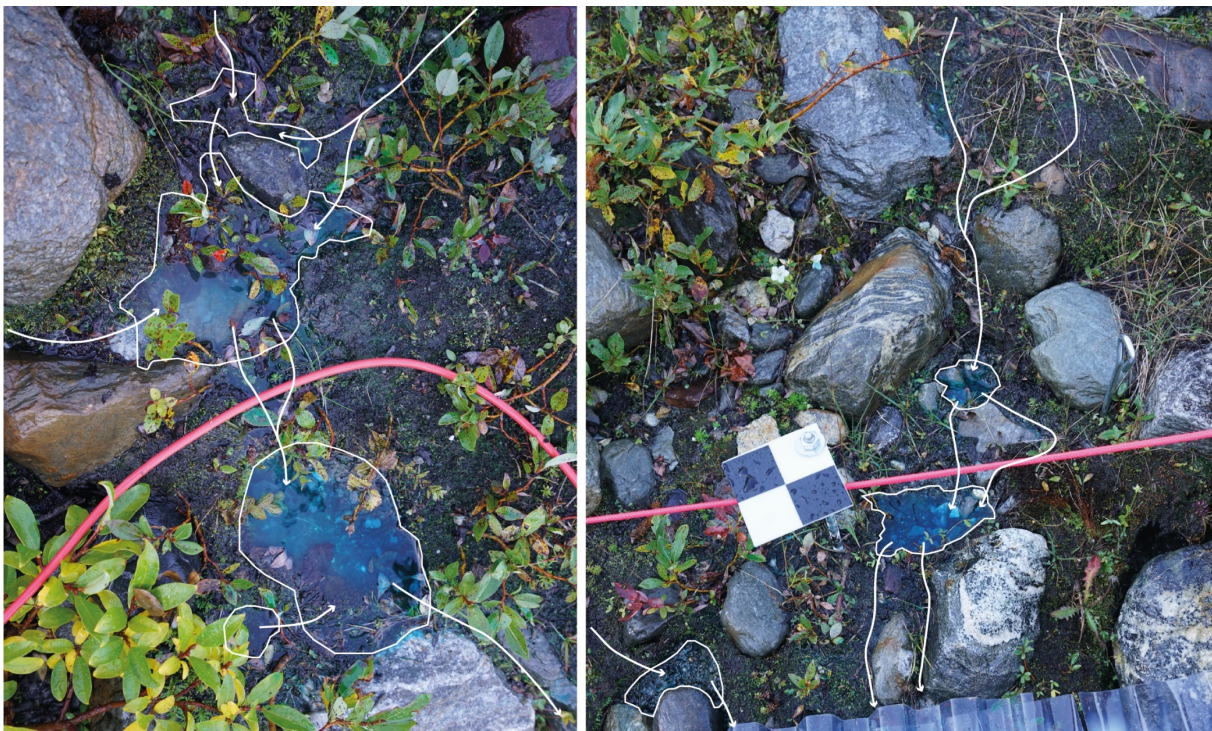


Figure 7.3 Two examples of surface hydrological connectivity, visualized by the addition of brilliant blue tracer dye to the surface runoff, in the lower part of the 1990s right plot. The white circles mark water filled depressions (ponding), which drain when filled and connect with other parts of the area via overland flow (white arrows).

8 Conclusions

This study on experimental plots in the Swiss Alps suggests that the use of fluorescent sand to determine surface connectivity and sediment transport distances is a promising approach. The introduced setup allowed for the detection of the fluorescent sand distribution before and after rainfall simulations with an estimated accuracy of about 1 cm. It was possible to determine the flow patterns based on the sediment distribution on the plot surface. Where surface runoff dominated, the distribution of the transported sand matched the microtopography and the Digital Terrain Model (DTM) based flow accumulation, as well as the observed surface flow (visualized with brilliant blue dye tracer). This strongly suggests that sediment transport depends mainly on the surface hydrology and, thus, surface hydrological connectivity and sediment (meaning that surface hydrological connectivity and sediment connectivity are very similar). However, where erosion was dominated by rain splash only sediment connectivity could be assessed. The dominant erosion type was rain splash for the vegetated plots (3k, 1860 left, 1860 right) and surface runoff for the rocky surfaces on the younger moraine (1990s left, middle, right).

The distances of the sand movement allowed a direct comparison of the experimental plots in terms of possible maximum sediment transport rates (which were assumed to be related to erosion rates). A higher rainfall intensity led to higher sediment transport. Transport of the fluorescent sand was also affected by vegetation cover and the number of plant species, and to a lesser degree by slope angle and surface roughness. Vegetation cover and the number of plant species affected sediment transport negatively for all experiments. Local surface runoff affected the transport of the sand during the experiment more than surface runoff measured at the plot lower boundary, suggesting frequent re-infiltration of surface runoff and highlighted the importance of surface connectivity. It also shows that the sediment load (below the plot) does not fully reflect sediment transport on the plot surface.

In the following the research questions are answered:

(1) Is fluorescent quartz sand useful for tracing water and sediment movement?

- Yes, it is. Both sediment movement and water flow could be determined based on the photos of the sand. On sites with low vegetation cover, sediment transport is assumed to reflect surface water movement. In highly vegetated areas, though, sediment movement did not represent water flow.

(2.1) Do rainfall intensity, surface runoff and site characteristics (vegetation cover, number of plant species, slope angle, surface roughness, saturated hydraulic conductivity) affect sediment transport on hillslopes at plot scale?

- Yes, they do. However not all site characteristics were significantly correlated to sediment transport (see Table 6).
- Rainfall intensity had a strong influence on sediment transport. Local surface runoff was more important than surface runoff measured at the lower plot boundary.
- Of all studied site characteristics, vegetation cover and the number of plant species affected sediment transport the most.
- To a lesser degree also slope angle and surface roughness influenced sediment transport.

(2.2) And if so, how do they affect sediment transport?

- A higher rainfall intensity leads to more and further sediment transport. More observed local surface runoff also resulted in further sediment transport.
- Mover vegetation cover or a higher number of plant species reduces the sediment transport.
- The effect of the influence of slope angle and surface roughness was unclear (Table 6).

Table 6 Summary of the effects of the factors studied in the thesis on sediment transport. Note that the locally occurring surface runoff was only observed and not measured. Thus no statistical tests could be made for that factor.

variable	influence on sediment transport	direction of influence on sediment transport
rainfall intensity	yes	increase
surface runoff (plot outflow)	no	-
surface runoff (locally)	yes	increase
vegetation cover	yes	decrease
number of plant species	yes	decrease
slope angle	maybe	unclear
surface roughness	maybe	unclear
saturated hydraulic conductivity	no	-

9 Recommendation for further research & improvements

For further research on the topic of surface hydrological connectivity and sediment transport several recommendations for improvements of the used method are given. These include (i) a new and easily applicable system to improve geometric correction of images, (ii) ways to avoid the shadowing effect, (iii) recommendations considering sand line placements as well as (iv) recommendations for the sand and sand color.

- (i) The “reference areas” instead of reference points led to uncertainties within the geometric correction (described in chapter 7.1.3). Instead of the fluorescent chain around the plot, it is recommended to place reference points at regular intervals (e.g. 0.5 m) around the plot. The reference points should consist of a long and thin metal rod, which can be pushed far into the ground to remain stable for the duration of all experiments. On top of the rods a thin fluorescent cross hair should be placed (preferably on a white background) to mark a unique location. On pictures from a high pixel resolution camera, the intersect of the cross hair lines will represent only a very small area, which will improve the precision when selecting the reference points for the geometric correction. The uncertainty could then be improved from centimeters to millimeters or even smaller (depending on the plot size and the pixel resolution of the camera), as it was obtained by Hardy *et al.* (2017). The fluorescent rope, which was stretched horizontally over the plots, should not be used in further studies as they cover the sand particles below the rope.
- (ii) To avoid or minimize the shadowing effect (blocked views of the sand by large rocks), two alternatives are suggested. The first and more simple option would be the extension of the camera tower to five or six meters. However, this impedes the manual operation of the camera, which is needed for the orientation and adjustment of the focal point. Better results might be achieved by placing the camera directly above the plot. Using a metal construction (such as seen in Figure 9.1), the camera-lens can be located perpendicular to the slope angle ($\lambda = 90^\circ$), allowing an areal perspective (nadir view). This was already done during the tests before the field season 2018 at the University of Zurich (Figure 9.1), but proved to be difficult to implement and time consuming in the field.
- (iii) As already suggested in chapter 7.1.1 the three sand lines could be placed in the upper half of the plot so that less (or no) sand moves off the plot. In addition, if the goal was to extract transport distances only, the three sand lines should be placed closer together in order to represent the movement of the sand within the same areas. If the goal is the

detection of surface hydrological connectivity only, multiple sand lines could be placed on the plot surface at different locations.

- (iv) The choice of sand colors could be improved. Since the blue and green sand colors were too close in terms of the hue, a darker blue would be the right choice. However, the quality of the used sand particles was not satisfying for the blue color and, thus, different sand particles could be used. Patrarc Ltd offers quartz based tracer material, in the colors red and green (Partrac Ltd, 2013). The advantage compared to the sand of Noxton™ is the known emitted wavelength of the sand, which would also allow the use of filters in front of the camera lens. This sand is available in different grain sizes and was already successfully used for soil erosion studies (e.g. by Hardy *et al.*, 2019). However, the sand particles of Patrarc Ltd cannot be detected without UV-light which increases uncertainties (see chapter 7.1.2) and should, thus, not be used on rough surfaces. On rough surfaces, the use of the fluorescent glow in the dark sand, used in this thesis, is still strongly recommended.

Applying the suggested improvements in future research will lead to better results. Then the use of fluorescent sand may be an innovative and reproducible new method to study and quantify surface hydrological connectivity and/or sediment transport. I, therefore, encourage researchers to use the fluorescent sand method in their erosion studies.

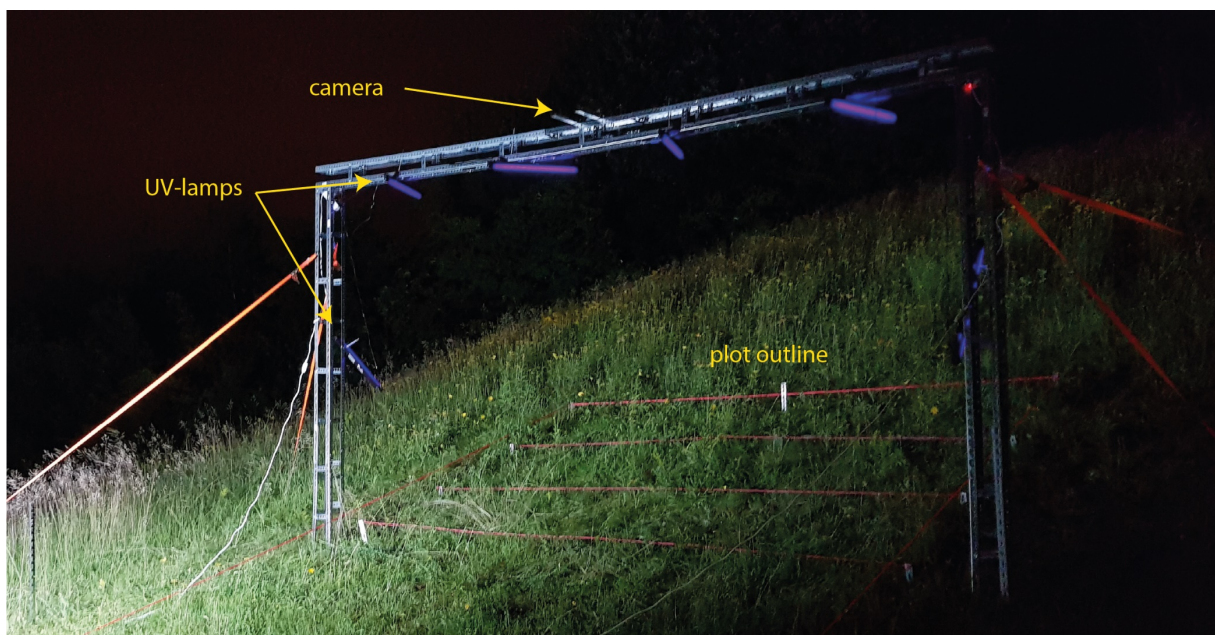


Figure 9.1 Alternative setup for the camera and the UV-lamps to capture the fluorescent sand, created during the field work preparation in June 2018 at University of Zurich. The position of the camera allows the lens to point perpendicular to plot surface ($\lambda = 90^\circ$).

Acknowledgements

This thesis was funded by the Swiss National Science Foundation (SNSF), the Deutsche Forschungsgemeinschaft (DFG) and University of Zurich. Many thanks for their support.

First, I would like to thank my supervisors Fabian Maier and Dr. Ilja van Meerveld. They supported me during the preparation for this thesis, answered questions in the field and were always open for discussions considering the evaluation process or the data.

Secondly, I would like to thank everyone that provided data or calculations for this master thesis: Fabian Maier (DTM based flow accumulation, K_{sat} , surface runoff ratio, sediment load), Konrad Greinwald (vegetation cover, number of plant species), Alessandra Musso (moraine age determination (1860 AD), soil samples and grain size distribution of the topsoils), Dr. Ilja van Meerveld and Prof. Dr. Markus Weiler (calculation of typical rainfall intensities of Sustenpass, based on return periods). Own data collection of all used variables would not have been possible.

I would also like to thank Hannes Leistert, Marc Vis and Bastian Buman. Hannes Leistert and Marc Vis converted the old IDL code to Python. Additionally, Marc Vis and Bastian Buman supported me with the creation of the new Python code for the sand extraction.

Finally, I would like to acknowledge all people that assisted in the field for the execution of the experiments and especially when taking the fluorescent sand photographs, where at least five people were needed. Further thanks to everyone assisting in the digitization process of the microtopography data (listed in alphabetical order):

Martin Binder, Theresa Binder, Gwendolyn Dasser, Jonas Freymüller, Konrad Greinwald, Markus Greinwald, Anne Hartmann, Julia Herr, Rico Hübscher, Moritz Lesche, Anja zur Loye, Jasmin Lustenberger, Fabian Maier, Verena Maier, Franziska Röpke, Ekaterina Semenova, Joseph Wetzel

Literature

- Ali GA, Roy AG. 2010. Shopping for hydrologically representative connectivity metrics in a humid temperate forested catchment. *Water Resources Research* **46** (12): 1–24 DOI: 10.1029/2010WR009442
- Allen DC, Cardinale BJ, Wynn-Thompson T. 2016. Plant biodiversity effects in reducing fluvial erosion are limited to low species richness. *Ecology* **97** (1): 17–24 DOI: 10.1890/15-0800.1
- Ameli AA, Creed IF. 2017. Quantifying hydrologic connectivity of wetlands to surface water systems. *Hydrology and Earth System Sciences* **21** (3): 1791–1808 DOI: 10.5194/hess-21-1791-2017
- Anache JAA, Flanagan DC, Srivastava A, Wendland EC. 2018. Land use and climate change impacts on runoff and soil erosion at the hillslope scale in the Brazilian Cerrado. *Science of The Total Environment* **622–623**: 140–151 DOI: 10.1016/J.SCITOTENV.2017.11.257
- Appels WM, Bogaart PW, van der Zee SEATM. 2011. Influence of spatial variations of microtopography and infiltration on surface runoff and field scale hydrological connectivity. *Advances in Water Resources* **34** (2): 303–313 DOI: 10.1016/J.ADVWATRES.2010.12.003
- Ares MG, Bongiorno F, Holzman M, Chagas C, Varni M, Entraigas I. 2016. Water erosion and connectivity analysis during a year with high precipitations in a watershed of Argentina. *Hydrology Research* **47** (6): 1239–1252 DOI: 10.2166/nh.2016.179
- Arnáez J, Larrea V, Ortigosa L. 2004. Surface runoff and soil erosion on unpaved forest roads from rainfall simulation tests in northeastern Spain. *CATENA* **57** (1): 1–14 DOI: 10.1016/J.CATENA.2003.09.002
- Badr AA, Lotfy MF. 1999. Tracing Beach Sand Movement Using Fluorescent Quartz along the Nile Delta Promontories, Egypt. *Journal of Coastal Research* **15**: 261–265 DOI: 10.2307/4298931
- Baird EJ. 2008. Controls on sediment generation from forest roads in a Pacific Maritime watershed. Simon Fraser University. Available at: <http://summit.sfu.ca/item/11687> [Accessed 29 April 2019]
- Barneveld RJ, Seeger M, Maalen-Johansen I. 2013. Assessment of terrestrial laser scanning technology for obtaining high-resolution DEMs of soils. *Earth Surface Processes and Landforms* **38** (1): 90–94 DOI: 10.1002/esp.3344
- Battany MC, Grismer ME. 2000. Rainfall runoff and erosion in Napa Valley vineyards: effects of slope, cover and surface roughness. *Hydrological Processes* **14** (7): 1289–1304 DOI: 10.1002/(SICI)1099-1085(200005)14:7<1289::AID-HYP43>3.0.CO;2-R
- Berendse F, van Ruijven J, Jongejans E, Keesstra S. 2015. Loss of Plant Species Diversity Reduces Soil Erosion Resistance. *Ecosystems* **18** (5): 881–888 DOI: 10.1007/s10021-015-9869-6
- Bertuzzi P, Rauws G, Courault D. 1990. Testing roughness indices to estimate soil surface
-

- roughness changes due to simulated rainfall. *Soil and Tillage Research* **17** (1–2): 87–99 DOI: 10.1016/0167-1987(90)90008-2
- Betson RP. 1964. What is watershed runoff? *Journal of Geophysical Research* **69** (8): 1541–1552 DOI: 10.1029/JZ069i008p01541
- Beven K. 2018. A Century of Denial: Preferential and Nonequilibrium Water Flow in Soils, 1864–1984. *Vadose Zone Journal* **17** (1): 1–17 DOI: 10.2136/vzj2018.08.0153
- Beven KJ. 2012. *Rainfall-runoff modelling: the primer*. Wiley-Blackwell. DOI: 10.1002/9781119951001
- Bilotta GS, Brazier RE. 2008. Understanding the influence of suspended solids on water quality and aquatic biota. *Water Research* **42** (12): 2849–2861 DOI: 10.1016/J.WATRES.2008.03.018
- Blume T, van Meerveld HJL. 2015. From hillslope to stream: methods to investigate subsurface connectivity. *Wiley Interdisciplinary Reviews: Water* **2** (3): 177–198 DOI: 10.1002/wat2.1071
- Bodhinayake W, Si BC, Noborio K. 2004. Determination of Hydraulic Properties in Sloping Landscapes from Tension and Double-Ring Infiltrimeters. *Vadose Zone Journal* **3** (3): 964–970 DOI: 10.2136/vzj2004.0964
- Bracken LJ, Croke J. 2007. The concept of hydrological connectivity and its contribution to understanding runoff-dominated geomorphic systems. *Hydrological Processes* **21** (13): 1749–1763 DOI: 10.1002/hyp.6313
- Bracken LJ, Turnbull L, Wainwright J, Bogaart P. 2015. Sediment connectivity: a framework for understanding sediment transfer at multiple scales. *Earth Surface Processes and Landforms* **40** (2): 177–188 DOI: 10.1002/ESP.3635
- Bryan RB. 1979. The influence of slope angle on soil entrainment by sheetwash and rainsplash. *Earth Surface Processes* **4** (1): 43–58 DOI: 10.1002/esp.3290040105
- Bryan RB. 2000. Soil erodibility and processes of water erosion on hillslope. *Geomorphology* **32** (3–4): 385–415 DOI: 10.1016/S0169-555X(99)00105-1
- Butzen V, Seeger M, Wirtz S, Huemann M, Mueller C, Casper M, Ries JB. 2014. Quantification of Hortonian overland flow generation and soil erosion in a Central European low mountain range using rainfall experiments. *CATENA* **113**: 202–212 DOI: 10.1016/J.CATENA.2013.07.008
- Cantón Y, Solé-Benet A, de Vente J, Boix-Fayos C, Calvo-Cases A, Asensio C, Puigdefábregas J. 2011. A review of runoff generation and soil erosion across scales in semiarid south-eastern Spain. *Journal of Arid Environments* **75** (12): 1254–1261 DOI: 10.1016/J.JARIDENV.2011.03.004
- Capra A. 2013. Ephemeral gully and gully erosion in cultivated land: A review. In *Drainage Basins and Catchment Management: Classification, Modelling and Environmental Assessment* 109–141.

-
- Cavalli M, Trevisani S, Comiti F, Marchi L. 2013. Geomorphometric assessment of spatial sediment connectivity in small Alpine catchments. *Geomorphology* **188**: 31–41 DOI: 10.1016/J.GEOMORPH.2012.05.007
- Cerdà A, García-Fayos P. 1997. The influence of slope angle on sediment, water and seed losses on badland landscapes. *Geomorphology* **18** (2): 77–90 DOI: 10.1016/S0169-555X(96)00019-0
- Chu X, Yang J, Chi Y, Zhang J. 2013. Dynamic puddle delineation and modeling of puddle-to-puddle filling-spilling-merging-splitting overland flow processes. *Water Resources Research* **49** (6): 3825–3829 DOI: 10.1002/wrcr.20286
- Coveney S, Stewart Fotheringham A. 2011. Terrestrial laser scan error in the presence of dense ground vegetation. *The Photogrammetric Record* **26** (135): 307–324 DOI: 10.1111/j.1477-9730.2011.00647.x
- Currence HD, Lovely WG. 1970. The Analysis of Soil Surface Roughness. *Transactions of the ASAE* **13** (6): 710–714 DOI: <https://doi.org/10.13031/2013.38702>
- D. Eigel J, D. Moore I. 1983. A Simplified Technique for Measuring Raindrop Size and Distribution. *Transactions of the ASAE* **26** (4): 1079–1084 DOI: <https://doi.org/10.13031/2013.34080>
- Defersha MB, Melesse AM. 2012. Effect of rainfall intensity, slope and antecedent moisture content on sediment concentration and sediment enrichment ratio. *CATENA* **90**: 47–52 DOI: 10.1016/J.CATENA.2011.11.002
- Dierschke H. 1994. *Pflanzensoziologie: Grundlagen und Methoden (UTB)*. Ulmer, Stuttgart.
- Dominati E, Patterson M, Mackay A. 2010. A framework for classifying and quantifying the natural capital and ecosystem services of soils. *Ecological Economics* **69** (9): 1858–1868 DOI: 10.1016/J.ECOLECON.2010.05.002
- Dunne T, Black RD. 1970. An Experimental Investigation of Runoff Production in Permeable Soils. *Water Resources Research* **6** (2): 478–490 DOI: 10.1029/WR006i002p00478
- Evans R. 1980. Mechanics of water erosion and their spatial and temporal controls: an empirical viewpoint. In *Soil Erosion*, Kirkby MJ, , Morgan RPC (eds).Wiley: Chichester; 109–128.
- FAO. 2015. Status of the World's Soil Resources. Main Report Available at: <http://www.fao.org/3/a-i5199e.pdf>
- Federal Office for the Environment FOEN. 2018. Wasser: Internationales Available at: <https://www.bafu.admin.ch/bafu/de/home/themen/wasser/fachinformationen/internationaler-gewaesserschutz.html> [Accessed 29 April 2019]
- Federal Office of Topography swisstopo. 2019a. Areal Photo Sustenpass Available at: https://map.geo.admin.ch/?lang=de&topic=ech&bgLayer=ch.swisstopo.swissimage&layers=ch.swisstopo.zeitreihen,ch.bfs.gebaeude_wohnungs_register,ch.bav.haltestellen-oev,ch.swisstopo.swisstlm3d-wanderwege&layers_visibility=false,false,false,false&layers_timestamp=18641231,,&E=26
-

- 76134.85&N=1175289.54&zoom=9 [Accessed 29 April 2019]
- Federal Office of Topography swisstopo. 2019b. Aareal Photographs Available at: https://map.geo.admin.ch/?lang=de&topic=ech&bgLayer=ch.swisstopo.pixelkarte-farbe&layers=ch.swisstopo.lubis-luftbilder_schwarzweiss,ch.swisstopo.lubis-luftbilder_farbe,ch.swisstopo.lubis-luftbilder_schraegaufnahmen,ch.swisstopo.lubis-luftbilder_infrarot&l [Accessed 29 April 2019]
- Fullen MA. 1991. A comparison of runoff and erosion rates on bare and grassed loamy sand soils. *Soil Use and Management* **7** (3): 136–138 DOI: 10.1111/j.1475-2743.1991.tb00864.x
- Golden HE, Creed IF, Ali G, Basu NB, Neff BP, Rains MC, McLaughlin DL, Alexander LC, Ameli AA, Christensen JR, et al. 2017. Integrating geographically isolated wetlands into land management decisions. *Frontiers in Ecology and the Environment* **15** (6): 319–327 DOI: 10.1002/fee.1504
- Guzmán G, Laguna A, Cañasveras JC, Boulal H, Barrón V, Gómez-Macpherson H, Giráldez JV, Gómez JA. 2015. Study of sediment movement in an irrigated maize–cotton system combining rainfall simulations, sediment tracers and soil erosion models. *Journal of Hydrology* **524**: 227–242 DOI: 10.1016/J.JHYDROL.2015.02.033
- HADES. 2019. Hydrological Atlas of Switzerland Available at: <https://hydrologicalatlas.ch/?language=switch> [Accessed 29 April 2019]
- Hardy RA, James MR, Pates JM, Quinton JN. 2017. Using real time particle tracking to understand soil particle movements during rainfall events. *CATENA* **150**: 32–38 DOI: 10.1016/J.CATENA.2016.11.005
- Hardy RA, Pates JM, Quinton JN, Coogan MP. 2016. A novel fluorescent tracer for real-time tracing of clay transport over soil surfaces. *CATENA* **141**: 39–45 DOI: 10.1016/J.CATENA.2016.02.011
- Hardy RA, Quinton JN, James MR, Fiener P, Pates JM. 2019. High precision tracing of soil and sediment movement using fluorescent tracers at hillslope scale. *Earth Surface Processes and Landforms* **44** (5): 1091–1099 DOI: 10.1002/esp.4557
- Heikkinen O, Fogelberg P. 1980. Bodenentwicklung im Hochgebirge : ein Beispiel vom Vorfeld des Steingletschers in der Schweiz. *Geographica Helvetica* **35** (3): 107–112 DOI: 10.5194/gh-35-107-1980
- Hendriks MR. 2010. *Introduction to Physical Hydrology*. Oxford University Press.
- Horton RE. 1933. The Rôle of infiltration in the hydrologic cycle. *Transactions, American Geophysical Union* **14** (1): 446–460 DOI: 10.1029/TR014i001p00446
- Hou J, Wang H, Fu B, Zhu L, Wang Y, Li Z. 2016. Effects of plant diversity on soil erosion for different vegetation patterns. *CATENA* **147**: 632–637 DOI: 10.1016/J.CATENA.2016.08.019
- IUSS Working Group WRB. 2015. World reference base for soil resources 2014, Update 2015

-
- International soil classification system for naming soils and creating legends for soil maps. *World Soil Resources Reports* **106**: 1–203
- Johnson BG, Layzell AL, Eppes MC. 2015. Chronosequence development and soil variability from a variety of sub-alpine, post-glacial landforms and deposits in the southeastern San Juan Mountains of Colorado. *CATENA* **127**: 222–239 DOI: 10.1016/J.CATENA.2014.12.026
- El Kateb H, Zhang H, Zhang P, Mosandl R. 2013. Soil erosion and surface runoff on different vegetation covers and slope gradients: A field experiment in Southern Shaanxi Province, China. *CATENA* **105**: 1–10 DOI: 10.1016/J.CATENA.2012.12.012
- Kato S, Okabe T, Aoki Y, Kamohara S. 2014. Field measurement of sand movement on river-mouth tidal flat using color sand tracing. *Coastal Engineering Proceedings* **1** (34): 1–9 DOI: 10.9753/icce.v34.sediment.61
- Khan M, Gong Y, Hu T, Lal R, Zheng J, Justine M, Azhar M, Che M, Zhang H, Khan MN, et al. 2016. Effect of Slope, Rainfall Intensity and Mulch on Erosion and Infiltration under Simulated Rain on Purple Soil of South-Western Sichuan Province, China. *Water* **8** (11): 1–528 DOI: 10.3390/w8110528
- King L. 1974. Studien zur postglazialen Gletscher- u. Vegetationsgeschichte d. Sustenpaßgebietes.
- Klein M, Zviely D, Kit E, Shteinman B. 2007. Sediment Transport along the Coast of Israel: Examination of Fluorescent Sand Tracers. *Journal of Coastal Research* **23** (6): 1462–1470 DOI: 10.2112/05-0488.1
- Koulouri M, Giourga C. 2007. Land abandonment and slope gradient as key factors of soil erosion in Mediterranean terraced lands. *CATENA* **69** (3): 274–281 DOI: 10.1016/J.CATENA.2006.07.001
- Leatherman SP. 1987. Field Measurement of Microtopography. *Journal of Coastal Research* **3**: 233–235 DOI: 10.2307/4297283
- Lee J-H, Heo J-H. 2011. Evaluation of estimation methods for rainfall erosivity based on annual precipitation in Korea. *Journal of Hydrology* **409** (1–2): 30–48 DOI: 10.1016/J.JHYDROL.2011.07.031
- Lesschen JP, Schoolr JM, Cammeraat LH. 2009. Modelling runoff and erosion for a semi-arid catchment using a multi-scale approach based on hydrological connectivity. *Geomorphology* **109** (3–4): 174–183 DOI: 10.1016/J.GEOMORPH.2009.02.030
- Li D (ed.). 2008. HSV Color Space. In *Encyclopedia of Microfluidics and Nanofluidics* Springer US: Boston, MA; 791–803. DOI: 10.1007/978-0-387-48998-8_656
- Lillesand TM, Kiefer RW, Chipman JW. 2015. *Remote sensing and image interpretation, 7th Edition*. Hoboken, NJ: John Wiley & Sons.
- Liu J, Engel BA, Wang Y, Wu Y, Zhang Z, Zhang M. 2019. Runoff Response to Soil Moisture and Micro-topographic Structure on the Plot Scale. *Scientific Reports* **9** (2532): 1–13 DOI:
-

10.1038/s41598-019-39409-6

- Liu QQ, Singh VP. 2004. Effect of Microtopography, Slope Length and Gradient, and Vegetative Cover on Overland Flow through Simulation. *Journal of Hydrologic Engineering* **9** (5): 375–382 DOI: 10.1061/(ASCE)1084-0699(2004)9:5(375)
- Lohse KA, Dietrich WE. 2005. Contrasting effects of soil development on hydrological properties and flow paths. *Water Resources Research* **41** (12): 1–17 DOI: 10.1029/2004WR003403
- Long EJ, Hargrave GK, Cooper JR, Kitchener BGB, Parsons AJ, Hewett CJM, Wainwright J. 2014. Experimental investigation into the impact of a liquid droplet onto a granular bed using three-dimensional, time-resolved, particle tracking. *Physical Review E* **89** (3): 1–14 DOI: 10.1103/PhysRevE.89.032201
- Marques MJ, Jiménez L, Pérez-Rodríguez R. 2007. Effect of vegetal cover on runoff and soil erosion under light intensity events. Rainfall simulation over USLE plots. *Science of The Total Environment* **378** (1–2): 161–165 DOI: 10.1016/J.SCITOTENV.2007.01.043
- Martínez-Murillo JF, Nadal-Romero E, Regüés D, Cerdà A, Poesen J. 2013. Soil erosion and hydrology of the western Mediterranean badlands throughout rainfall simulation experiments: A review. *CATENA* **106**: 101–112 DOI: 10.1016/J.CATENA.2012.06.001
- Mather P, Tso B, Tso B. 2016. *Classification Methods for Remotely Sensed Data*. CRC Press. DOI: 10.1201/9781420090741
- Mayor ÁG, Bautista S, Small EE, Dixon M, Bellot J. 2008. Measurement of the connectivity of runoff source areas as determined by vegetation pattern and topography: A tool for assessing potential water and soil losses in drylands. *Water Resources Research* **44** (10): 1–13 DOI: 10.1029/2007WR006367
- Meerkerk AL, van Wesemael B, Bellin N. 2009. Application of connectivity theory to model the impact of terrace failure on runoff in semi-arid catchments. *Hydrological Processes* **23** (19): 2792–2803 DOI: 10.1002/hyp.7376
- van Meerveld HJ, Baird EJ, Floyd WC. 2014. Controls on sediment production from an unpaved resource road in a Pacific maritime watershed. *Water Resources Research* **50** (6): 4803–4820 DOI: 10.1002/2013WR014605
- van Meerveld HJ, Egli M, Weiler M, Blume T. 2018. HILLSCAPE Project Homepage Available at: <http://hillscape.ch/> [Accessed 29 April 2019]
- MeteoSwiss. 2016a. Climate normals Meiringen Available at: <https://www.meteoswiss.admin.ch/home/climate/swiss-climate-in-detail/climate-normals/climate-diagrams-and-normals--per-station.html?region=Table>
- MeteoSwiss. 2016b. Climate normals Grimsel Hospiz Available at: <https://www.meteoswiss.admin.ch/home/climate/swiss-climate-in-detail/climate-normals/climate-diagrams-and-normals--per-station.html?region=Table>
-

-
- Michaelides K, Chappell A. 2009. Connectivity as a concept for characterising hydrological behaviour. *Hydrological Processes* **23** (3): 517–522 DOI: 10.1002/hyp.7214
- Musso A, Lamorski K, Slawinski C, Geitner C, Hunt A, Greinwald K, Egli M. in review. Evolution of soil pores and their characteristics in a siliceous and calcareous proglacial area. *CATENA*
- Nadal-Romero E, Petrlic K, Verachtert E, Bochet E, Poesen J. 2014. Effects of slope angle and aspect on plant cover and species richness in a humid Mediterranean badland. *Earth Surface Processes and Landforms* **39** (13): 1705–1716 DOI: 10.1002/esp.3549
- Nearing MA, Pruski FF, O'Neal MR. 2004. Expected climate change impacts on soil erosion rates: A review. *Journal of soil and water conservation* **59** (1): 43–50 Available at: <https://pubag.nal.usda.gov/catalog/6819> [Accessed 29 April 2019]
- Noxton. 2019. Glow in the Dark Decorative Sand Available at: http://noxton.com/index_en.html [Accessed 29 April 2019]
- Parsons AJ, Wainwright J, Powell DM, Kaduk J, Brazier RE. 2004. A conceptual model for determining soil erosion by water. *Earth Surface Processes and Landforms* **29** (10): 1293–1302 DOI: 10.1002/esp.1096
- Partrac Ltd. 2013. Demonstration of fluorescent magnetic particles for linking sources to sediments at DoD sites - Partrac Tracer Material 'White Paper'. Glasgow. Available at: <http://www.partrac.com/services/particle-tracking/>
- Paz-Ferreiro J, Bertol I, Vidal Vázquez E. 2008. Quantification of tillage, plant cover, and cumulative rainfall effects on soil surface microrelief by statistical, geostatistical and fractal indices. *Nonlinear Processes in Geophysics* **15** (4): 575–590 DOI: 10.5194/npg-15-575-2008
- Peñuela A, Javaux M, Bièlders CL. 2015. How do slope and surface roughness affect plot-scale overland flow connectivity? *Journal of Hydrology* **528**: 192–205 DOI: 10.1016/J.JHYDROL.2015.06.031
- Pietravalle S, van den Bosch F, Welham S., Parker S., Lovell D. 2001. Modelling of rain splash trajectories and prediction of rain splash height. *Agricultural and Forest Meteorology* **109** (3): 171–185 DOI: 10.1016/S0168-1923(01)00267-2
- Poesen J. 2018. Soil erosion in the Anthropocene: Research needs. *Earth Surface Processes and Landforms* **43** (1): 64–84 DOI: 10.1002/esp.4250
- Pohl M, Alig D, Körner C, Rixen C. 2009. Higher plant diversity enhances soil stability in disturbed alpine ecosystems. *Plant and Soil* **324** (1–2): 91–102 DOI: 10.1007/s11104-009-9906-3
- Prosdocimi M, Burguet M, Di Prima S, Sofia G, Terol E, Rodrigo Comino J, Cerdà A, Tarolli P. 2017. Rainfall simulation and Structure-from-Motion photogrammetry for the analysis of soil water erosion in Mediterranean vineyards. *Science of The Total Environment* **574**: 204–215 DOI: 10.1016/J.SCITOTENV.2016.09.036
- Qing-quan L, Li C, Jia-chun L. 2001. Influences of slope gradient on soil erosion. *Applied*
-

-
- Mathematics and Mechanics* **22** (5): 510–519 DOI: 10.1007/BF02437740
- Raclot D, Le Bissonnais Y, Annabi M, Sabir M, Smetanova A. 2018. Main Issues for Preserving Mediterranean Soil Resources From Water Erosion Under Global Change. *Land Degradation & Development* **29** (3): 789–799 DOI: 10.1002/ldr.2774
- Rahmat RF, Chairunnisa T, Gunawan D, Sitompul OS. 2016. Skin color segmentation using multi-color space threshold. In *2016 3rd International Conference on Computer and Information Sciences (ICCOINS)* 391–396. DOI: 10.1109/ICCOINS.2016.7783247
- Reaney SM, Bracken LJ, Kirkby MJ. 2014. The importance of surface controls on overland flow connectivity in semi-arid environments: results from a numerical experimental approach. *Hydrological Processes* **28** (4): 2116–2128 DOI: 10.1002/hyp.9769
- Rey F, Ballais J-L, Marre A, Rovéra G. 2004. Role of vegetation in protection against surface hydric erosion. *Comptes Rendus Geoscience* **336** (11): 991–998 DOI: 10.1016/J.CRTE.2004.03.012
- Rodrigo Comino J, Iserloh T, Lassu T, Cerdà A, Keestra SD, Prosdocimi M, Brings C, Marzen M, Ramos MC, Senciales JM, et al. 2016. Quantitative comparison of initial soil erosion processes and runoff generation in Spanish and German vineyards. *Science of The Total Environment* **565**: 1165–1174 DOI: 10.1016/j.scitotenv.2016.05.163
- Römkens MJ, Helming K, Prasad S. 2002. Soil erosion under different rainfall intensities, surface roughness, and soil water regimes. *CATENA* **46** (2–3): 103–123 DOI: 10.1016/S0341-8162(01)00161-8
- Sandercock PJ, Hooke JM. 2011. Vegetation effects on sediment connectivity and processes in an ephemeral channel in SE Spain. *Journal of Arid Environments* **75** (3): 239–254 DOI: 10.1016/J.JARIDENV.2010.10.005
- van Schaik NLMB. 2009. Spatial variability of infiltration patterns related to site characteristics in a semi-arid watershed. *CATENA* **78** (1): 36–47 DOI: 10.1016/J.CATENA.2009.02.017
- Scherrer S, Naef F, Faeh AO, Cordery I. 2007. Formation of runoff at the hillslope scale during intense precipitation. *Hydrology and Earth System Sciences* **11** (2): 907–922 DOI: 10.5194/hess-11-907-2007
- Schimmelpfennig I, Schaefer JM, Akçar N, Koffman T, Ivy-Ochs S, Schwartz R, Finkel RC, Zimmerman S, Schlüchter C. 2014. A chronology of Holocene and Little Ice Age glacier culminations of the Steingletscher, Central Alps, Switzerland, based on high-sensitivity beryllium-10 moraine dating. *Earth and Planetary Science Letters* **393**: 220–230 DOI: 10.1016/J.EPSL.2014.02.046
- Schneider P, Pool S, Strouhal L, Seibert J. 2014. True colors - experimental identification of hydrological processes at a hillslope prone to slide. *Hydrology and Earth System Sciences* **18** (2): 875–892 DOI: 10.5194/hess-18-875-2014
- Smith A. 1978. Color Gamut Transform Pairs. In *ACM Siggraph Computer Graphics* 12–19. DOI:
-

10.1145/800248.807361

- Stewart RD, Liu Z, Rupp DE, Higgins CW, Selker JS. 2015. A new instrument to measure plot-scale runoff. *Geoscientific Instrumentation, Methods and Data Systems* **4** (1): 57–64 DOI: 10.5194/gi-4-57-2015
- Stieglitz M, Shaman J, McNamara J, Engel V, Shanley J, Kling GW. 2003. An approach to understanding hydrologic connectivity on the hillslope and the implications for nutrient transport. *Global Biogeochemical Cycles* **17** (4): 1–15 DOI: 10.1029/2003GB002041
- Tarboton DG. 1997. A new method for the determination of flow directions and upslope areas in grid digital elevation models. *Water Resources Research* **33** (2): 309–319 DOI: 10.1029/96WR03137
- Tauro F, Grimaldi S, Petroselli A, Porfiri M. 2012a. Fluorescent particle tracers for surface flow measurements: A proof of concept in a natural stream. *Water Resources Research* **48** (6): 1–10 DOI: 10.1029/2011WR011610
- Tauro F, Grimaldi S, Petroselli A, Rulli MC, Porfiri M. 2012b. Fluorescent particle tracers in surface hydrology: a proof of concept in a semi-natural hillslope. *Hydrology and Earth System Sciences* **16** (8): 2973–2983 DOI: 10.5194/hess-16-2973-2012
- Tauro F, Petroselli A, Fiori A, Romano N, Rulli MC, Porfiri M, Palladino M, Grimaldi S. 2016. Technical Note: Monitoring streamflow generation processes at Cape Fear. *Hydrology and Earth System Sciences Discussions*: 1–25 DOI: 10.5194/hess-2016-501
- Temme AJAM, Lange K. 2014. Pro-glacial soil variability and geomorphic activity - the case of three Swiss valleys. *Earth Surface Processes and Landforms* **39** (11): 1492–1499 DOI: 10.1002/esp.3553
- Thomsen LM, Baartman JEM, Barneveld RJ, Starkloff T, Stolte J. 2015. Soil surface roughness: comparing old and new measuring methods and application in a soil erosion model. *SOIL* **1** (1): 399–410 DOI: 10.5194/soil-1-399-2015
- Tromp-van Meerveld HJ, McDonnell JJ. 2006. On the interrelations between topography, soil depth, soil moisture, transpiration rates and species distribution at the hillslope scale. *Advances in Water Resources* **29** (2): 293–310 DOI: 10.1016/j.advwatres.2005.02.016
- Usai C, Diaspro A. 2013. Fluorescence: General Aspects. In *Encyclopedia of Biophysics*, Roberts GCK (ed.). Springer Berlin Heidelberg: Berlin, Heidelberg; 826–832. DOI: 10.1007/978-3-642-16712-6_823
- Vermang J, Norton LD, Baetens JM, Huang C, Cornelis WM, Gabriels D. 2013. Quantification of Soil Surface Roughness Evolution under Simulated Rainfall. *Transactions of the ASABE* **56** (2): 505–514 DOI: 10.13031/2013.42670
- Vermang J, Norton LD, Huang C, Cornelis WM, da Silva AM, Gabriels D. 2015. Characterization of Soil Surface Roughness Effects on Runoff and Soil Erosion Rates under Simulated Rainfall.
-

-
- Soil Science Society of America Journal* **79** (3): 903–916 DOI: 10.2136/sssaj2014.08.0329
- Wei W, Chen L, Fu B, Huang Z, Wu D, Gui L. 2007. The effect of land uses and rainfall regimes on runoff and soil erosion in the semi-arid loess hilly area, China. *Journal of Hydrology* **335** (3–4): 247–258 DOI: 10.1016/J.JHYDROL.2006.11.016
- Weiler M, Flühler H. 2004. Inferring flow types from dye patterns in macroporous soils. *Geoderma* **120** (1–2): 137–153 DOI: 10.1016/J.GEODERMA.2003.08.014
- Weiler MH. 2001. Mechanisms controlling macropore flow during infiltration dye tracer experiments and simulations. ETH Zürich. DOI: 10.3929/ETHZ-A-004180115
- Wen L, Zheng F, Shen H, Bian F, Jiang Y. 2015. Rainfall intensity and inflow rate effects on hillslope soil erosion in the Mollisol region of Northeast China. *Natural Hazards* **79** (1): 381–395 DOI: 10.1007/s11069-015-1847-y
- Xu X, Zheng F, Wilson GV, Wu M. 2017. Upslope inflow, hillslope gradient and rainfall intensity impacts on ephemeral gully erosion. *Land Degradation & Development* **28** (8): 2623–2635 DOI: 10.1002/ldr.2825
- YASSO WE. 1966. Formulation and use of fluorescent tracer coatings in sediment transport studies. *Sedimentology* **6** (4): 287–301 DOI: 10.1111/j.1365-3091.1966.tb01896.x
- Young RA, Holt RF. 1968. Tracing Soil Movement with Fluorescent Glass Particles¹. *Soil Science Society of America Journal* **32** (4): 600–602 DOI: 10.2136/sssaj1968.03615995003200040050x
- Zech W, Schad P, Hintermaier-Erhard G. 2014. *Böden der Welt*. Springer Spektrum. DOI: 10.1007/978-3-642-36575-1
- Zhang B, Yang Y, Zepp H. 2004. Effect of vegetation restoration on soil and water erosion and nutrient losses of a severely eroded clayey Plinthudult in southeastern China. *CATENA* **57** (1): 77–90 DOI: 10.1016/J.CATENA.2003.07.001
- Zhang G-H, LIU G-B, WANG G-L, WANG Y-X. 2011. Effects of Vegetation Cover and Rainfall Intensity on Sediment-Bound Nutrient Loss, Size Composition and Volume Fractal Dimension of Sediment Particles. *Pedosphere* **21** (5): 676–684 DOI: 10.1016/S1002-0160(11)60170-7
- Zhou P, Luukkanen O, Tokola T, Nieminen J. 2008. Effect of vegetation cover on soil erosion in a mountainous watershed. *CATENA* **75** (3): 319–325 DOI: 10.1016/J.CATENA.2008.07.010
- Ziadat FM, Taimah AY. 2013. Effect of rainfall intensity, slope, land use and antecedent soil moisture on soil erosion in an arid environment. *Land Degradation & Development* **24** (6): 582–590 DOI: 10.1002/ldr.2239
- Zimmermann A, Schinn DS, Francke T, Elsenbeer H, Zimmermann B. 2013. Uncovering patterns of near-surface saturated hydraulic conductivity in an overland flow-controlled landscape. *Geoderma* **195–196**: 1–11 DOI: 10.1016/J.GEODERMA.2012.11.002
- Zimmermann B, Zimmermann A, Turner BL, Francke T, Elsenbeer H. 2014. Connectivity of
-

overland flow by drainage network expansion in a rain forest catchment. *Water Resources Research* **50** (2): 1457–1473 DOI: 10.1002/2012WR012660

Declaration of originality

Personal declaration: I hereby declare that the submitted thesis is the result of my own, independent work. All external sources are explicitly acknowledged in the thesis.

Place, Date

Florian R. Lustenberger

Zurich, 29.04.2019

A handwritten signature in black ink, appearing to read 'F. Lustenberger', written in a cursive style.

Appendix 1: Calculations

Calculation of the actual experimental plot area (A_{plot}) for the calculation of the surface runoff ratio (chapter 4.2.2):

The actual plot area in the field was different from the planned 4 m × 6 m because of natural variations. The actual plot area had, hence, needed to be calculated in order to provide correct results for the surface runoff ratio in equation (1). For the calculations the plot was sketched in Figure A.1.

The actual plot area (A_{plot}) was first divided into two triangles (see equation (4), where A_b = blue and A_d = green in Figure A.1):

$$A_{plot} = A_b + A_d \quad (4)$$

Within each triangle then the corresponding height (h_b for blue and h_d for green) were calculated. This is presented in equations (5) and (6).

$$h_b = \sin \beta * c \quad (5)$$

$$h_d = \sin \alpha * a \quad (6)$$

Then for both triangles the corresponding area (A_b for blue and A_d for green) could be calculated using equations (5) and (6):

$$A_b = \frac{h_b * b}{2} = \frac{\sin \beta * b * c}{2} \quad (7)$$

$$A_d = \frac{h_d * d}{2} = \frac{\sin \alpha * a * d}{2} \quad (8)$$

Combining equation (4) with equations (7) and (8) the actual plot area was calculated:

$$A_{plot} = A_b + A_d = \frac{\sin \beta * b * c}{2} + \frac{\sin \alpha * a * d}{2} \quad (9)$$

The actual plot areas are presented in Table 7. Notably no plot had the theoretical area of 24 m², and thus the actual plot areas were important for the calculations in equation (1).

Calculation of the actual heights of the microtopography profiles on the 1990s right plot for the 3-dimensional plot (Figure 6.7):

The actual height of the microtopography transects v, vi, vii and viii compared to the transects ix and x was calculated using the measured slope angles. They were available in 0.5 m steps and thus 0.5 m surface distances around each slope angle measurement ($\gamma, \delta, \varepsilon, \eta, \theta$) were created (25 cm before and after). For each of those distances (e, f, g, h, i) the slope was constant (Figure A.2). Using the laws of trigonometry, the individual heights for each surface distance (y_e, y_f, y_g, y_h, y_i) was calculated as follows:

$$y_e = \cos \gamma * e \quad (10)$$

$$y_f = \cos \delta * f \quad (11)$$

$$y_g = \cos \varepsilon * g \quad (12)$$

$$y_h = \cos \eta * h \quad (13)$$

$$y_i = \cos \theta * i \quad (14)$$

For transects ix and x no actual height had to be calculated since they were used as starting height (reference height). The actual height for transects vii and viii (h_{l2}) was calculated using equations (12), (13) and (14):

$$h_{l2} = \frac{y_i}{2} + y_h + \frac{y_g}{2} \quad (15)$$

The division of y_i and y_g by two is because only half of the surface distance, and thus also only half the individual height, was needed for the actual height (see Figure A.2b). For the transects v and vi the actual height (h_{l3}) was calculated using equations (10), (11), (12), (13) and (14):

$$h_{l3} = \frac{y_i}{2} + y_h + y_g + y_f + \frac{y_e}{2} \quad (16)$$

As before, the first and last additional distances (y_i, y_e) were divided by two.

The actual heights were added to all height readings of the corresponding microtopography transect. This was 39 cm for h_{l2} and 79 cm for h_{l3} .

Table 7 Plot border lengths a, b, c, d (see Figure A.1) in m, as measured in the field, the angles α (between a and d) and β (between b and c) in degree as well as the actual calculated plot area A_{plot} in m^2 using equation (9).

plot	a [m]	b [m]	c [m]	d [m]	α [°]	β [°]	A_{plot} [m ²]
3k	4.2	6.05	4.05	6.05	65	74	23.29
1860 left	4.1	6.1	4.1	6.1	89	90	25.01
1860 right	4.1	6	4	6.2	88	89	24.70
1990 left	4	5.7	4.2	6	87	102	23.69
1990 middle	3.6	6.1	4.1	6.2	84	92	23.60
1990 right	3.8	6.1	4.2	6.4	93	103	24.63

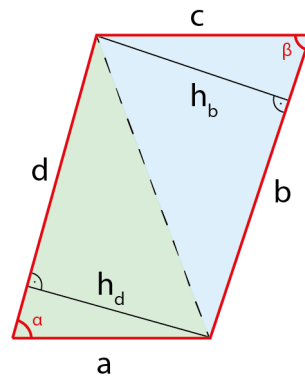


Figure A.1 Sketch of an experimental plot (red) in the field with the measured distances a, b, c and d as well as the angles α and β . The plot is divided into two triangles ($A_b = \text{blue}$ and $A_d = \text{green}$) for the calculation of the actual plot area.

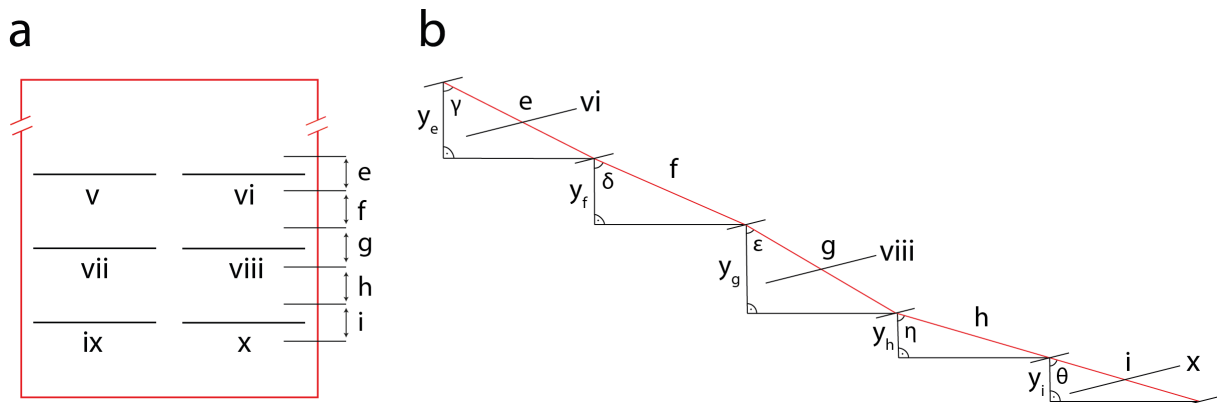


Figure A.2 Sketch of a lower experimental plot half (a), including the microtopography transects v to x . Since the slope angles were measured every 0.5 m, their values were used for the corresponding 25 cm before and after a measurement which leads to five distances (e, f, g, h, i) to which one slope angle measurement corresponds. The transects v and vi were in the middle of distance e , vii and $viii$ in the middle of distance g and ix and x in the middle of distance i . A vertical side view of the lower part of the plot (b) was created to illustrate the calculation of the actual height of microtopography lines (transect v and vi , transect vii and $viii$) above the lowest line (transect ix and x). Therefore, the heights y_e, y_f, y_g, y_h and y_i as well as the angles $\gamma, \delta, \epsilon, \eta$ and θ are presented.

Appendix 2: Correlation tables

Table 8 Pearson and Spearman rank correlations for the four sand distance measures (based on the relative cumulative travel distances: 50 %, 75 %, 90 % and maximum distance) and the values of the site characteristics (slope angle, tortuosity index TI, random roughness RR, vegetation cover, number of plant species (species richness), saturated hydraulic conductivity K_{sat}) and the first two principal components (PC1, PC2) of the PCA for the three rainfall intensities (low, mid, high). Marked in green are the significant values (significance level: $\alpha = 0.1$).

	Pearson (r)				Spearman (r _s)			
	50 %	75 %	90 %	max	50 %	75 %	90 %	max
low intensity								
slope angle	-0.742	-0.663	-0.558	-0.246	-0.543	-0.486	-0.429	-0.600
surface roughness (TI)	0.526	0.568	0.481	0.484	0.600	0.657	0.429	0.829
surface roughness (RR)	0.649	0.688	0.525	0.409	0.714	0.543	0.371	0.486
vegetation cover	-0.448	-0.587	-0.694	-0.873	-0.714	-0.886	-0.771	-0.943
species richness	0.038	-0.228	-0.355	-0.679	-0.290	-0.580	-0.493	-0.754
K_{sat}	0.163	0.325	0.469	0.700	0.143	0.429	0.314	0.657
PC1	-0.373	-0.552	-0.633	-0.832	-0.314	-0.600	-0.543	-0.771
PC2	0.652	0.575	0.399	0.140	0.543	0.371	0.257	0.429
mid intensity								
slope angle	-0.832	-0.828	-0.489	-0.132	-0.900	-0.900	-0.600	-0.700
surface roughness (TI)	0.414	0.439	0.409	0.375	0.500	0.500	0.400	0.700
surface roughness (RR)	0.702	0.723	0.615	0.443	0.300	0.300	0.200	0.500
vegetation cover	0.041	-0.014	-0.606	-0.864	-0.300	-0.300	-0.800	-0.900
species richness	0.048	-0.008	-0.674	-0.927	-0.154	-0.154	-0.718	-0.872
K_{sat}	-0.155	-0.107	0.472	0.737	0.100	0.100	0.500	0.700
PC1	-0.141	-0.194	-0.676	-0.855	-0.300	-0.300	-0.800	-0.900
PC2	0.764	0.764	0.413	0.123	0.800	0.800	0.300	0.400
high intensity								
slope angle	0.441	0.260	0.077	-0.267	0.300	0.300	0.000	-0.700
surface roughness (TI)	-0.527	-0.276	-0.119	0.533	-0.700	-0.700	-0.300	0.700
surface roughness (RR)	-0.008	0.272	0.420	0.545	0.100	0.100	0.400	0.500
vegetation cover	0.503	0.307	0.080	-0.890	0.500	0.500	-0.100	-0.900
species richness	0.182	0.016	-0.196	-0.884	0.410	0.410	-0.205	-0.872
K_{sat}	-0.617	-0.487	-0.276	0.755	-0.800	-0.800	-0.300	0.700
PC1	0.559	0.318	0.069	-0.917	0.500	0.500	-0.100	-0.900
PC2	-0.226	-0.005	0.117	0.268	0.000	0.000	0.100	0.400

Table 9 p-values of Pearson and Spearman rank correlations for the four sand distance measures (based on the relative cumulative travel distances: 50 %, 75 %, 90 % and maximum distance) and the values of the site characteristics (slope angle, tortuosity index TI, random roughness RR, vegetation cover, number of plant species (species richness), saturated hydraulic conductivity K_{sat}) and the first two principal components (PC1, PC2) of the PCA for the three rainfall intensities (low, mid, high). Marked in green are the significant values (significance level: $\alpha = 0.1$).

	p-value of Pearson				p-value of Spearman			
	50 %	75 %	90 %	max	50 %	75 %	90 %	max
low intensity								
slope angle	0.091	0.151	0.250	0.639	0.297	0.356	0.419	0.242
surface roughness (TI)	0.284	0.239	0.334	0.330	0.242	0.175	0.419	0.058
surface roughness (RR)	0.163	0.131	0.285	0.421	0.136	0.297	0.497	0.356
vegetation cover	0.373	0.221	0.126	0.023	0.136	0.033	0.103	0.017
species richness	0.943	0.665	0.490	0.138	0.577	0.228	0.321	0.084
K_{sat}	0.757	0.529	0.348	0.122	0.803	0.419	0.564	0.175
PC1	0.466	0.256	0.178	0.040	0.564	0.242	0.297	0.103
PC2	0.160	0.232	0.433	0.791	0.297	0.497	0.658	0.419
mid intensity								
slope angle	0.080	0.084	0.404	0.833	0.083	0.083	0.350	0.233
surface roughness (TI)	0.488	0.460	0.494	0.533	0.450	0.450	0.517	0.233
surface roughness (RR)	0.187	0.168	0.270	0.455	0.683	0.683	0.783	0.450
vegetation cover	0.948	0.982	0.279	0.059	0.683	0.683	0.133	0.083
species richness	0.939	0.990	0.213	0.024	0.805	0.805	0.172	0.054
K_{sat}	0.804	0.864	0.422	0.156	0.950	0.950	0.450	0.233
PC1	0.821	0.755	0.210	0.065	0.683	0.683	0.133	0.083
PC2	0.133	0.132	0.490	0.843	0.133	0.133	0.683	0.517
high intensity								
slope angle	0.457	0.673	0.902	0.664	0.683	0.683	1.000	0.233
surface roughness (TI)	0.361	0.653	0.848	0.356	0.233	0.233	0.683	0.233
surface roughness (RR)	0.990	0.658	0.482	0.342	0.950	0.950	0.517	0.450
vegetation cover	0.387	0.616	0.898	0.043	0.450	0.450	0.950	0.083
species richness	0.769	0.980	0.753	0.047	0.493	0.493	0.741	0.054
K_{sat}	0.267	0.406	0.654	0.140	0.133	0.133	0.683	0.233
PC1	0.328	0.602	0.912	0.028	0.450	0.450	0.950	0.083
PC2	0.715	0.993	0.851	0.663	1.000	1.000	0.950	0.517

Table 10 Pearson and Spearman rank correlations for the four sand distance measures (based on the relative cumulative travel distances: 50 %, 75 %, 90 % and maximum distance) and the values of the surface runoff ratio and sediment load for the three rainfall intensities (low, mid, high). Marked in green are the significant values (significance level: $\alpha = 0.1$).

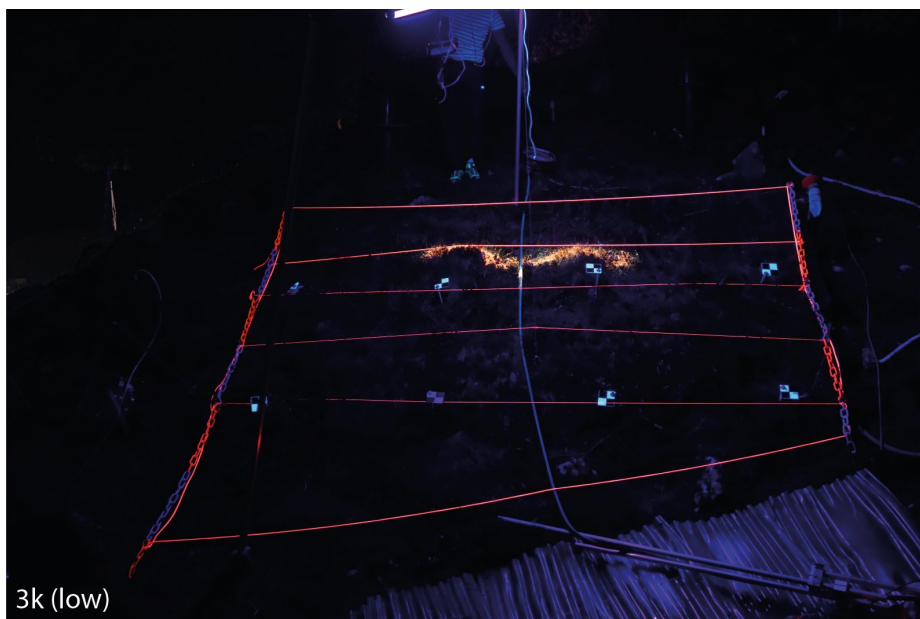
	Pearson (r)				Spearman (r _s)			
	50 %	75 %	90 %	max	50 %	75 %	90 %	max
low intensity								
surface runoff ratio	0.429	0.523	0.410	0.426	0.507	0.507	0.338	0.676
sediment load	0.383	0.434	0.325	0.332	0.304	0.304	0.068	0.541
mid intensity								
surface runoff ratio	0.924	0.928	0.633	0.282	0.872	0.872	0.462	0.564
sediment load	0.940	0.953	0.771	0.446	0.975	0.975	0.564	0.462
high intensity								
surface runoff ratio	-0.197	0.096	0.272	0.646	-0.200	-0.200	0.300	0.800
sediment load	0.065	0.343	0.532	0.578	-0.300	-0.300	0.000	0.700

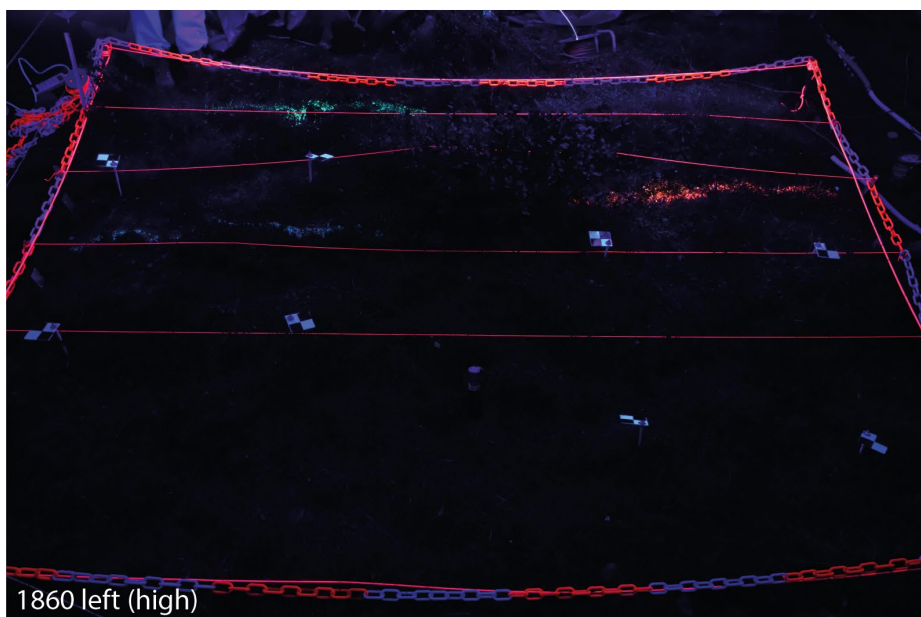
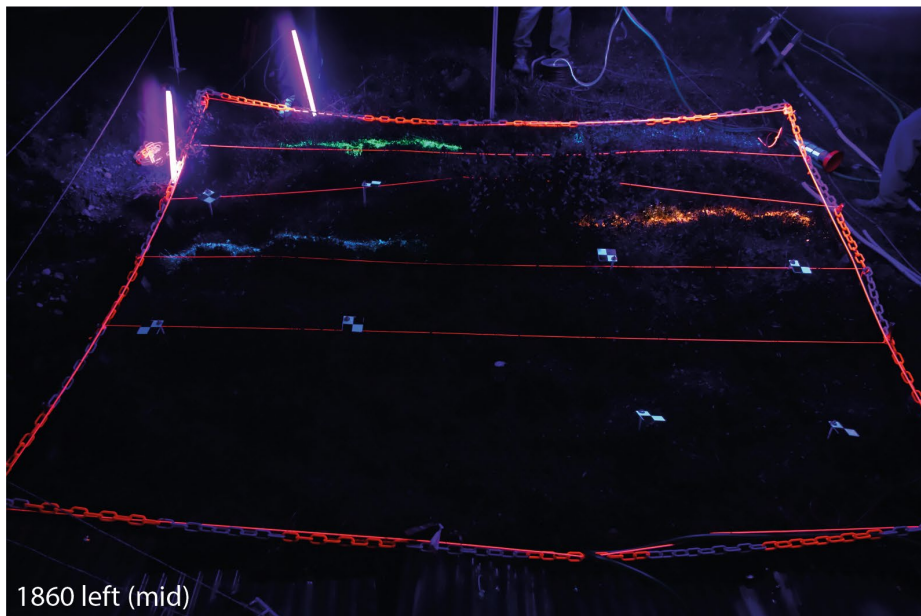
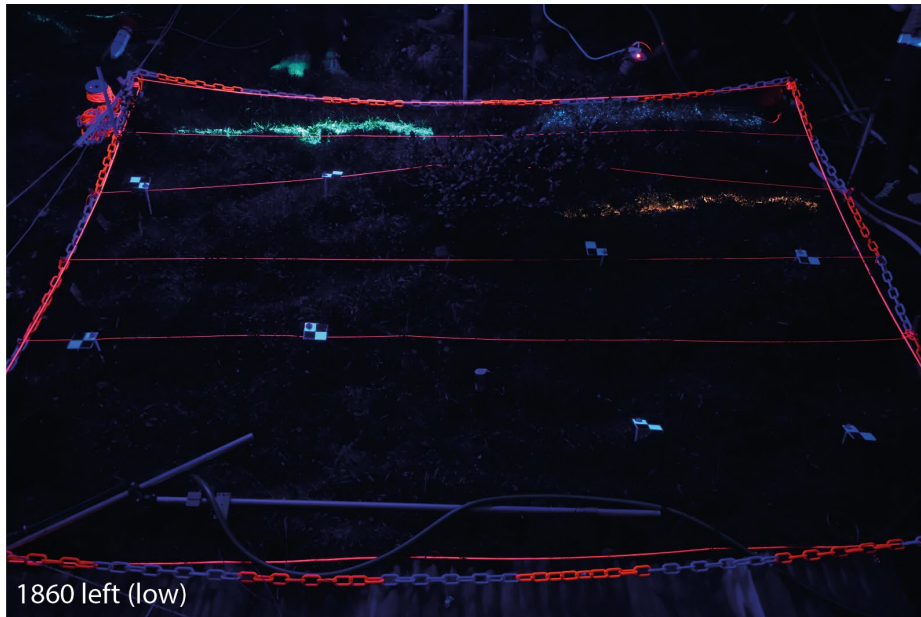
Table 11 p-values of Pearson and Spearman rank correlations for the four sand distance measures (based on the relative cumulative travel distances: 50 %, 75 %, 90 % and maximum distance) and the values of the surface runoff ratio and sediment load for the three rainfall intensities (low, mid, high). Marked in green are the significant values (significance level: $\alpha = 0.1$).

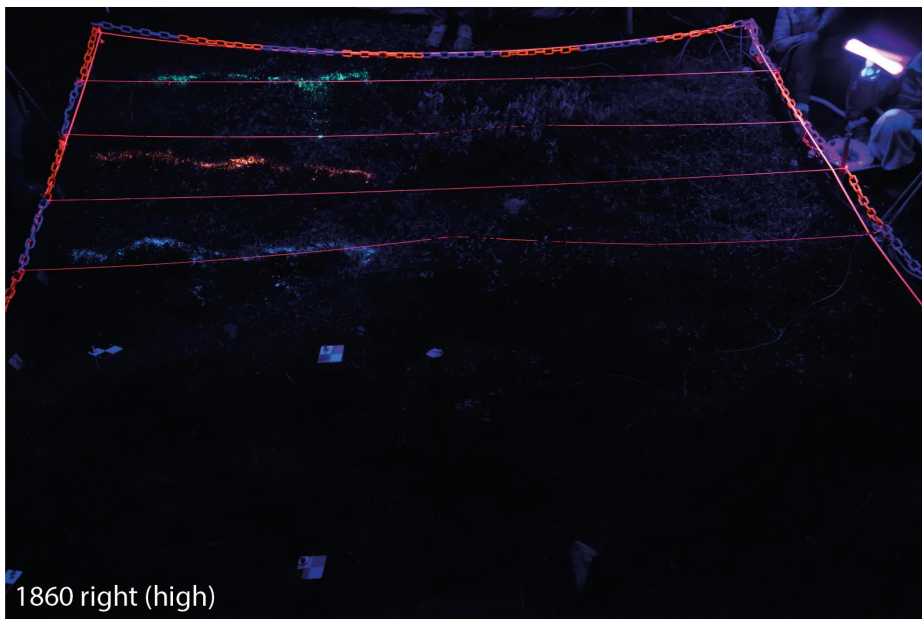
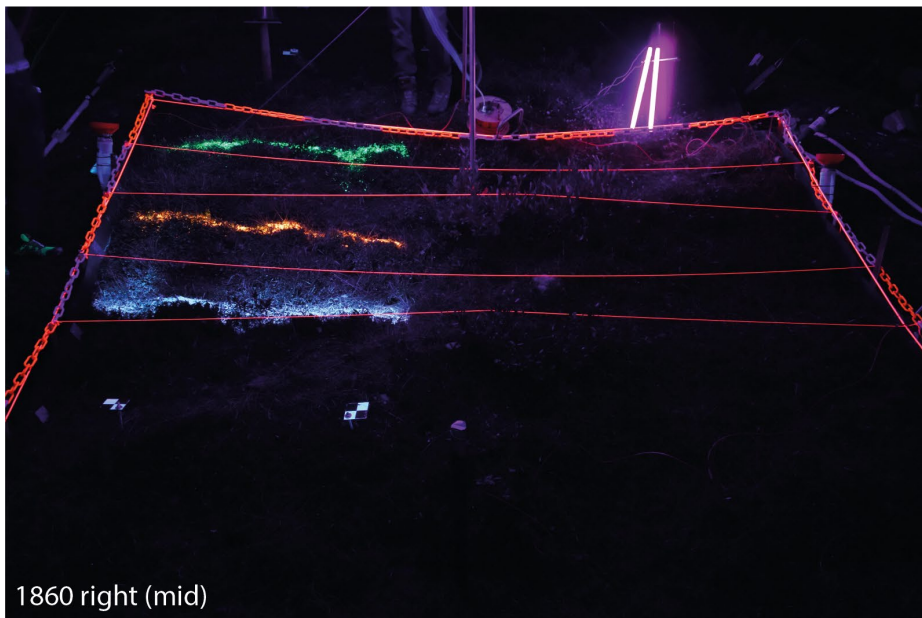
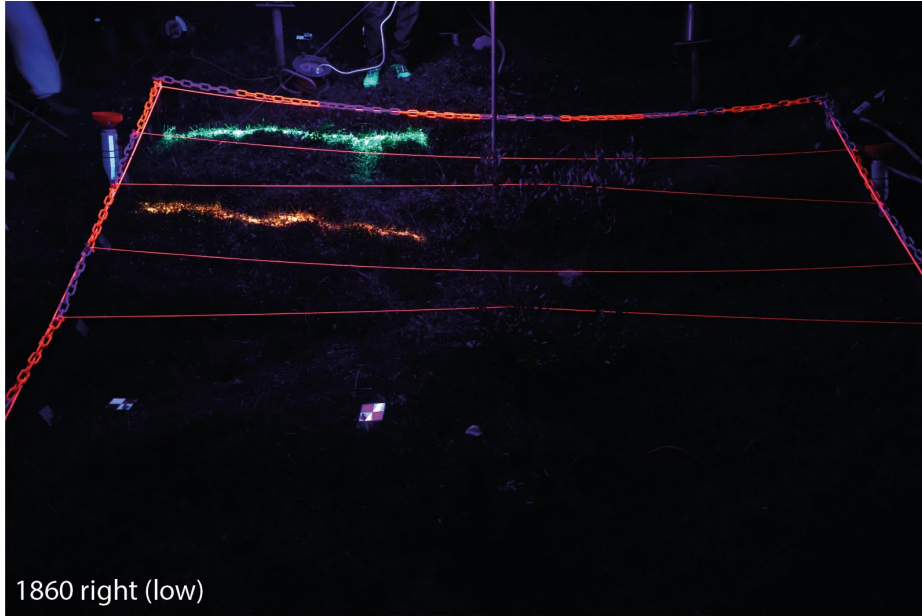
	p-value of Pearson				p-value of Spearman			
	50 %	75 %	90 %	max	50 %	75 %	90 %	max
low intensity								
surface runoff ratio	0.395	0.287	0.420	0.399	0.305	0.305	0.512	0.140
sediment load	0.454	0.390	0.530	0.521	0.558	0.558	0.899	0.268
mid intensity								
surface runoff ratio	0.025	0.023	0.252	0.646	0.054	0.054	0.434	0.322
sediment load	0.017	0.012	0.127	0.451	0.005	0.005	0.322	0.434
high intensity								
surface runoff ratio	0.751	0.878	0.658	0.239	0.783	0.783	0.683	0.133
sediment load	0.918	0.572	0.356	0.308	0.683	0.683	1.000	0.233

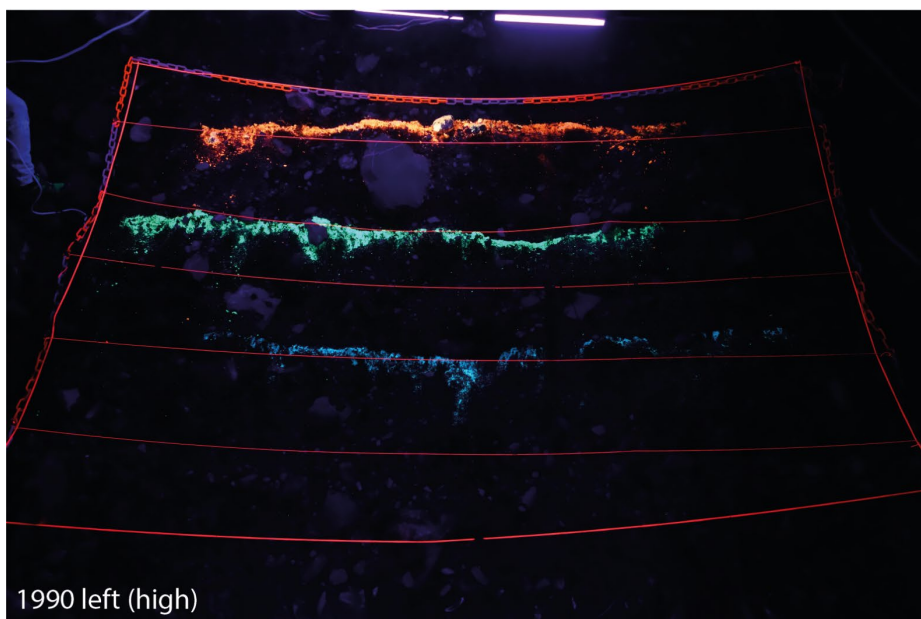
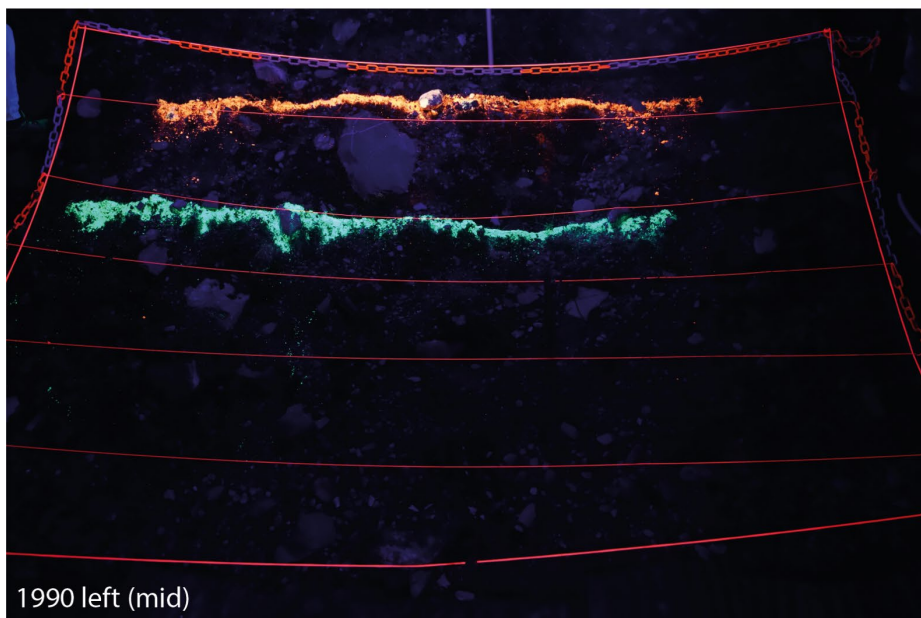
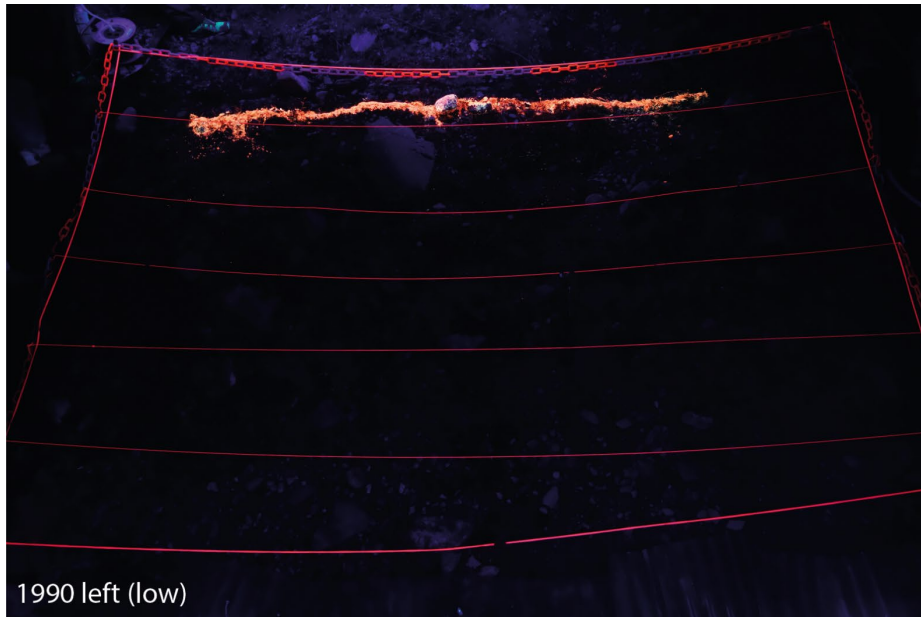
Appendix 3: Sand photographs

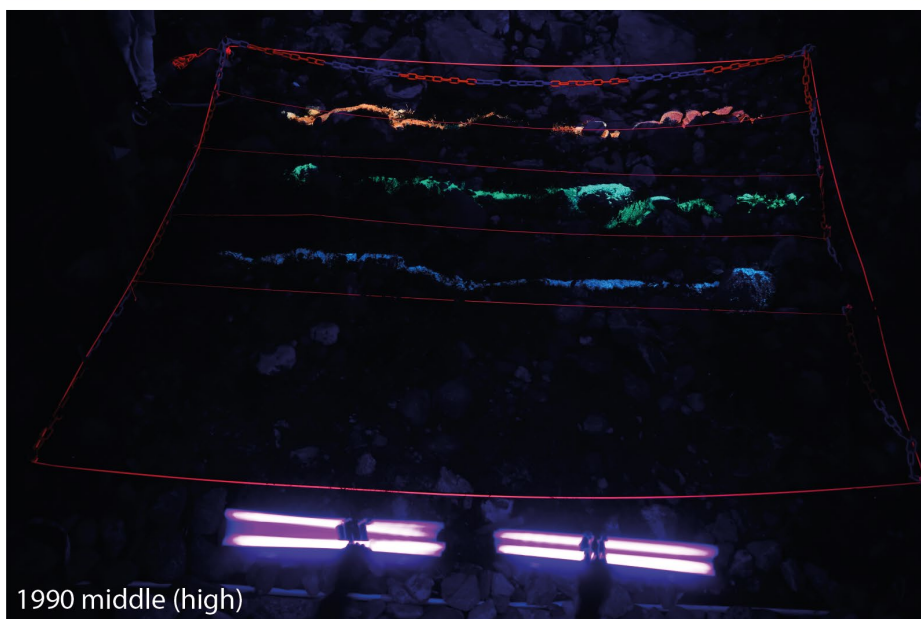
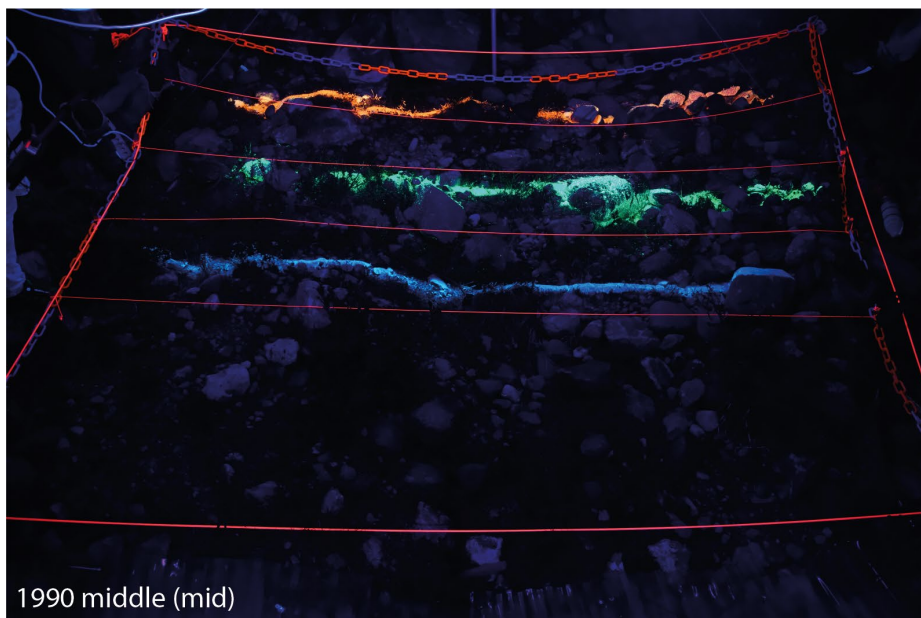
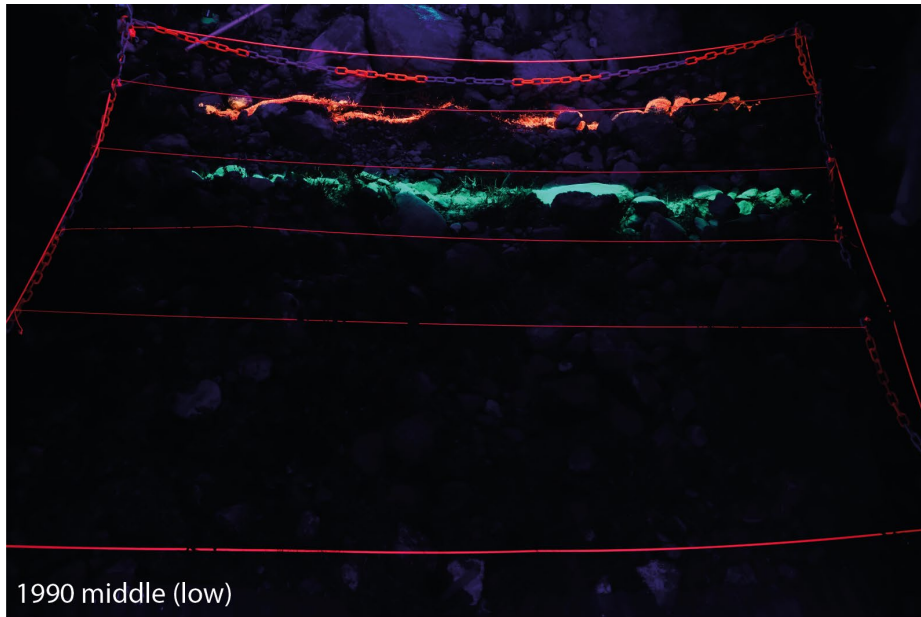
In the following the photographs of the fluorescent sand lines after the rainfall experiments (low, mid, high) are presented for the six experimental plots (3k, 1860 left, 1860 right, 1990 left, 1990 middle, 1990 right). The photographs are untouched (no geometric correction, cropping or color correction) but were downscaled in resolution. The orange sand was applied for the low intensity, the green for the mid intensity and blue for the high intensity rainfall simulation. Note that only the photos after the experiments are presented as the sand movement is only visible there. If the sand did not move far, the new sand line (for the next rainfall experiment) was already placed before taking the photo (green sand in low intensity photo / blue sand in mid intensity photo). An additional blue sand line was placed on the 1860 left plot top right already for the first experiment. This line was only used to study the sand aggregate formation after wetting (see also chapter 7.1.2) and was not used to estimate sediment transport.

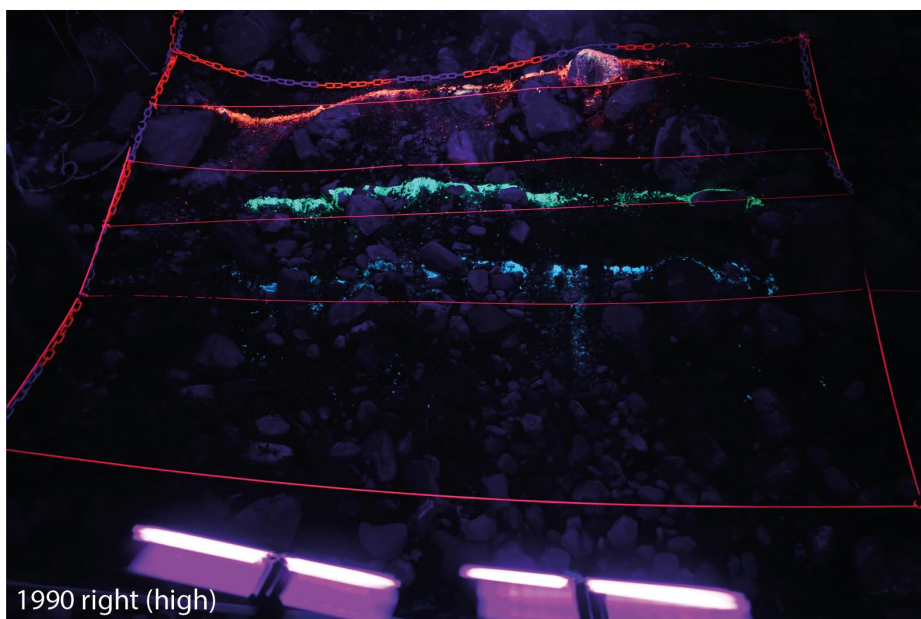
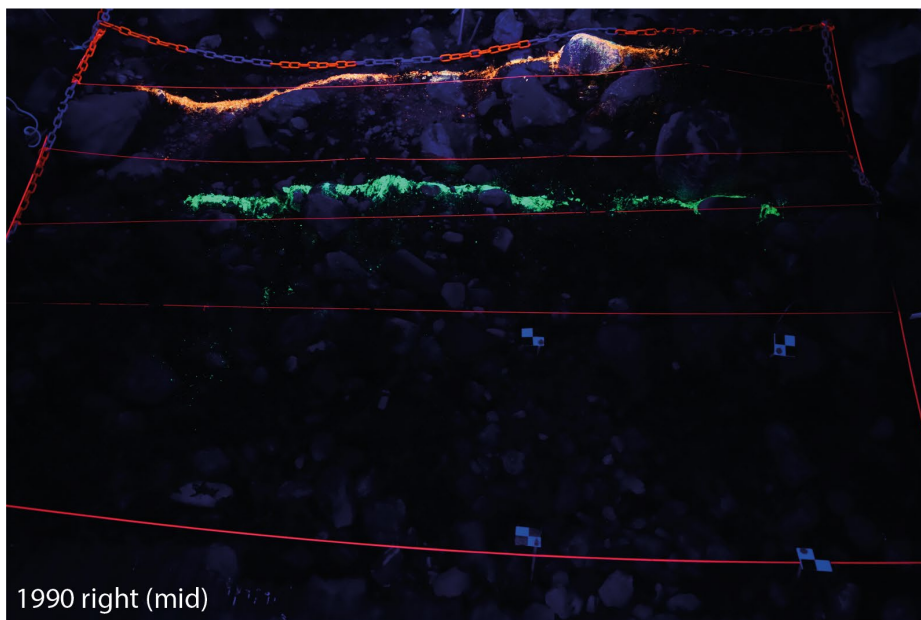
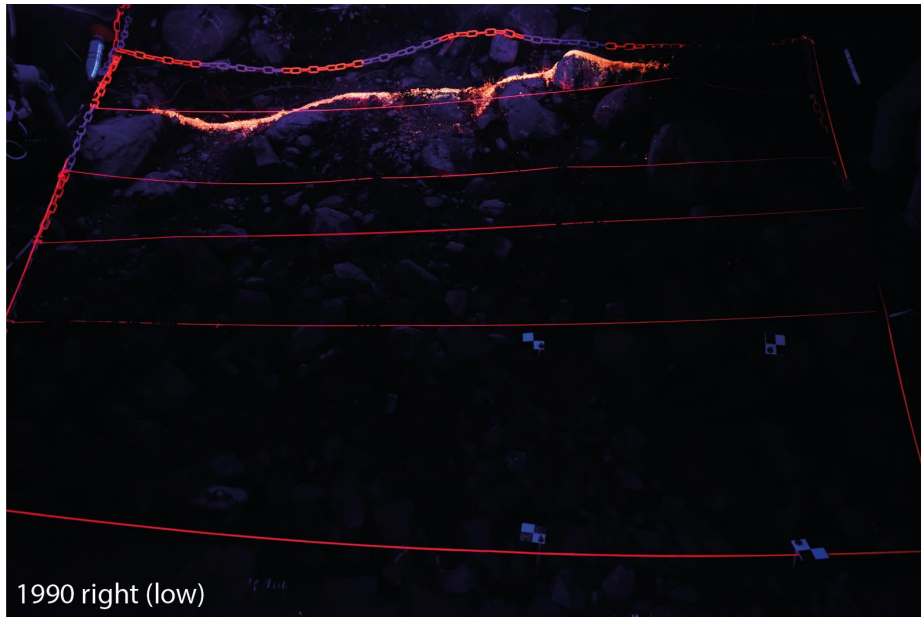












Appendix 4: Sand extraction methods

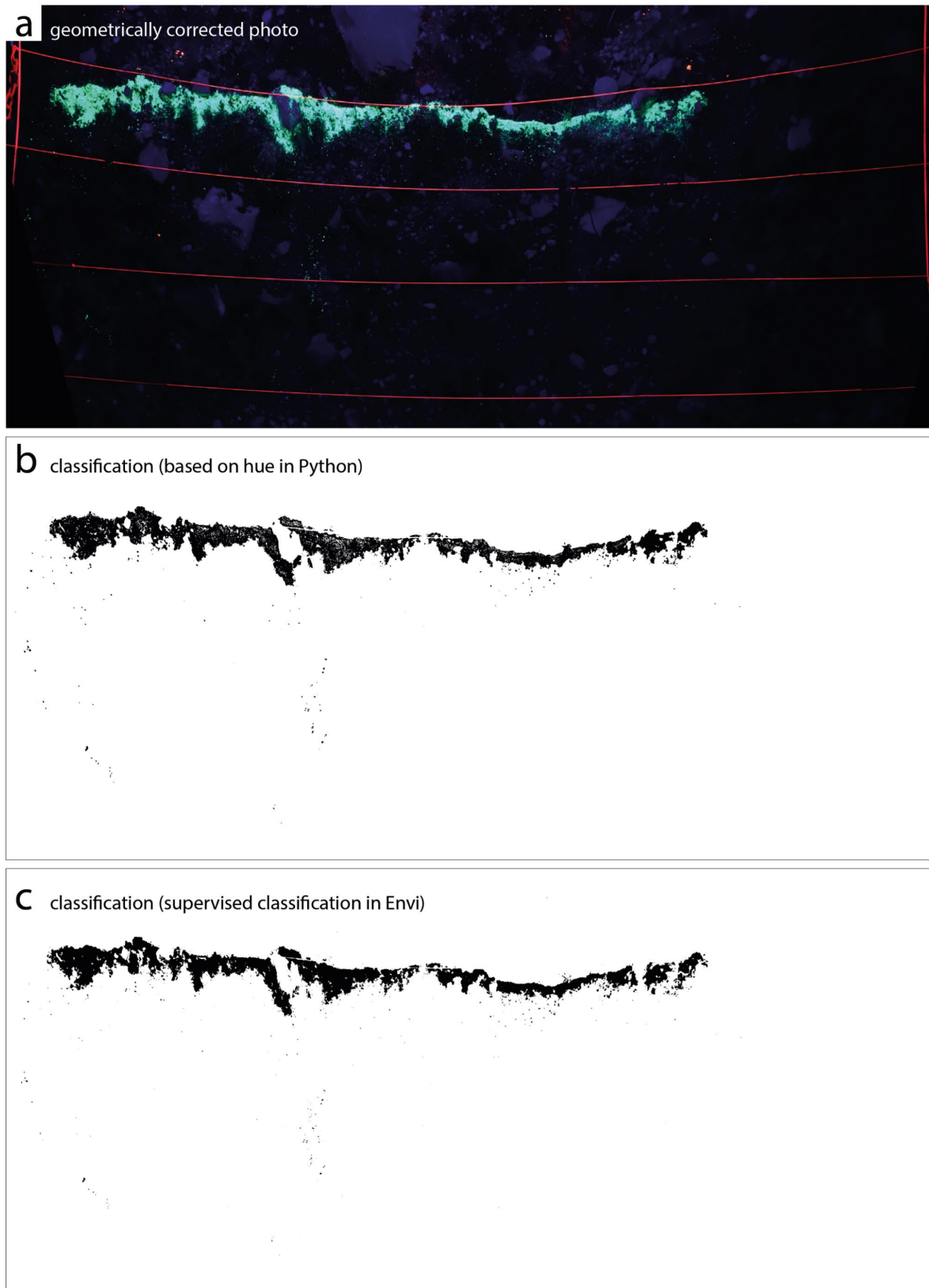


Figure A.3 (a) Geometrically corrected and cropped photo of the green sand line (mid intensity) of the 1990 left plot. (b) Classification of the green sand line based on the extraction method used in this thesis (hue in Python). (c) A supervised classification (here maximum likelihood) could, however, achieve nearly as good results. The classification was performed with Envi (v. 5.4.1), a common software for remote sensing purposes.